THE UNIVERSITY OF QUEENSLAND

AUSTRALIA

Dual-tracer simultaneous acquisition of positron emission tomography

Christopher Michael Bell

Bachelor of Science (Physics) / Bachelor of IT (Software Architecture)

A thesis submitted for the degree of Doctor of Philosophy at
The University of Queensland in 2017
Faculty of Medicine

Abstract

Positron emission tomography (PET) imaging is a versatile modality with the ability to examine metabolic factors in individual tissues *in vivo*. It is an indispensable tool for research and treatment planning of diseases such as cancer. However, versatility could be increased if it were possible to image multiple tracers simultaneously. Such an ability could be important in developing a treatment strategy for diseases that remain intractable in the majority of cases, such as advanced glioma.

Metabolic imaging with PET using target specific radiotracers has been shown to improve the delineation of tumour margins and provide increased information about tumour microbiology. However, the physical properties of radiotracers limits their combined use, such that imaging of more than one molecular target using PET is not generally considered feasible.

Multiplexing PET imaging (dual-tracer PET) offers a solution that allows for individual PET imaging of two or more individual radiotracers, within the same scanning session. Although the technique was first proposed in the 1980s, this approach is not utilised despite offering significant advantages such as multiple target imaging and validation of new PET radiopharmaceuticals. Reasons for this lack of implementation may include assumptions about the potential loss in image quality and the logistics in synthesizing multiple PET tracers simultaneously.

In this PhD, Dual-Tracer PET imaging techniques were developed, with a focus on the ability to validate chosen dual-tracer protocols prior to scanning. A set of techniques was devised to handle cases of increasing complexity: (initially) where the first tracer can be assumed to be static after a certain amount of time; secondly where the first tracer has a constant slow uptake that can be assumed to be linear; and the general case where the first tracer retains residual dynamics, with the use of a basis pursuit to separate the signals. These approaches were tested by applying them to specific, clinically relevant use cases.

Development of these techniques has provided a framework for study designers to effectively implement dual-tracer PET imaging with confidence for the validation of new tracers, the investigation of cases where multiple biological factors are important and the further development of diagnosis and treatment in future applications. Finally, by utilising

basis pursuit approaches, it is possible to consider any combination of tracers regardless of tracer and without devising specific model of uptake within tissue.

Declaration by author

This thesis is composed of my original work, and contains no material previously published or written by another person except where due reference has been made in the text. I have clearly stated the contribution by others to jointly-authored works that I have included in my thesis.

I have clearly stated the contribution of others to my thesis as a whole, including statistical assistance, survey design, data analysis, significant technical procedures, professional editorial advice, and any other original research work used or reported in my thesis. The content of my thesis is the result of work I have carried out since the commencement of my research higher degree candidature and does not include a substantial part of work that has been submitted to qualify for the award of any other degree or diploma in any university or other tertiary institution. I have clearly stated which parts of my thesis, if any, have been submitted to qualify for another award.

I acknowledge that an electronic copy of my thesis must be lodged with the University Library and, subject to the policy and procedures of The University of Queensland, the thesis be made available for research and study in accordance with the Copyright Act 1968 unless a period of embargo has been approved by the Dean of the Graduate School.

I acknowledge that copyright of all material contained in my thesis resides with the copyright holder(s) of that material. Where appropriate I have obtained copyright permission from the copyright holder to reproduce material in this thesis.

Publications during candidature

Peer-reviewed Papers

1. **Bell C**, Pannek K, Fay M, Thomas P, Bourgeat P, Salvado O, Gal Y, Coulthard A, Crozier S, Rose S 2013 Distance informed Track-Weighted Imaging (diTWI): A framework for sensitising streamline information to neuropathology. *NeuroImage* 86:60-66 **IF 6.13**

1. **Bell C***,* Dowson N, Fay M, Thomas P, Puttick S, Gal Y, Rose S 2015 Hypoxia imaging in gliomas with 18F-Fluoromisonidazole PET: Towards clinical translation. *Seminars in Nuclear Medicine* 45:136-150 **^ IF 3.13**

2. **Bell C**, Rose S, Puttick S, Pagnozzi A, Poole C, Gal Y, Thomas P, Fay M, Jeffree R, Dowson N 2014 Dual acquisition of 18F-FMISO and 18F-FDOPA. *Physics in Medicine and Biology* 59:3925-3949 **IF 2.92**

3. Puttick S*, **Bell C***,* Dowson N, Rose S, Fay M 2014 PET, MRI, and simultaneous PET/MRI in the development of diagnostic and therapeutic strategies for glioma. *Drug Discovery Today* 0:0 **^ IF 5.96**

4. **Bell C**, Dowson N, Puttick S, Gal Y, Thomas P, Fay M, Smith J, Rose S 2015 Survey on utility and feasibility of 18F-FDOPA in managing glioma. *Nuclear Medicine and Biology*, 42 10: 788-795 **IF 2.41**

5. Winter C, **Bell C**, Whyte T, Cardinal J, Macfarlane D, Rose S 2015 Blood-Brain Barrier dysfunction following Traumatic Brain Injury: correlation of Ktrans (DCE-MRI) and SUVR (99mTc-DTPA SPECT) but not serum S100B. *Neurological Research* 37(7):599-606 **IF 1.45**

6. Wellard R, Ravasio J, Guesne S, **Bell C**, Oloyede A, Tevelen G, Pope JM, Momot KI 2014 Simultaneous magnetic resonance imaging and consolidation measurement of articular cartilage. *Sensors* 14(5):7940-58 **IF 2.05**

7. Rundle-Theile D, Day B, Stringer B, Fay M, Martin J, Jeffrey L, Rose S, Gal Y, Thomas P, Crozier S, Coulthard A, Salvado O, **Bell C**, Salvado O, Gal Y, Coulthard

A, Crozier S, Rose S 2015 Using the apparent diffusion coefficient to identify MGMT promoter methylation status early in glioblastoma: importance of analytical method. *Journal of Medical Radiation Sciences* 62(2): 92–98

8. **Bell C**, Dowson N, Puttick S, Rose S 2016 Design and utilisation of protocols to characterise dynamic PET uptake of two tracers using basis pursuit. *Physics in Medicine and Biology* – Accepted April 2017

* Co First Authors – Equal Contributors

^ Invited submission

Book Chapters

1. Mike Fay, Chris Bell, Nick Dowson, Simon Puttick and Stephen Rose (2015). Imaging of Brain Tumours, Molecular Considerations and Evolving Surgical Management Issues in the Treatment of Patients with a Brain Tumor, Dr. Terry Lichtor (Ed.), InTech, DOI: 10.5772/59981. Available from: https://www.intechopen.com/books/molecular-considerations-and-evolving-surgical-management-issues-in-the-treatment-of-patients-with-a-brain-tumor/imaging-of-brain-tumours

Conference Abstracts

1. Puttick S, Dowson N, Fay M, **Bell C**, Martin J, Rose S 2015 Effect of ligand size uptake and washout of EphA2 targeted theranostics using 64Cu-PET. *Brain & Brain PET* – Vancouver, Canada

2. Bell C, Puttick S, Fay M, Rose S, Dowson N 2017 Dual PET tracer imaging to validate biodistribution of a theranostic. *International Symposium on Biomedical Imaging* – Melbourne, Australia

Posters

1. **Bell C** 2014 Multiplexing 18F-FDOPA and 18F-FMISO PET in gliomas. *The AEHRC Colloquium* – Brisbane, Australia.

2. Puttick S, **Bell C** 2014 Multiplexing Radiotracers: Increasing the Power of Positron Emission Tomography. *NanoBio* – Brisbane Australia

Publications included in this thesis

Bell C *et al* 2015 Hypoxia imaging in gliomas with 18F-Fluoromisonidazole PET: Towards clinical translation. *Seminars in Nuclear Medicine* 45:136-150 – incorporated in Chapter 2.

Contributor	Statement of contribution
Christopher Bell (Candidate)	Literature research (70%) Wrote and edited paper (60%)
Nicholas Dowson	Literature research (5%) Wrote and edited paper (10%)
Mike Fay	Literature research (5%) Wrote and edited paper (5%)
Paul Thomas	Literature research (5%) Wrote and edited paper (5%)
Simon Puttick	Literature research (5%) Wrote and edited paper (5%)
Yaniv Gal	Literature research (5%) Wrote and edited paper (5%)
Stephen Rose	Literature research (5%) Wrote and edited paper (10%)

Bell C *et al* 2015 Survey on utility and feasibility of 18F-FDOPA in managing glioma. *Nuclear Medicine and Biology*, 42 10: 788-795 – incorporated in Chapter 2.

Contributor	Statement of contribution
Christopher Bell (Candidate)	Literature research (70%) Wrote and edited paper (60%)
Nicholas Dowson	Literature research (5%) Wrote and edited paper (10%)
Yaniv Gal	Literature research (5%) Wrote and edited paper (5%)
Paul Thomas	Literature research (5%) Wrote and edited paper (5%)
Mike Fay	Literature research (5%) Wrote and edited paper (5%)
Jye Smith	Literature research (5%) Wrote and edited paper (5%)
Stephen Rose	Literature research (5%) Wrote and edited paper (10%)

Bell C *et al* 2014 Dual acquisition of 18F-FMISO and 18F-FDOPA. *Physics in Medicine and Biology* 59:3925-3949 – incorporated as Chapter 3.

Contributor	Statement of contribution
Christopher Bell (Candidate)	Experimental design (60%) Experimental implementation (5%) Analysis (70%) Wrote and edited paper (55%)
Stephen Rose	Experimental design (20%) Wrote and edited paper (10%)
Simon Puttick	Experimental implementation (75%) Wrote and edited paper (5%)
Alex Pagnozzi	Experimental design (5%) Wrote and edited paper (1%)
Christopher Poole	Experimental implementation (5%) Wrote and edited paper (1%)
Yaniv Gal	Wrote and edited paper (5%)
Paul Thomas	Experimental implementation (5%) Wrote and edited paper (1%)
Michael Fay	Experimental implementation (5%) Wrote and edited paper (1%)
Rosalind Jeffrey	Experimental implementation (5%) Wrote and edited paper (1%)
Nicholas Dowson	Experimental design (15%) Analysis (30%) Wrote and edited paper (20%)

Bell C, *et al* 2017 Design and utilisation of protocols to characterise dynamic PET uptake of two tracers using basis pursuit. *Physics in Medicine and Biology* – Under Revision March 2017

Contributor	Statement of contribution
Christopher Bell (Candidate)	Experimental design (60%) Experimental implementation (70%) Analysis (70%) Wrote and edited paper (65%)
Stephen Rose	Experimental design (20%) Wrote and edited paper (10%)
Simon Puttick	Experimental implementation (30%) Wrote and edited paper (5%)
Nicholas Dowson	Experimental design (20%) Analysis (30%) Wrote and edited paper (20%)

Contributions by others to the thesis

Prof Stephen Rose (primary supervisor), Dr. Nicholas Dowson (associate supervisor), Dr. Yaniv Gal (associate supervisor), Dr. Andrew Bradley (associate supervisor), Dr. Simon Puttick, Dr. Mike Fay, Dr. Paul Thomas, Mr. Alex Pagnozzi, Dr. Christopher Poole, Dr. Rosalind Jeffrey, Dr. Brett Stringer. Dr. Bryan Day, Dr. Andrew Boyd, Dr. James Doeke have all made contributions towards research ideas, experimental design, experimental analysis and statistical analysis. This thesis contains work that has been published (Chapters 2-6). The individual contributions of all authors are detailed in the previous section.

Statement of parts of the thesis submitted to qualify for the award of another degree

None

Acknowledgements

I wish to thank Prof. Stephen Rose, Dr. Nicholas Dowson, Dr. Simon Puttick, and Dr. Yaniv Gal and Dr. Andrew Bradley for their continual support for the entire duration of this doctorate, both inside and outside the academic bounds.

I wish to thank the RBWH and RAPID SCGH for provision of radioactive tracer needed for experimental data.

I wish to thank the Australian Government and UQ for financial support during the majority of my candidature.

I wish to thank my family – My parents Keith and Louise, my wife Laura and my baby girl Sophie for supporting me.

Keywords

pet imaging, dual-tracer, multiplexing, kinetic modelling, 18f-fmiso, 18f-fdopa, 64cu-epha2, glioma

Australian and New Zealand Standard Research Classifications (ANZSRC)

ANZSRC code: 111202, Cancer Diagnosis, 25%

ANZSRC code: 111207, Molecular Targets, 15%

ANZSRC code: 080801, Image Processing, 60%

Fields of Research (FoR) Classification

FoR code: 1112, Oncology and Carcinogenics, 100%

Table of Contents

List of Figures

List of Tables

List of Equations

List of Abbreviations

AA	Anaplastic Astrocytoma
BBB	Blood Brain Barrier
CE-MRI	Contrast Enhanced Magnetic Resonance Imaging
CNS	Central Nervous System
CT	Computed Tomography
FLAIR	Fluid Attenuated Inversion Recovery
GBM	Glioblastoma
HGG	High-Grade Glioma
IgG	Immunoglobulin G
LGG	Low-Grade Glioma
LOR	Line Of Response
MRI	Magnetic Resonance Imaging
NIF	National Imaging Facility
PET	Positron Emission Tomography
SWI	Susceptibility Weighted Imaging
TAC	Time Activity Curve
V_T	Volume of Distribution
WHO	World Health Organisation
WK1	A patient derived glioma cell line

Chapter 1 – Introduction

Positron Emission Tomography (PET) has found increasing clinical use for the management of a range of diseases, including infiltrating advanced glioma, where it complements the information on oedema and blood brain barrier breakdown supplied by Magnetic Resonance Imaging (MRI) (1, 2). The utility of PET lies in its ability to identify regions with particular biological characteristics that are relevant to oncology management, which is accomplished through the use of radioactive tracers with specific molecular targets. With the development of novel therapeutics and more sophisticated treatment regimes, the need to image multiple molecular targets using PET imaging is becoming more apparent. This is the case for glioma, where the heterogeneous presence of hypoxic and metabolically active regions has potential relevance for planning surgery and radiotherapy. Metabolically active regions are likely to contain particularly aggressive phenotypes and hypoxic regions are known to be resistant to radiotherapy (3, 4).

While multi-target PET imaging may provide additional important information, the physical properties of radiotracers limits their use, such that typical imaging of a second molecular target using PET while residual activity from the first tracer remains is not considered to be feasible. The longer the half-life of the first tracer, the longer the delay needed between the two scans. This is due to the fact that the PET scanner cannot differentiate between tracers for individual decay events. The current accepted method for acquiring information on more than one radiotracer is to perform multiple scans, with sufficient intervening time between the two scans to prevent cross-contamination. This process itself introduces a number of potential logistical and technical problems, including the introduction of image registration, a temporal gap in metabolic information, physiological changes due to patient movement/orientation, and an increase in scanner and specialist time.

Research Rationale

An alternative to performing multiple PET acquisitions is dual-tracer PET imaging, first proposed by Huang *et al* in 1982, where both radiotracers are imaged within a single scanning session and specific computational techniques are used to separate the signals of the two tracers post-reconstruction (5). Further investigations have sought to develop

dual-tracer imaging into a viable imaging tool. However, these methods are subject to certain limitations.

Implementation of dual-tracer imaging potentially provides for the same benefits as two single scans, while circumventing some of the logistical issues imposed by separate scanning. In addition to providing more detailed information on intratumoral biology, the technique of dual-tracer imaging also lends itself to other applications, including novel tracer validation. With such a range of applications and clinical need, there is an inherent necessity for a set of tools that allow a study designer to investigate dual-tracer imaging, irrespective of the temporal characteristics of the tracers used and the variance in the pattern of tracer uptake within the field of view.

To accomplish this, both static and dynamic reconstructions must be considered. Static reconstruction allows for a “snapshot” of the radiotracer activity to be taken over a short period of time. For dynamic imaging, acquisition begins from tracer injection, with computer post-processing (“kinetic modelling”) employed to analyse the temporal characteristics of the tracer.

For dual tracer techniques, the following aspects are also to be taken into account:

- Post-processing technique: The temporal behaviour of the tracers involved will determine the post-processing technique required to separate the two tracers. The more complex the residual dynamics of the first tracer at the injection of the second tracer, the more complex the post-processing technique will be required to separate the two tracer signals.
- Imaging protocol: The length of the scan and the temporal gap between the injection of the two tracers will have an impact on the quality of the separated images. If the scanning length is too short, or the temporal gap is too small, the resulting tracer information will have increased error. In some cases, the increase in error will render the images unable to serve their intended purpose.

Overall aims and outline of thesis

Therefore, the overarching goal of this thesis is to design dual-tracer frameworks that can be applied to a wide variety of situations, and also allow the study designer to pre-validate the proposed protocol to ensure the efficacy of the resulting images. To accomplish this,

three frameworks for dual-tracer imaging are described and developed to cover the full range of scanning acquisitions and protocols. In this way, study designers can investigate potential dual-tracer imaging sequences against their selection of biology and radioactive tracer prior to performing any actual experiments. Hence, this thesis has three aims:

1. Develop a framework to allow study designers to perform static dual-tracer imaging on a pair of tracers, where it can be assumed that the activity of the first tracer is at equilibrium.
2. Extend this framework to consider the case where the first tracer has some residual dynamics.
3. Develop a framework to allow dynamic dual-tracer imaging in the general case that can allow designers to consider any combination of tracers and tissue.

These aims are investigated in the coming chapters, an outline of which is presented in Table 1-1.

Table 1-1 Thesis overview

Chapter	Overview
Chapter 2	**Background** - Introduces PET imaging and glioma - Discusses the need for multi-tracer imaging - Introduces dual-tracer PET imaging and the current literature
Chapter 3	**Dual acquisition of ^{18}F-FMISO and ^{18}F-FDOPA** Presents a framework for static dual-tracer imaging where the activity of the first tracer is at equilibrium at injection of the second tracer (Thesis aim 1). Validated using ^{18}F-FMISO and ^{18}F-FDOPA.
Chapter 4	**Extension to where first tracer dynamics are not at equilibrium** Extends the previous chapter to include the ability to validate scanning protocols where the first tracer continues to have residual dynamics at the injection of the second tracer (Thesis aim 2). Validated using ^{64}Cu-EphA2 and ^{18}F-FDOPA
Chapter 5	Performing dual tracer PET imaging in the general case Develops a novel technique for validating protocols for performing dynamic dual-tracer PET imaging (Thesis aim 3). This technique employs a method called basis pursuit to fit the activity of the tracers over time, and subsequently separate them. This approach is validated using ^{18}F-FDG and ^{18}F-FDOPA data.
Chapter 6	Summary - Summarises the contributions of the doctorate. - Discusses limitations of this work. - Discusses future research directions.

Chapter 2 – Background

This chapter consists of two published papers: “Survey on utility and feasibility of ^{18}F-FDOPA in managing glioma” and “Hypoxia imaging in gliomas with 18F-Fluoromisonidazole PET: Towards clinical translation”. Together, they analyse present suspected causes for treatment failure in glioma and the caveats of MR imaging. They systematically review and discuss the use of each tracer in the diagnosis and treatment of malignant glioma, demonstrating that these tracers could complement each other in clinical practice. Finally, the need for dual-tracer PET imaging is discussed, laying the foundation for the novel work in this doctoral thesis.

Glioma

Gliomas (Figure 2-1) are the most commonly occurring primary brain tumours, signified by their invasive potential and increased capacity for proliferation (2). These tumours have a uniformly poor prognosis, and while the median survival of patients with WHO grade IV gliomas (glioblastomas; GBM) is now longer than 12 months, most patients succumb within two years (6-8). Patient survival often depends largely on the extent of surgical resection, pretreatment functional status or the age of the patient (9-11). WHO Grade III anaplastic gliomas and WHO Grade II gliomas are less aggressive and have a more promising, yet still poor, prognosis of 2-5 and 2 years, respectively (12). Gliomas are the most common neoplasm in the brain, accounting for 80% of malignant brain tumours and 30% of all brain and CNS tumours (13, 14).

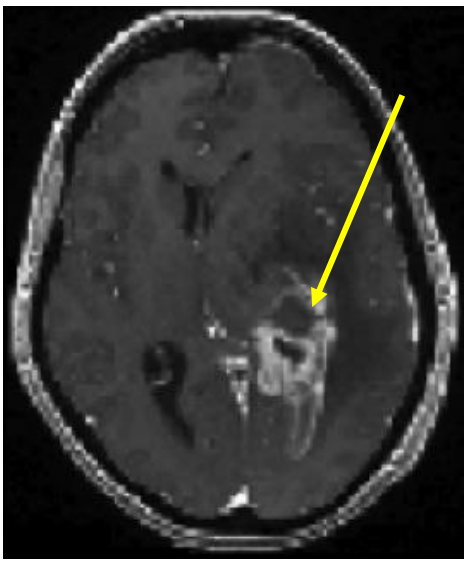

Figure 2-1Example brain slice of a patient with glioblastoma (WHO grade IV glioma). The patient was scanned with contrast enhanced MRI. The tumour is shown by the yellow arrow.

Tumour recurrence plays a large role in patient mortality, with treatment resistance thought to take significant part in recurrence. A number of important factors are thought to promote resistance, including vasculogenesis, cancer stem cells (CSC), hypoxia, and infiltration, all of which are believed to be biologically linked within the tumour microenvironment. To understand their relevance to treatment outcome, *in vivo* imaging of glioma cases needs to be performed. PET imaging using tracers such as ^{18}F-FMISO and ^{18}F-FDOPA allow for characterisation of hypoxia and metabolism, respectively. Effective imaging of these tracers will help to describe the disease as well as assist in treatment planning regimes.

Background to imaging with Positron emission tomography

While current imaging techniques such as MRI are routinely used for oncological imaging, different imaging modalities have particular caveats. Positron emission tomography (PET) can provide information on the underlying microbiology of tumours such as glioma, complimenting structural information gained from MRI. PET imaging relies on the decay of a radioactive tracer injected into a patient to determine the location of a specific biological process.

The first step in PET imaging is the synthesis of the radioactive tracer that will be injected into the patient, which is made up of two key components: the molecular analogue and the radioactive isotope.

The molecular analogue is first chosen as each analogue specifically targets a biological process. For example, ^{18}F-FDG - the most common oncological tracer, is a glucose analogue and is taken up by cells during cell metabolism. ^{18}F-FDG is transported into tumor cells and phosphorylated by hexokinase. Since ^{18}F-FDG is not metabolised further, it remains metabolically trapped intracellularly as FDG-6-phosphate. Specifically, ^{18}F-FDG is taken up by metabolising cells, but only excreted via the slower process of dephosphorylation which typically becomes apparent at 45 minutes post-injection, allowing for identificaton of particularly active cells (15). Since cancerous cells are more metabolically active than normal cells in most tissues, with the particular exception of tissues within the brain, uptake is more rapid, and thus a brighter spot on the PET image implies faster metabolism and is a sign of pathology. Analogues for other molecules also exist, which can be utilised to examine other aspects of disease. An outline of some of these analogues is shown in Table 2-1.

Table 2-1 Common molecular analogues using in PET radiopharmaceuticals.

Analogue	Abbreviation	Original molecule	Target biological process
Fluorodeoxyglucose	FDG	Glucose	Metabolism
fluoro-l-phenylalanine	FDOPA	L-Dopa	Dopaminergic Activity
Fluoromisonidazole	FMISO	Misonidazole	Hypoxia
Methionine	MET	Methionine	Protein synthesis
Fluorothymidine	FLT	Thymidine	Proliferation
Fluoro-ethyl-tyrosine	FET	Ethyl-tyrosine	Infiltration

There are a range of radioactive isotopes available, selection of which depends on isotope availability/synthesisability, half-life and ability to attach it to the molecular analogue. For PET imaging, only isotopes that decay by means of positron emission can be used. Table 2-2 shows common radioactive isotopes used in PET imaging, along with their half-lives and synthesis method. A longer half-life is often desirable, as a half-life that is too short limits the use of the tracer to on-site scanners, or scanners within a short travelling time. However, a shorter half-life may be desired if the tracer is irreversibly bound in the tissue in order to limit radiation dose.

Table 2-2 Radioactive isotopes commonly used in PET imaging, along with their half-lives and synthesis method.

Isotope	Name	Half Life (Minutes)	Synthesis method
^{18}F	Fluorine	109.7	Cyclotron
^{64}Cu	Copper	762.0	Cyclotron
^{11}C	Carbon	20.33	Cyclotron
^{15}O	Oxygen	2.037	Cyclotron
^{68}Ga	Gallium	67.92	Generator
^{82}Ru	Rubidium	1.273	Generator

Reconstruction of the acquired data can either be static or dynamic. Static imaging allows for a “snapshot” to be taken once an approximate equilibrium has been reached. Generally imaging is only over a few minutes (depending on specifics such as tracer half-life, rate of uptake and the injected activity), with the resulting image to be a sum or average of activity of the scan. This method is most commonly utilized in the clinic. Dynamic reconstruction can be from the injection of the radiotracer into the patient. After reconstruction, computer post-processing (“kinetic modelling”) is employed to analyse how the radiotracer behaves in the body over time. Dynamic imaging can provide additional salient information on the underlying tissue biology, and is more frequently used in the research setting.

The processes involved in a typical clinical static PET scan are shown in Figure 2-2a for static imaging and Figure 2-2b for dynamic.

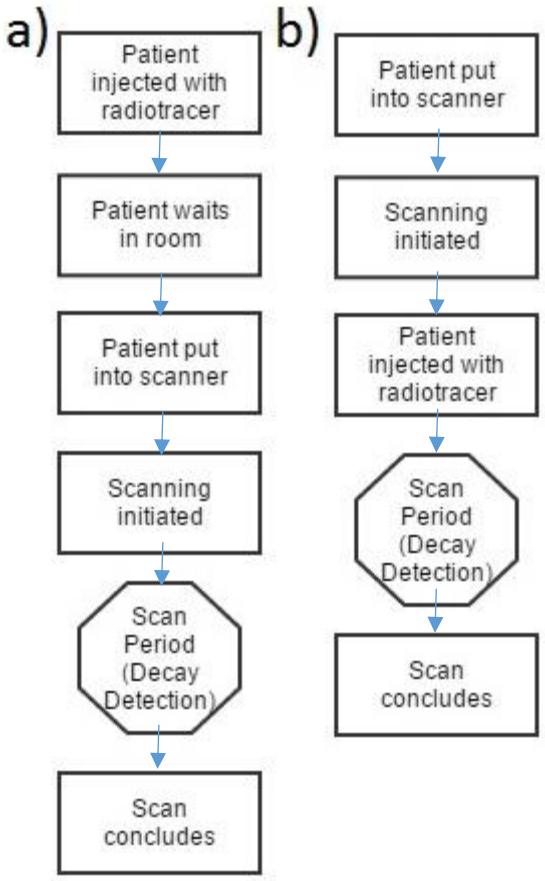

Figure 2-2 Flowchart of typical static (a) and dynamic (b) PET scans. The stage at where the tracer is injected depends on the scanning type. For static scans, the tracer is injected prior to scanning to allow time for uptake of the tracer into the cells and near steady state to be reached. For dynamic scanning, the tracer is injected after scanning has been initiated so that full tracer pharmacokinetics can be acquired.

Once the scanning has been completed, the PET images are reconstructed into a 3D volume of interest (with a fourth temporal dimension where required) ready for post-processing and analyses. Computed Tomography (CT) is often used to correct for attenuation due to denser tissue types.

The synthesis and application of these tracers allows *in vivo* imaging of diseases such as glioma, and opens up new pathways for patient diagnosis and treatment.

The role of ^{18}F-FMISO and ^{18}F-FDOPA in glioma

^{18}F-FMISO and hypoxia

It has been shown that low oxygen tension is associated with persistent tumour activity following radiotherapy and the subsequent development of local recurrences and metastases (16-18). Cells become hypoxic when they exist at distances greater than 1-2 mm from vasculature, where diffusion of oxygen is no longer possible (19). While hypoxia in normal tissue is rare, it is a known phenomenon found in most solid tumours and can be classified into three distinct types: chronic, acute and anaemic (20, 21). Chronic hypoxia was first hypothesized in 1955, when the central cores of bronchial tumours were noted to be necrotic (22). It occurs in cells that are no longer within range of vascularity, often due to the tumour outgrowing its blood supply or proliferation pressure forcing cells away from blood vessels. The presence of necrosis is a requirement in diagnosis of glioblastomas, as it signifies a high proliferation rate followed by outstripping of blood supply, resulting in chronic hypoxia and eventually necrosis (23).

Acute hypoxic cells, in contrast, are cells temporarily oxygen deprived due to the brief closure of vessels. These closures are caused by severe vascular abnormalities within the tumour volume, leading to leaky vessels and alterations in intratumoral pressure. This can cause abrupt changes in blood supply, preventing oxygen and nutrients from reaching the tumour cells. Acutely hypoxic cells become normoxic again when blood flow is redirected back to the cells via angiogenesis or recanalisation of the vessels.

Anaemic hypoxia relates to a reduced O_2-carrying capacity of the blood supply. This may be associated with either the tumour or the treatment itself.

It is well known that hypoxic tumour cells are more resistant to radiation, as the presence of oxygen facilitates the rendering of radiation induced DNA damage permanent. In fact, 2

to 3 times greater radiation dosage is required to induce cell death in hypoxic tissue compared with normoxic tissue (24). A recent study investigating the presence of persistent DNA double strand breaks (DSBs), which leads to mitotic cell death and tumour regression, has shed light on the association between hypoxia and radiation insensitivity (25, 26). In this study the dose-response of residual YH2AX foci, a robust measure of DSBs, was found to be highly dependent on tumour cell oxygenation, *i.e.* normoxic regions showed greater YH2AX expression indicating increased sensitivity to radiotherapy (27).

Despite development of novel hypoxia targeting radiotracers, ^{18}F-FMISO remains in use. Pioneering work by Valk *et al* some two decades ago, highlighted the role of ^{18}F-FMISO as a hypoxic sensitizer in a small number of patients with high-grade gliomas (28). Initial uptake activity of ^{18}F-FMISO at the site of blood-brain barrier BBB breakdown exceeded the activity in the normal cortex, with tumour hypoxia clearly delineable during the first five minutes of the ^{18}F-FMISO scan. Uptake in tumoural regions exhibiting unperturbed BBB was slower, with maximum uptake peaking at around 40 minutes. In this early study, retention of ^{18}F-FMISO occurred in two of the three patients, with uptake remaining significantly higher than cortical tissue. This work was the first to demonstrate using ^{18}F-FMISO PET that hypoxia does occur in human brain tumours, and suggested that ^{18}F-FMISO has potential for *in vivo* evaluation of hypoxia in glioma cases.

^{18}F-FDOPA and tumour infiltration

For both newly diagnosed and recurrent brain tumours, it is imperative that the exact glioma tumour volume is known for both planning surgical resection and subsequent radiation therapy. The propensity for gliomas to infiltrate along white matter structures is well established from pathology studies (29, 30). It is also well known that lesions on an MRI do not necessarily correspond to regions of tumour infiltration (31). Thus, the use of MRI alone for surgical and radiotherapy planning runs the risk of underestimating the tumour volume. ^{18}F-FDOPA PET, on the other hand, has been shown to identify regions of infiltration and proliferation (32-39). ^{18}F-FDOPA was first synthesised in the 1980's for the purpose of examining Parkinson's disease (40). However, a case study by Heiss *et al* in 1996 illustrated a potential new role for ^{18}F-FDOPA in the brain (41). While evaluating a movement disorder in a patient with suspected Parkinson's disease, ^{18}F-FDOPA imaging revealed a mass in the right frontal lobe. Further multi-modal studies investigating the lesion were suggestive of a low-grade glioma, with high ^{11}C-MET uptake displayed within the same area. This unexpected, yet important finding was the first to describe the possibility

that ^{18}F-FDOPA may provide complimentary information to other amino acid PET tracers, such as ^{11}C-MET and ^{18}F-tyrosine, in the assessment of gliomas.

^{18}F-FMISO, ^{18}F-FDOPA and the link to MR imaging

Contrast enhanced T_1, T_2 and FLAIR imaging are mainstays in the treatment planning and follow-up of patients diagnosed with gliomas (42, 43). There is evidence that a relationship between MR defined tumour volumes and hypoxia exists, as hypoxia is known to initiate the angiogenic cascade, resulting in eventual BBB breakdown: Hypoxia has been shown to promote neovascularization through a large number of molecular signals, leading to leakage of the blood-brain barrier (44, 45). A number of studies have been performed comparing the efficacy of ^{18}F-FMISO PET and MRI in detecting regions of hypoxia.(46-49) Together, these results confirm a relationship between tumour hypoxia and MRI defined volumes and metabolic imaging, with ^{18}F-FMISO PET appearing to provide an improved assessment of tumour hypoxia compared with surrogate MRI markers, such as contrast enhancement.

In addition, current research studies suggest that a link between tumour infiltration as imaged by ^{18}F-FDOPA and MRI derived indices exist (36, 50). Hence, while MRI is currently implemented in the diagnosis and treatment of glioma, studies support the potential of ^{18}F-FDOPA to provide information additional to that obtained from MRI (Figure 2-3). Specifically, ^{18}F-FDOPA could provide further pathological information where MRI findings are negative in primary/recurrent tumours or inconclusive in recurrent tumours.

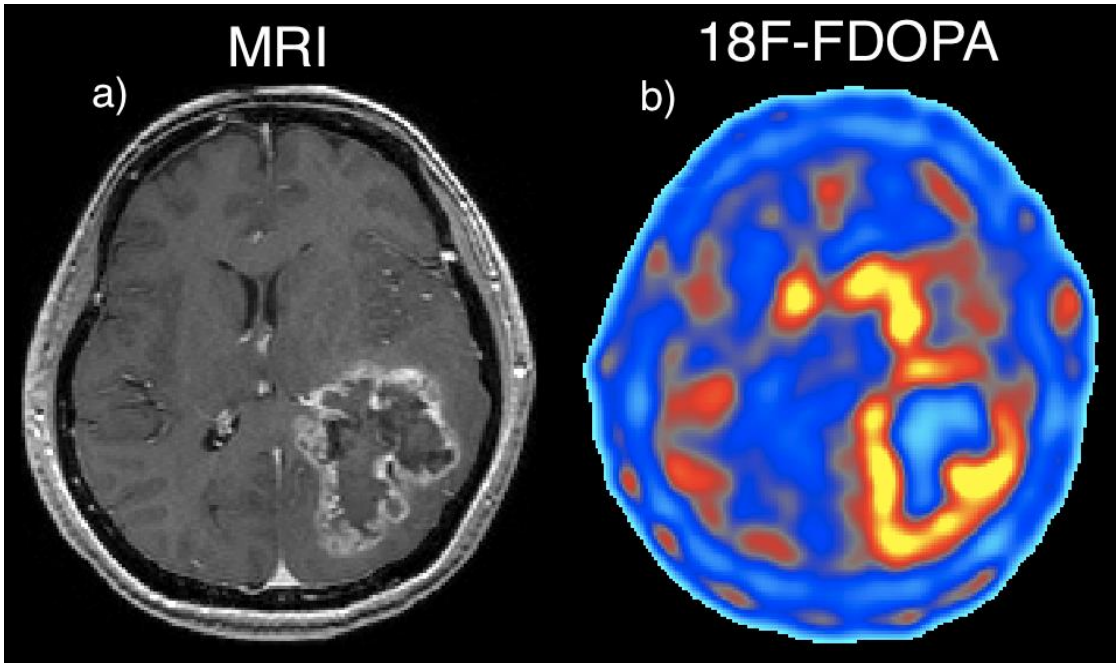

Figure 2-3 Figure 1 – a) Contrast enhanced MRI and b)^{18}F-FDOPA imaging of a primary high-grade glioma (grade IV – GBM).

Patient prognosis

The ability to predict patient prognosis and response to therapy is of great importance. Currently, several factors such as Karnofsky performance status (an assessment tool for functional impairment; KPS), age, tumour size, extent of surgery, tumour grade and histology are used in predicting patient survival (51, 52). Previous studies have shown that ^{18}F -Fluorodeoxyglucose (^{18}F-FDG) is also effective in predicting survival in primary and recurrent glioma patients (53, 54). However, the low specificity of ^{18}F-FDG PET is a limitation. The idea that a link exists between hypoxia and patient life-span is not new and comes from the suspected link between radiation treatment, vasculogenesis, cancer stem cells (CSC), infiltration and hypoxia (24, 25, 55-57). As such, various prospective studies have been performed to evaluate the intratumoural partial pressure of oxygen (pO_2) values on the outcome of tumour patients since the development of polarographic electrodes in the late 1980's, with numerous studies specific to investigating ^{18}F-FMISO PET and hypoxia (46, 47, 58-64). These studies provide evidence for a relationship between hypoxia, as measured by ^{18}F-FMISO, and patient survival. This body of work is in agreement with a multitude of other cancer studies suggesting the relationship between hypoxia and prognosis exists (16, 17, 59, 65-70).

A further study also suggests a link between ^{18}F-FDOPA and patient prognosis, proposing that increased ^{18}F-FDOPA uptake is predictive of reduced patient survival in cases of recurrent glioma (71).

Glioma grading

While anaplastic and mitotic activity exists in all grade gliomas, necrosis is not present in lower grade neoplasms due to the less aggressive conditions within the core (72-75). Confirmation of a GBM diagnosis generally involves surgical biopsy or resection, followed by a pathological assessment to determine tumour microvascularity, although there are concerns for this approach (9). Firstly, biopsy is an invasive procedure and is sometimes not possible due to the anatomic location of the tumour or the condition of the patient. Secondly, as biopsy tissue samples often represent only a small part of the entire tumour, there is a chance that the true tumour grade will be underestimated (76). Thirdly, surgery

of certain regions may involve surrounding normal brain tissue, exacerbating the prognosis by causing additional neurological morbidity or dysfunction (77).

In contrast to biopsy and resection, current research suggests that the use of ^{18}F-FMISO imaging may provide the ability to distinguish GBM from lower-grade gliomas *in vivo* (63, 64, 78-80). Furthermore, there is some evidence that ^{18}F-FDOPA can assist in tumour grading, though further research is needed before conclusions can be drawn confidently (33, 37, 81, 82). The ability to link glioma grade to *non-invasive* studies has clinical significance, even if employed only to aid guidance of tumour biopsy.

From this body of research, it is clear that *in vivo* imaging of glioma using 18F-FMISO and 18F-FDOPA PET is of importance, especially with the introduction of new hypofractionated stereotatic image-guided helical tomotherapy, where hypoxic tumoural regions can be treated with higher doses. Tomotherapy, as a salvage regime for recurrent high-grade gliomas, has shown promising results for improving patient survival (83). This suggests that the need to image more than one PET tracer is evident: Imaging with ^{18}F-FMISO and ^{18}F-FDOPA PET provides valuable information not obtainable using either one individually. Although offering the potential to improve characterisation of tumour volumes, imaging multiple PET tracers is not often adopted due to technical and logistical constraints. As PET scanners cannot differentiate between individual tracer decay events, imaging more than one molecular target would require multiple PET acquisitions with a large enough temporal gap between them to prevent cross contamination. This approach not only increases scanner and specialist time, the poor health of patients may preclude multiple scans from being performed. Furthermore, higher grade gliomas are known to be fast progressing, suggesting that even a short temporal gap between independent scans may result in physiological changes in the tumour and underlying biology. Finally, individual acquisitions required registration, adding another source of potential uncertainty.

Dual-Tracer PET imaging

An alternative to performing multiple PET acquisitions is dual-tracer PET imaging, where both radiotracers are imaged within a single scanning session. Implementation of this technique could allow for information on multiple biological factors such as hypoxia and metabolism to be obtained within a single scanning session, potentially providing the same benefits as two single scans, while circumventing some of the logistical issues. Previous studies have suggested the potential of dual-tracer PET imaging. Huang proposed

exploiting the different decay rates of distinct isotopes to separate the signals once a biological steady state had been reached (5). Kadrmas *et al* implemented a novel method that combined distinct tracer half-lives with the biological kinetics of each tracer to separate 18F-FDG, 64Cu-ATSM, 64Cu-PTSM and 11C-acetate signals (84). Here, PCA was used to examine mean signal separability as a function of injection delay and extract individual tracer signals; parameters were solved for a combined, pre-defined multi-compartment mode. Figueiras *et al* evaluated a simultaneous dual-tracer technique method that exploits the difference between the half-lives of ^{18}F-FDG and ^{13}N-ammonia in phantoms and an *in vivo* rat model of cerebral ischemia (85). Their model can be applied to the sinogram[1] data or directly to reconstructed image data. Kadrmas *et al* performed an investigation using distinct tracer half-lives combined with biological kinetics to separate FDG, diacetyl-bis(N(4)-methylthiosemicarbazone) (ATSM), pyruvaldehyde-bis(N4-methylthiosemicarbazone) (PTSM) and acetate signals (84). In addition to exploiting the difference in tracer metabolic half-lives, Verhaeghe *et al* implemented a staggered injection interval between the two tracers in conjunction with a basis function separation method for the extraction of information from dual-tracer dynamic ^{18}F-FDG and ^{15}O-H_2O acquisitions (86). Ikoma *et al* also relied on staggered injection intervals combined with kinetic modeling to assist in the separation of ^{18}F-FDG and ^{11}C-flumazenil (^{11}C-FMZ) signals (87). Koeppe *et al* demonstrated that a gap between tracer injection allows three ^{11}C-based tracers with the same isotope to be separated when using a two compartment kinetic model for each tracer (88). Kadrmas *et al* further investigated dual-tracer imaging by evaluating a kinetic model to separate ^{18}F-FLT and ^{18}F-FDG signals from dual-tracer simulations and *in vivo* studies of brain tumours (89). More recently, Zhang *et al.* proposed a method for separating two PET tracers using an extension of separable parameter space kinetic modelling to reduce the dimensionality of an otherwise complex non-linear fitting *(90)*.

Two studies have been performed investigating performing signal separation at the reconstruction level. Gao *et al* presented a technique where the kinetics of two tracers are used to constrain PET reconstruction (91). Cheng *et al* presented a novel method where a reduced-parameter dual-tracer kinetic model is incorporated into the reconstruction method to extract parametric maps (92).

[1] The raw data collected during PET scanning is stored as a sinogram file, containing the count averages during each predefined time frame.

Finally, there has been some research into the field of triple coincidence PET imaging. Unlike the typical case, where double coincidences (a positron-electron annihilation event) are detected by the scanner, triple coincidence PET relies on detecting the additional gamma prompts that occur in the decay of some isotopes, and their inclusion in image reconstruction to enhance signal to noise ratio (93). With this in mind, separation of dual-tracer signals could be performed using this third particle. However, the limitation with this approach is that triple coincidences are not guaranteed, and thus cross contamination of the signals is possible. In addition, the selection of tracers is limited to those where one (only) emits the third particle.

These techniques establish dual-tracer PET imaging as a potential alternative to performing multiple PET acquisitions. Yet despite the potential utility of dual tracer techniques, they are not widely used, possibly because existing methods either:

- Require each tracer to have a distinct half-life or radio-isotope, limiting the selection of available tracers. Each tracer has a specific half-life depending on the radio-isotope attached to the tracer. These methods are inappropriate for hypoxia/infiltration imaging, as both ^{18}F-FMISO and ^{18}F-FDOPA are ^{18}F radiotracers, and thus both have a half-life of 109 minutes.
- Require the particular pharmacokinetic model to be specified to calculate parameters. Pre-defining a model can be a disadvantage when a model has not yet been developed for a new tracer, or where different models apply to different tissue regions within the field of view.

Given these potential limitations, there is an inherent need to provide a set of dual-tracer frameworks to assist the study designer in selecting the most appropriate set of protocols for effectively performing dual-tracer imaging. In the following chapters, methods for performing dual-tracer imaging are presented that attempt to circumvent these limitations and move the current work in dual-tracer imaging towards clinical translation.

Chapter 3 – Dual acquisition of ^{18}F-FMISO and ^{18}F-FDOPA

Introduction

Previous work demonstrates the potential of dual-tracer PET imaging for providing valuable metabolic information while circumventing some of the logistical issues of acquiring multiple PET scans. However, these methods are restricted to separating signals by either requiring that each tracer has a different half-life and exploiting the temporal difference, limiting the application to certain tracer combinations, or performing a full dynamic acquisition from the injection of the first tracer, significantly increasing the required scanner time. Given the potential value of combining information about tumour metabolism with hypoxia, this chapter considers the case of combining ^{18}F-FMISO with ^{18}F-FDOPA and consists of the published paper "Dual acquisition of ^{18}F-FMISO and ^{18}F-FDOPA". Since ^{18}F-FMISO uptake can be considered stable after the 2 to 4-hour post-injection interval typical of most studies, there exists the possibility of estimating the ^{18}F-FMISO signal from a single frame prior to the injection of ^{18}F-FDOPA, removing the need to scan from the injection of the first tracer (^{18}F-FMISO).

Recent work has suggested that kinetic parameters obtained from dynamic ^{18}F-FMISO scanning can provide more salient information about the hypoxic regions than static images taken 2-4 hours post-injection (94). Even so, as kinetic analysis is not necessarily standard in the clinical setting, this chapter restricts itself to considering the case where two static frames are acquired, one pre-injection of ^{18}F-FDOPA and one post-injection.

The additional error introduced when performing dual-tracer imaging is dependent on the stabilizing time of the first tracer (^{18}F-FMISO), tracer dynamics and the isotope half-life. Many of these factors can be controlled, implying that error can be mitigated by the appropriate design of the injection and scanning protocol. Hence, a trade-off between logistics and signal accuracy exists. In the proposed approach, simulations covering ranges of known temporal distributions of ^{18}F-FMISO and ^{18}F-FDOPA are generated and realistic levels of noise are added. The contrast and bias for a range of dual-tracer imaging protocols are compared to imaging on separate days to investigate the effect of dual-tracer imaging. The framework is demonstrated using both theoretical simulations of uptake in glioma and real image data obtained from a preclinical study.

Materials & Methods

Modelling of PET activity using Kinetic Models

The temporal evolution of a radiotracer can be simulated using time activity curves (TACs), derived from kinetic parameters previously calculated. For example, previous reports have shown that tracers such as ^{18}F-FMISO and ^{18}F-FDOPA activity concentrations can be modelled within the brain using irreversible two-compartment and reversible two-compartment models, respectively (95, 96). Kinetic analysis is frequently formulated as the numerical solution to a set of ordinary differential equations taking reaction rate constants that model inter-compartment flow, k_1 to k_4, as parameters:

$$\frac{d}{dt}\begin{pmatrix} C_1 \\ C_2 \end{pmatrix} = \begin{pmatrix} k_1 & -k_2 - k_3 & k_4 \\ 0 & k_3 & -k_4 \end{pmatrix}\begin{pmatrix} C_p \\ C_1 \\ C_2 \end{pmatrix} \quad \text{3-1}$$

A two compartment model is illustrated in 3-1Figure 3-1. To model irreversible activity, k_4 is set to zero. The plasma concentration, C_p, does not necessarily include all of the activity in the blood, which may also contain metabolites. Thus, the blood concentration, C_b, is modelled as an additional variable, related to C_p. The time activity curve is obtained by linearly combining the compartments with the blood concentration to obtain the activity concentration(C) of the tracer at a given point in time:

$$C(t) = C_b(t) + C_1(t) + C_2(t) \quad \text{3-2}$$

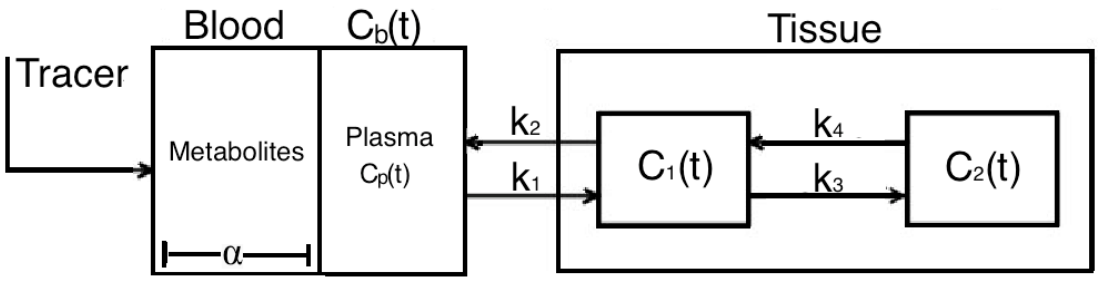

Figure 3-1 A model with three compartments. $C_b(t)$, $C_1(t)$ and $C_2(t)$ represent activity concentration as a function of time in the blood, metabolic compartment one and metabolic compartment two, respectively. $C_p(t)$ is the activity concentration of the tracer within the plasma, a fraction of blood activity determined by the metabolite fraction (α) calculated using Figure 3-3 and Figure 3-4. The kinetic parameters k_1, k_2, k_3 and k_4 are reaction rate constants representing the flow between compartments defined by real data, and depend on the tracer and tissue combination. k_4 is set to zero for irreversible models.

In some studies, the plasma concentration is obtained using arterial blood sampling. However, this is invasive and sometimes impractical to obtain clinically, especially if patients are severely ill. Hence C_b can be estimated from an available image by averaging the activity in the hottest voxels within the carotid arteries, and a previously established model for the relationship between C_b and C_p can be used(96):

$$C_p(t) = (1-\alpha)C_b(t) \quad \text{3-3}$$

$$\alpha = 0.6(1-e^{-0.08t}) - 0.1e^{0.01t} \quad \text{3-4}$$

where t represents the time after injection of the tracer in question and α represents the fraction of metabolites in the blood. Treating C_b and C_p as separate variables is necessary because in long scans, metabolites of tracers such as ^{18}F-FDOPA form a significant fraction of activity (96). Radiolabeled metabolites of the parent tracer are a problem for quantitative analysis of ^{18}F-FDOPA PET images, as they confound the true uptake of the parent tracer in the tissue. Therefore, correction of the ^{18}F-FDOPA PET signal is necessary. Where arterial sampling is unavailable (as is typical in hospital environments) empirical correction from population based measurements can be used, albeit with the assumption that metabolites accumulate at similar rates across the population. For the FDOPA signal the empirically established Equation 3-4 from Schiepers et al., with equation constants adopted from Huang et al (96, 97), was used. ^{18}F-FMISO metabolites within the blood are assumed to be negligible, due to the long post injection delay relative to the tracer kinetics.

For ^{18}F-FDOPA, blood activity concentration was obtained from post-processed patient PET data with metabolite correction performed as per 3-3 and 3-4. A "training" ^{18}F-FMISO scan was not available, so the ^{18}F-FDOPA blood activity concentration was directly reused for ^{18}F-FMISO. This makes the assumption that, although the main clearance pathway of ^{18}F-FMISO differs from ^{18}F-FDOPA (renal for ^{18}F-FDOPA(98); hepatobiliary for ^{18}F-FMISO(99)), the rapid drop off in blood activity is comparable to that of ^{18}F-FDOPA.

Table 3-1 - Kinetic reaction rate constants used for simulation of ^{18}F-FDOPA and ^{18}F-FMISO time activity curves for "typical" biological scenarios. Constants for ^{18}F-FDOPA were obtained from available clinical data and constants for ^{18}F-FMISO were obtained from literature(100).

Variable	FMISO- "Hypoxic"	FMISO+ "Normoxic"	FDOPA+ "Tumour"	FDOPA- "Normal/Cerebellum"
Typical uptake [SUV]	0.95 (101)	1.1 (101)	2.7 (37)	1.1 (37)
k1	0.300	0.300	0.225	0.124
k2	0.450	0.450	0.169	0.199
k3	0.008	0.001	0.031	0.075
k4	0	0	0.016	0.010

Regarding terminology, several terms are used to refer to signal measurement and need explanation. *Activity concentration,* refers to the concentration of the tracer at a given point in time, *C(t)*. *Total counts* or *signal intensity*, *I(t)*, is used to define the activity concentration integrated over a given time period, such as a PET frame or PET scan:

$$I(t_{start}, t_{end}) = \int_{t=t_{start}}^{t=t_{end}} C(t) \cdot e^{-\lambda t}\, dt, \qquad 3\text{-}5$$

where λ is the decay constant of the tracer (or ~ln(2)/110 minutes for ^{18}F). The defined terms are used to refer both to individual voxels and regions of interest, the latter of which is equivalent to integrating over a volume. Experiments were performed both at the voxel scale and over entire regions of interest; the scale is indicated in each case.

Each tracer is simulated independently using kinetic parameters shown in Table 3-1. An injection interval (T) is added to the ^{18}F-FDOPA simulation (by pre-concatenating the ^{18}F-FDOPA simulation with zeros) and the two simulations are summed as illustrated in Figure 3-2. The scanning time after injection of ^{18}F-FDOPA is symbolised by T_{post}. In the convention used here, t = 0 indicates the time of injection for the first tracer. A second time

factor, τ, is used to define a time interval between the commencement of scanning and the second injection. In this work, the signal intensity during two time intervals is of interest:

A single frame prior to injection of ^{18}F-FDOPA, where solely ^{18}F-FMISO is responsible for the signal:

$$I_{FMISO} = I(t - \tau, t)$$

A single frame after injection of ^{18}F-FDOPA, where both tracers are responsible for the signal:

$I_{combined} = I(t, t + T_{post})$.

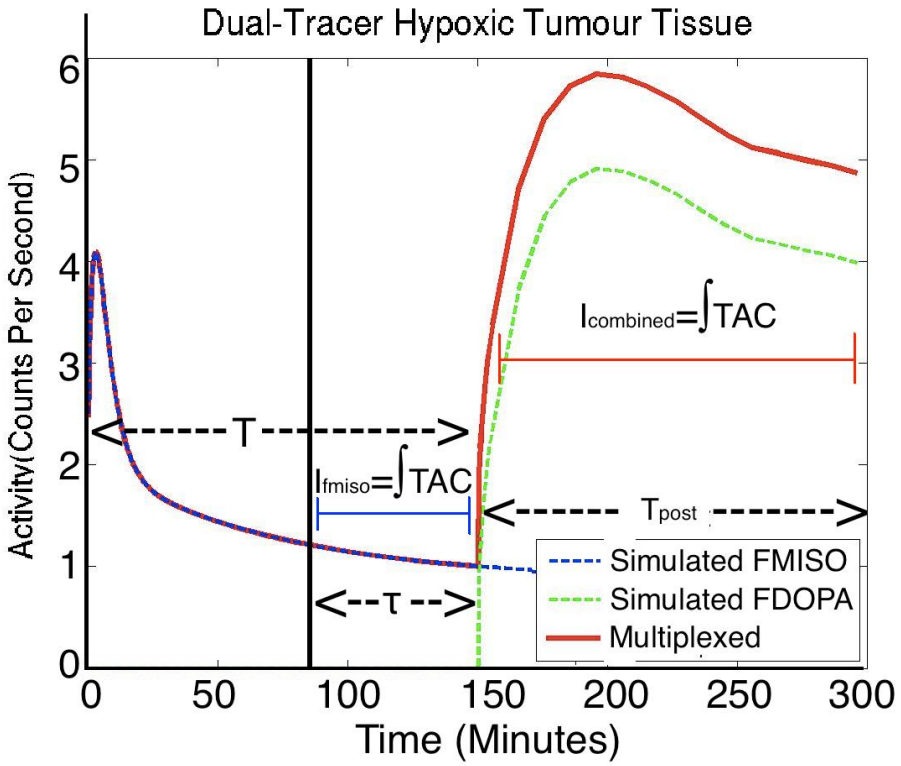

Figure 3-2 - Example of time activity curves for a single voxel in hypoxic tumour tissue illustrating the combination of ^{18}F-FMISO and ^{18}F-FDOPA activity when performing dual-trace imaging.

After activities for each of the two signals are computed, measurement noise is introduced. Previous studies report that noise within iteratively reconstructed dynamic PET images follows a multivariate log-normal distribution (102, 103). However, at higher counts this distribution is approximately Gaussian, which has been used previously to simulate noise

in reconstructed PET signals (89, 100, 104-106). In this study, noise is introduced by sampling from a Gaussian distribution with standard deviation, σ, equal to:

$$\sigma = c\sqrt{\frac{Ie^{\lambda t}}{\Delta t}}, \qquad 3\text{-}6$$

where the noise constant *c* is used to account for the noise characteristics of the scanner being used and Δt is the frame duration. Once again, *I* is used to represent the PET frame. The scanner specific constant c is a scalar used to control for differences in scanner sensitivity. It can be estimated by performing kinetic analysis on data and comparing the fits, *F*, to the original activities:

$$c = \mathcal{M}\left\{\frac{\sigma(I-F)}{\sqrt{\frac{Ie^{-\lambda t}}{\Delta t}}}\right\}, \qquad 3\text{-}7$$

The noise constant was obtained by performing a two compartment kinetic analysis of a dynamic ^{18}F-FDOPA scan. Only image regions above a given threshold were processed in this way. The threshold was selected to ensure the entire head was included but air was excluded. The sum of square error between the data and the best kinetic analysis fit was computed throughout the volume. The error volume was examined for high error regions, which were indicative of poor fits and these regions were excluded. Finally image intensity and the fit errors were summed over the remaining regions to solve for the noise constant, *c*, using 3-6. From this analysis, a value of 104.5 was found. Wang *et al* (100) used a value of 150.

Quantifying the error induced by combining two signals

To represent the biological variations typical of heterogeneous tumours, four representative scenarios were considered, schematically illustrated in Figure 3-3: hypoxic tumour tissue (high mean activity for both tracers), hypoxic non-enhancing tumour tissue (high mean activity of ^{18}F-FMISO only), normoxic tumour (high mean activity of ^{18}F-FDOPA only), and normal brain tissue (low mean activity for both tracers).

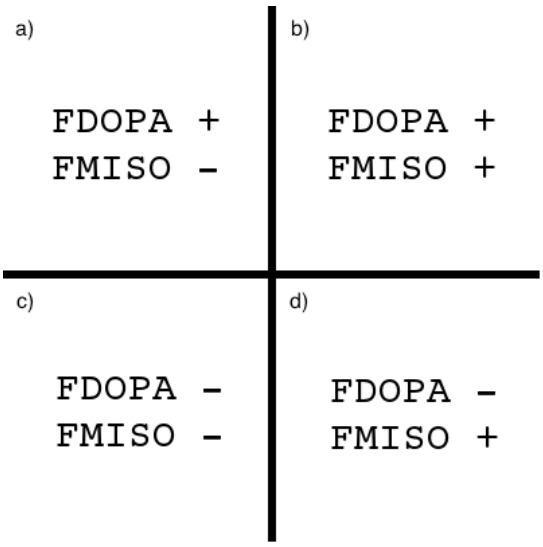

Figure 3-3 - Four broad categories of ^{18}F-FDOPA and ^{18}F-FMISO activity: (a) normoxic tumour, (b) hypoxic tumour tissue, (c) normoxic brain tissue and (d) hypoxic non-enhancing tumour tissue tissue.

For each biological scenario, signal fidelity was assessed in four ways:

- the ability to distinguish high and low ^{18}F-FMISO uptake (hypoxic and normoxic tissue) using relative contrast,
- the ability to distinguish high and low ^{18}F-FDOPA uptake (tumour and normal tissue) using relative contrast,
- the bias in^{18}F-FDOPA measurements caused by residual dynamics within the ^{18}F-FMISO signal, and
- the additional variance in ^{18}F-FDOPA measurements arising from ^{18}F-FMISO activity.

Relative contrast between two tissues was measured in units of standard deviations of noise of the higher magnitude signal:

$$S = \frac{|I_1 - I_2|}{\max(\sigma(I_1), \sigma(I_2))}. \qquad 3\text{-}8$$

Where I_1 and I_2 are the counts in the PET frame of the two tissues in question. This contrast measure was selected because it is normalised to the variations in noise arising from changes in signal intensity, which are in turn dependent on the choice of protocol. This choice of S allows the contrast for the continuum of protocols (in T and τ) and associated variations in signal intensity and noise to be presented in a single plot.

For comparison, tissue contrast values in the literature were adopted for ^{18}F-FMISO and ^{18}F-FDOPA (37, 101). SUV values from these studies were converted to activity in units of counts:

$$A = \frac{InjectedDose[Beql]*SUV[ROI]*e^{\lambda\frac{(t_{end}+t_{start})}{2}}*(t_{end}-t_{start})[s]*VoxelVolume[ml]}{PatientWeight[gm]/DensityOfWater[gm/ml]}, \quad 3\text{-}9$$

Reported ^{18}F-FMISO standard uptake values (SUV) for hypoxic and normoxic regions were of 1.1 and 0.95 respectively in Eschmann *et al* (101). The adopted ^{18}F-FDOPA SUV for tumour and normal tissue were 2.7 and 1.1 respectively from Pafundi *et al* (37). Here, a patient weight of 80kg is assumed. Activities were converted to contrasts using 3-5, resulting in ^{18}F-FMISO and ^{18}F-FDOPA baseline contrasts shown in the bottom rows of **Error! Reference source not found.** for reference (in the results). To represent the worst ase for a range of T and τ values, the contrast between low and high ^{18}F-FMISO uptakes were measured with high ^{18}F-FDOPA background, *i.e.* quadrants A and B in Figure 3-3. Also, the contrast between low and high ^{18}F-FDOPA uptakes were measured with high ^{18}F-FMISO background, *i.e.* quadrants B and D in Figure 3-3, for a range of T and τ values.

Bias in the ^{18}F-FDOPA signal can arise from residual dynamics in the ^{18}F-FMISO signal for the case where the ^{18}F-FMISO activity was assumed to be static. The bias is expressed as a percentage of the original ^{18}F-FDOPA signal and this effect is assessed for a hypothetical tissue expressing a high ^{18}F-FMISO activity with the lower ^{18}F-FDOPA activity typical of healthy (cerebellum) tissue, i.e. quadrant D in Figure 3-3. Tissues expressing these properties have longer ^{18}F-FMISO dynamics and lower ^{18}F-FDOPA signal, and so act as a "worst case" scenario.

Finally, the additional variance introduced by background ^{18}F-FMISO uptake to the ^{18}F-FDOPA signal was measured. This error is expressed as a percentage of the original ^{18}F-FDOPA signal and, as above, is assessed for a hypothetical tissue expressing a high ^{18}F-FMISO activity with the lower ^{18}F-FDOPA activity typical of normal (cerebellum) tissue (quadrant D in Figure 3-3).

To assist discussion, several *T*-τ pairs are used as reference protocols. Several studies into hypoxia have used acquisition time of 20 minutes dictating one choice of τ (47-49, 107). Minimising τ allows for the optimal use of scanner time, and thus τ = 1 minute was investigated as well. ^{18}F-FMISO stabilizing times of 2 hours and 4 hours post-injection have been proposed (47-49, 107, 108). Reducing the ^{18}F-FMISO stabilizing time also has

logistical implications, so a 30-minute ^{18}F-FMISO stabilizing time is also investigated. Hence three references for T were used: 0.5, 2 and 4 hours. These were combined with the two τ durations (1 and 20 minutes) to give six reference scenarios. Preclinical scans were used in addition to theoretical experiments to assist in validation. In the preclinical scans, *T*=120 minutes, so two additional protocols are used for reference: τ = 5, T = 120 and τ=10, *T*=120 minutes to give a total of eight reference protocols. The eight reference protocols each comprise a single point in a continuum of variations of *T* and τ, and are shown in columns two and three of **Error! Reference source not found.** in the results.

Imaging protocol

The assumed scenario is that the patient is injected with ^{18}F-FMISO and rests in a waiting room while ^{18}F-FMISO activity stabilises. Several minutes before injection of ^{18}F-FDOPA, the patient is placed prone on the scanner bed. Following a transmission CT scan, PET acquisition is initiated. After the pre-defined interval, τ, the ^{18}F-FDOPA bolus is injected while scanning continues. The patient would need to remain prone and not move. If movement does occur, registration is possible if enough anatomical structure is visible in the first image, or multiple CT scans are performed. The time of injection after scanning commences is recorded to allow the correct separation of the two static frames (pre- and post-injection of ^{18}F-FDOPA). For ^{18}F-FMISO, a dosage of 3.7 MBq/kg was adopted in previous studies (46, 48). For ^{18}F-FDOPA an activity of 2.05 MBq/kg is typical of the literature and the authors' institution and was assumed in this work (96). In the experiments, the total acquisition time is the ^{18}F-FMISO-only interval plus combined tracer interval, i.e. $\tau + T_{post}$. For the simulations T_{post} was assumed to be 75 minutes.

Several studies have shown that a static scan several hours post-injection suffices to identify hypoxic regions that retain ^{18}F-FMISO (28, 46, 48, 49, 63, 109-112). Two to four hours post-injection, biological steady state has been reached, hence the relatively stable signal. Thus, although an irreversible two-compartment model is used to *simulate* ^{18}F-FMISO signals, *measurements* of signal intensity are estimated assuming static activity during the time interval prior to injection of ^{18}F-FDOPA, τ, shown in Figure 3-2.

The assumption of static activity is in accord with several papers (28, 46, 48, 49, 63, 109-112) when reporting on ^{18}F-FMISO scans. The slow variation in ^{18}F-FMISO activity arises from the biological properties of hypoxic tissue, which prevents it from being metabolised and expelled. In normally oxygenated tissue ^{18}F-FMISO remains unbound, so the extended

interval between injection and scan ensures little, if any, unbound tracer remains. To reiterate, recent work has suggested kinetic parameters can provide more salient information about the hypoxic regions (94). The use of a static ^{18}F-FMISO frame several hours post injection is a trade-off to limit the amount of scanning time required.

The effects of varying dose and attenuation

Increasing the injection dose increases activity, and hence improves signal discrimination. However, protocols seek to avoid excessive radiation dose to the patient. The effect of dosage on signal discrimination was investigated by identifying for which T and τ there were above the baseline contrasts in the literature for individual voxels.

Similarly, signal attenuation varies with spatial location due to the density of the surrounding tissue. For completeness, typical attenuation values were obtained from a real CT scan of the human head using a GEANT4 (version 9.6.1) Monte-Carlo simulation as follows (113, 114). This approach was used, as opposed to measurements from a phantom, to check the extent to which skull thickness influenced attenuation as a function of spatial location. Multiple adjacent rings of detectors, each comprised of many crystals with the same geometry and arrangement as the Philips Gemini GXL scanner, were positioned around a 3D patient CT dataset. The full decay scheme of ^{18}F was simulated, with all radioactive decay products tracked throughout the CT dataset until either leaving the simulated scanner or hitting a detector. Atoms of ^{18}F were released and triggered to decay on a 200 mm cubic grid about the PET gantry centre at intervals of 5 mm in each of the 3 orthogonal directions. Ten thousand atoms were released at each point on the grid and an energy histogram of annihilation photons reaching the ring of detectors was scored. The two areas of minimum and maximum attenuation were identified and used to attenuate the simulated signals. This allowed for an observation of the effect of attenuation due to tissue density in both the least severe and most severe cases, providing for an estimation of the possible effects of attenuation on dual-tracer protocols.

Experiments using (real) preclinical data

As a proof of concept experiment, an investigation was performed using images of a NOD/SCID mouse bearing a U87 glioma cranial xenograph in the right striatum. U87 cells were maintained in RPMI160 medium (Gibco) supplemented with 10 % foetal bovine serum (Gibco), 2 mM L-glutamine, 25 mM HEPES, 25 mM sodium bicarbonate, 100 µg/mL

penicillin and 100 µg/mL streptomycin. Cells were cultured in 5 % CO_2 / 95 % humidified air atmosphere at 37 °C and used when they reached 70-80 % confluence. Cells (100,000 in 2 µl of PBS) were injected into the right striatum of 6-week old female NOD/SCID mice using a stereotaxic frame under isoflurane anaesthesia. Cells were injected at a depth of 3 mm, 1.6 mm caudal and 0.8 mm lateral to the bregma.

All animal experiments were approved by The University of Queensland Animal Ethics Committee. For synthetic dual-tracer experiments, mice were injected with tracer (5-7 MBq) intravenously via the lateral tail vein under isoflurane anaesthesia. Mice were maintained under 1-2 % isoflurane in an air-oxygen mixture at a flow rate of 2 L/min for the duration of the imaging session and monitored by a breathing pillow. Mice were positioned on the scanner bed (Bruker 7T Clinscan interfaced with a Siemens Spectrometer running Numaris/4 VB17 with a PET ring centred at the isocentre of the magnet consisting of 3 rings of 16 crystal blocks). 30 minute ^{18}F-FMISO and ^{18}F-FDOPA images were acquired on separate days, with the interval between scans large enough to allow complete washout and decay of the first tracer. For ^{18}F-FMISO, the 30 minute scan was acquired 120 minutes post-injection to reflect T = 120 minutes, allowing coverage of a range of scenarios. The preclinical data was used to perform a synthetic combination of the two data sets in list-mode format and subsequent separation after image reconstruction of two frames, one before and one after ^{18}F-FDOPA injection (i.e. when counts from the ^{18}F-FDOPA list mode file begin to be included). No spatial registration was performed in this experiment, as no software for list-mode registration was available. Hence no assumptions of biological correspondence could be made. However this does not obstruct the goal of this experiment, which was to ascertain the effect of dual-tracer imaging on the fidelity of the signals of the two signals. Therefore, only measurements in terms of signal fidelity were performed, and the original independently reconstructed images were used as a basis for analysis. In the real-world experiments no ground truth is available. At best, it can be assumed that the signal is the best estimate of PET activity that can be obtained with the hardware, albeit with error bounds that can be established. Hence experiments attempted to estimate bias with respect to the non-dual-tracer PET reconstructions (i.e. not the ground-truth) and that the variance in the signal estimates did not increase materially. Also given the manner in which PET scanners are read, where clinicians identify hyper-intensities within a noisy background sometimes in comparison to contralateral regions, results were usually reported in terms of contrast in units of signal standard deviation (which implicitly accounts for noise).

The list mode data were interleaved to reproduce the effect of dual-tracer imaging and then reconstructed using the original scanner software to produce images of the mouse. The list mode format was kindly supplied by Siemens (115). The ^{18}F-FMISO stabilizing time (T) was kept constant at 120 minutes and the pre-^{18}F-FDOPA scanning interval (τ) was set at 1, 5, 10 and 20 minutes, identical to a selection of the reference protocols. Tissue contrast and ^{18}F-FDOPA signal error were measured and reported for selective reference protocols. Although no spatial registration was performed, care was taken to ensure that the mouse was secured in the same position for both scans to maximise spatial alignment. Some movement did occur, but alignment was sufficient to ensure that synthetic exemplars of all permutations of low/high ^{18}F-FMISO/^{18}F-FDOPA occurred. Regions corresponding to hypoxic and normoxic ^{18}F-FMISO and tumour and normal ^{18}F-FDOPA uptake were manually drawn on the pre-clinical scans. Mean tissue signal was measured for the ROIs and the contrast of hypoxic-normoxic (^{18}F-FMISO) and tumour-normal (^{18}F-FDOPA) tissues was calculated and compared to simulated results. The fidelity of ^{18}F-FDOPA signals extracted from synthetically combined data was compared to the true signals and errors were reported as percentage of the true ^{18}F-FDOPA signal. Since the ROI mean activity (rather than summed activity) was used to calculate contrast, it is equivalent to a (class standardised) voxel level analysis.

In addition, an analysis of the individual voxels was performed on the preclinical data set within the ROIs defined above. Voxel values for true, single-tracer data was plotted against separated voxel values to examine their agreement with each other.

Results

The experiments described in the previous section can be summarised as follows:

- theoretical simulations using parameters derived from human images to establish the range of protocols giving sufficient signal fidelity at the voxel scale in Figure 3-4, Figure 3-5 and **Error! Reference source not found.**
- theoretical examination of the effects of varying dose in Figure 3-6 at the voxel scale
- separation of preclinical data synthetically combined in the list-mode format in Figure 3-7 and Table 3-3 for regions of interest means, and in Figure 3-8 and Figure 3-9 for individual voxels.

Theoretical experiments

The contrast between hypoxic-normoxic tissues and tumour-normal tissues is presented as a function of pre-^{18}F-FDOPA scanning interval, τ and ^{18}F-FMISO stabilization time, T in Figure 3-4. In Figure 3-4a, for each specific τ, a distinct optimum ^{18}F-FMISO stabilization time is visible. ^{18}F-FDOPA contrast improves as T increases, as shown in Figure 3-4b, while the pre-^{18}F-FDOPA scanning interval, τ, has a negligible effect.

The bias in the measured ^{18}F-FDOPA activity induced by residual ^{18}F-FMISO dynamics, presented in Figure 3-5a, decreases as the margin between stabilisation time and scanning interval increases. The cumulative improvements reduce with further increases in margin. The effect is expressed as a percentage of the simulated ^{18}F-FDOPA activity before noise is introduced. On the other hand, ^{18}F-FDOPA variance in Figure 3-5b, decreases both as T and τ increase, because increasing the scanning interval improves the accuracy of the estimate of ^{18}F-FMISO-activity and increasing the stabilising time reduces the ^{18}F-FMISO signal and hence its effect on ^{18}F-FDOPA. For the eight reference protocols, tissue contrast and ^{18}F-FDOPA error due to both ^{18}F-FMISO dynamics and statistical noise are shown in **Error! Reference source not found.**. For comparison, tissue contrasts for single-tracer imulations are also shown. In all cases, although the ^{18}F-FDOPA contrast decreased when performing dual-tracer imaging, the contrast exceeded the reference contrast from the literature. The ^{18}F-FMISO contrast required a scanning period of at least 10 minutes to reach the reference contrast from the literature, assuming scanner sensitivity similar to a Phillips Gemini. For reference, the noise standard deviation, as calculated by 3-6, for each reference protocol is shown in **Error! Reference source not found.**.

Table 3-2 - Full set of results from simulations for the eight reference protocols identified (a), which represent the imaging protocols, shown in (b). Contrasts are reported using units of noise standard deviations as an indication of ability to unambiguously separate adjacent voxels. Tissue contrasts for dual-tracer signals (c; after signal separation) are compared to single-tracer signals (d) for the same protocols. Note that tissue contrasts for ^{18}F-FMISO are identical for single- and separated-tracer contrasts, as the ^{18}F-FMISO scan is performed prior to the injection of ^{18}F-FDOPA, and is therefore unperturbed by dual-tracer imaging. Simulation signals and corresponding noise standard deviations, calculated from 3-6, are also shown for each reference protocol simulation to illustrate signal intensities (e). The right-most columns show the bias in the ^{18}F-FDOPA signal due to residual dynamics in the ^{18}F-FMISO signal (f), and the variance in the ^{18}F-FDOPA signal due to the additional noise introduced by the ^{18}F-FMISO signal (g). Contrasts obtained from the literature are also shown for comparison.

(a)	(b)		(c)		(d)		(e)		(f)	(g)
	Interval (min)		Dual Tracer Contrast (standard deviation of noise; higher is better)		Single Tracer Contrast (standard deviation of noise; higher is better)		Signal (Noise Standard Deviation; higher is better 3-6)		FDOPA Bias due to FMISO dynamics (% of FDOPA signal; lower is better)	Additional FDOPA Variance due to FMISO noise (% of FDOPA signal; lower is better)
Ref. Protocol	T (Injection interval)	τ (FMISO scanning time)	FMISO hypoxic-normoxic tissue	FDOPA tumour-normal tissue	^{18}F-FMISO hypoxic-normoxic tissue	^{18}F-FDOPA tumour-normal tissue	^{18}F-FMISO Hypoxia [counts]	^{18}F-FDOPA Tumour [counts]		
1	30	1	*Same as single tracer, because estimate prior to FDOPA*	44.58	0.36	51.8	183(183)	15570 (297)	9.46	35.65
2	120	1		46.95	0.58		163(148)		2.49	22.86
3	240	1		47.77	0.49		146(136)		0.45	14.87
4	30	20		44.58	2.78		4320(199)		17.9	7.68
5	120	20		46.95	6.79		2483(151)		3.40	4.86
6	240	20		47.77	5.82		2041(137)		0.62	2.87
7	120	5		46.95	1.90		606(149)		2.67	14.86
8	120	10		46.95	3.53		1222(150)		2.99	11.87
	Baseline Values from the literature									
Bib. Ref. (101)	120	14	Unavailable		3.40		SUV = 1.1 (normal)/0.95 (hypox.)			
Bib. Ref. (37)	10	20	Unavailable			35.80	SUV = 2.7 (tumour)/1.1 (normal)			

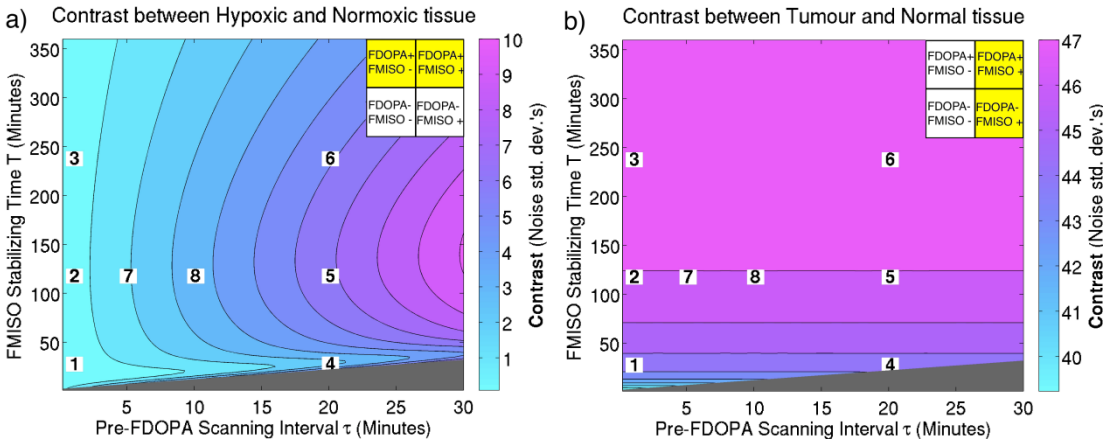

Figure 3-4 - **a)** Contrast between ^{18}F-FMISO signals in hypoxic and normoxic tissue types at a range of T and τ values. Higher contrast is better. Results are reported using units of noise standard deviations, as an indication of ability to unambiguously separate adjacent voxels. The grey triangle at the bottom of the image indicates protocols (Beginning scans prior to injection of ^{18}F-FMISO adds no information). **b)** Contrast of tumour and normal tissue based on ^{18}F-FDOPA activity for various T and τ values. Higher contrast is better. Results are reported in units of noise standard deviations of the larger signal (^{18}F-FDOPA).

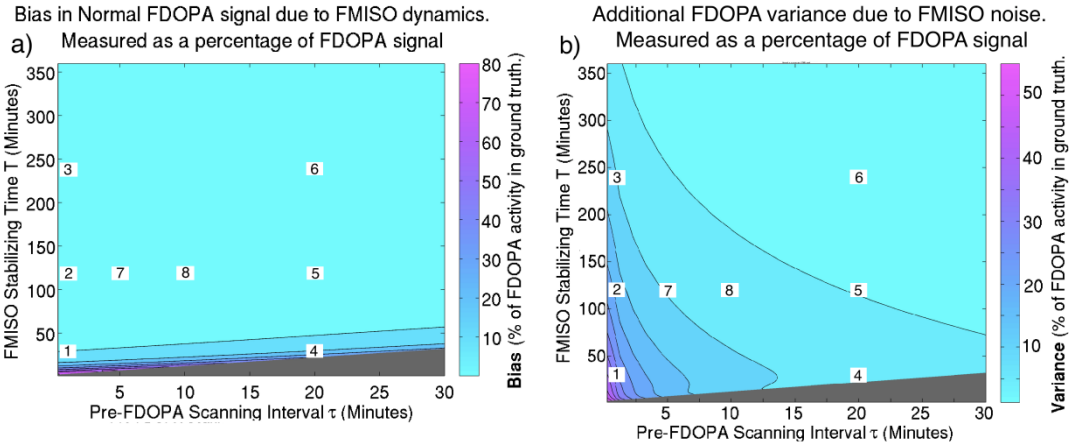

Figure 3-5 **- a)** Bias in the ^{18}F-FDOPA normal tissue signal imposed by residual dynamics in the ^{18}F-FMISO signal in hypoxic regions for various T and τ values. Bias is shown as percentage of the simulated ^{18}F-FDOPA signal. ^{18}F-FDOPA defined normal and ^{18}F-FMISO defined hypoxic tissue was chosen due to the low activity of ^{18}F-FDOPA and long dynamics of ^{18}F-FMISO signal, representing the worst-case scenario. **b)** Additional variance in the ^{18}F-FDOPA normal tissue signal added by the background ^{18}F-FMISO activity.

The effect of varying dose and attenuation

The improvements in ^{18}F-FMISO contrast resulting from increased ^{18}F-FMISO dosage are presented in Figure 3-6a. Here, contours were used to represent baseline contrasts for ^{18}F-FMISO taken from the literature. Increased ^{18}F-FMISO dose gives increased flexibility in the choice of protocol, *i.e.* T and τ can be reduced. Attenuation has a similar effect to varying ^{18}F-FMISO dose, as it also affects the measured signal by decreasing the signal-

to-noise ratio. However the effects are smaller than that of dose as shown in Figure 3-6b.

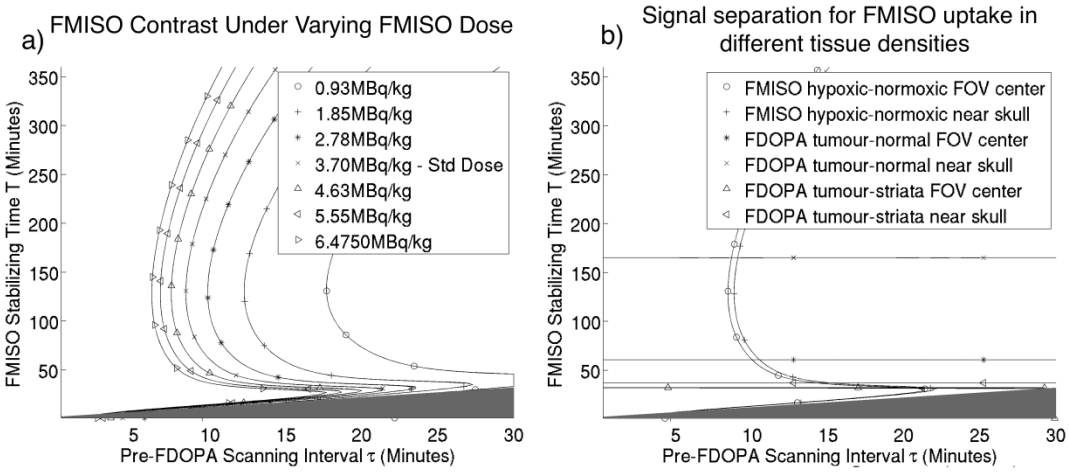

Figure 3-6 - a) The effect of varying injected 18F-FMISO dose on the 18F-FMISO iso-contrast line having the baseline contrast. b) The effect of attenuation for tumour and normal tissue. The lines shown are iso-contrast contours with the baseline contrast.

Validation using synthetic combination of list-mode data

This method was validated by applying it to a synthetically combined dual-tracer mouse model bearing a U87 xenograph in the right striatum. Results are shown in Figure 3-7 and Table 3-3 for reference protocols 2, 5, 7 and 8. The white outlines in Figure 3-7b and Figure 3-7c show activity in the olfactory system and salivary glands which were specifically excluded from statistical analysis. Two regions of interest within the brain were selected on each PET scan for a later experiment (Figure 3-8).

Figure 3-7b-c show the true ^{18}F-FMISO and ^{18}F-FDOPA data, which were acquired independently on separate days. Figure 3-7d shows this dual-tracer data. Since registration was not performed, no biological analysis can be made, only an analysis of signal fidelity.

In rows 2-5, the three columns respectively show the measured ^{18}F-FMISO activity, the estimated ^{18}F-FDOPA activity and the error in the ^{18}F-FDOPA estimate. Each row shows the results for τ ranging from 1 to 20 minutes.

^{18}F-FDOPA signal fidelity increases with increasing τ, but the decrease in error drops off after τ = 10 minutes, which is in accordance with findings in simulations. The quality of the ^{18}F-FMISO signal also increases with increasing τ.

Table 3-3 outlines the contrast of hypoxic-normoxic and tumour-normal tissues for reference protocols 2, 5, 7 and 8. Results from single-tracer scans (independently reconstructed) and simulation results are also shown for comparison.

For the ^{18}F-FMISO image, the selected regions of high and low ^{18}F-FMISO uptake are respectively indicated by magenta and green contours in Figure 3-7b. A voxel-wise comparison of the true and estimated ^{18}F-FMISO activity concentration is shown for each region in Figure 3-8 row 1, and using the same identifying colours. For the ^{18}F-FDOPA image, the selected regions of high and low metabolism are respectively indicated by the blue and red contours in Figure 3-7c. A voxel-wise comparison of the true and estimated ^{18}F-FDOPA activity concentration is shown for each of these regions in Figure 3-8 row 2, using the same identifying colours. At the voxel scale, the increases in relative bias and variance as the scanning interval (and hence activity) decreases are especially apparent for ^{18}F-FMISO, but are visible in ^{18}F-FDOPA as well.

In addition, to ensure that pre-clinical dual-tracer data reflects a large range of possible variations in signal, voxel activities for ^{18}F-FMISO are plotted against those of ^{18}F-FDOPA in Figure 3-9. All four permutations of signal strength shown in Figure 3-3 exist, indicating that the preclinical experiments have adequate coverage of the scenarios in Figure 3-3, and assuring that analysis can be performed without the need for spatial registration on the list-mode data.

Table 3-3 - Contrasts in ^{18}F-FMISO and ^{18}F-FDOPA signals for varying Pre-^{18}F-FDOPA scanning interval in simulated dual-tracer imaging of NOD/SCID rodent implanted with U87 xenograph. Also shown are contrasts from single-tracer data, obtained from the independently reconstructed scans, and dual-tracer-tracer contrasts from Table 3-1 for hypoxic-normoxic and tumour-normal tissue for the same protocols. The mean activity from each voxel was used.

	Interval (minutes)		Dual-Tracer Mouse Data Contrast (% noise std. dev.)		Single-Tracer Mouse Data Contrast (% noise std. dev.)		Simulated Dual-Tracer Contrast (% noise std. dev.)	
Reference Protocol	T	τ	FMISO "hypoxic-normoxic" tissue	FDOPA "tumour-normal" tissue	FMISO "hypoxic-normoxic" tissue	FDOPA "tumour-normal" tissue	FMISO "hypoxic-normoxic" tissue	FDOPA "tumour-normal" tissue
ROI →			Magenta	Green	Red	Blue		
2	120	1	*Same as single tracer.*	49.56	0.61	57.17	0.58	46.95
7	120	5		51.79	2.21		1.90	46.95
8	120	10		55.94	3.98		3.53	46.95
5	120	20		58.48	7.33		6.79	46.95

Baseline contrast values from literature				
(101)	120 14		3.40	
(37)	10 20		35.80	

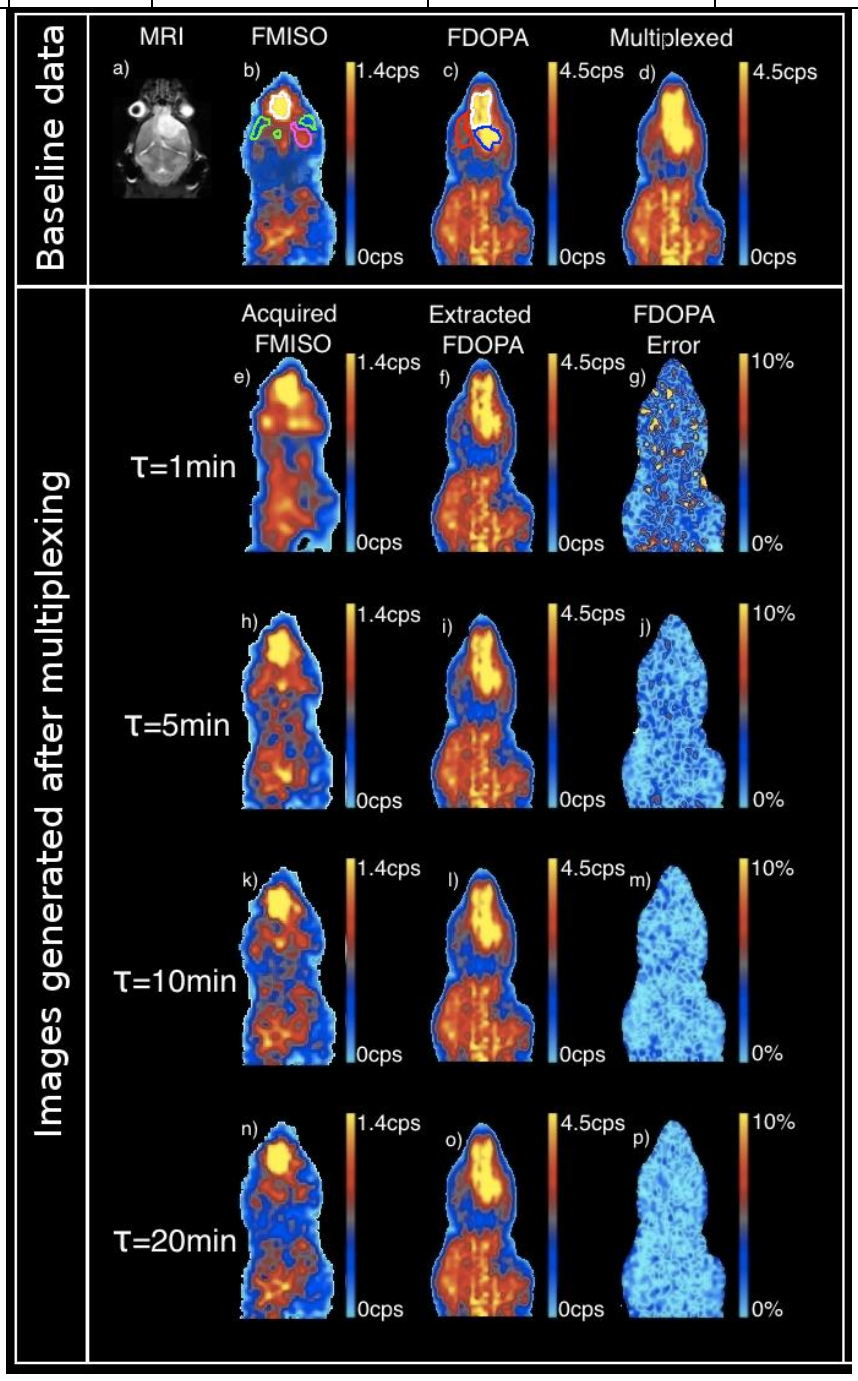

Figure 3-7 - Example dual-tracer imaging of 18F-FDOPA and 18F-FMISO signals acquired on a NOD/SCID mouse bearing a U87 glioma xenograph in the right striatum. The original 18F-FMISO and 18F-FDOPA signals (b and c, respectively) are interleaved using list mode data to simulate a dual-tracer acquisition (d). An 18F-FMISO stabilizing time (T) of 120 minutes was used. Rows 2-5 show the extracted 18F-FDOPA signal from the dual=tracer signal (f, i, l, o) for reference protocols 2, 5, 7 and 8. The 18F-FDOPA signal is extracted by subtracting the acquired 18F-FMISO signal (e, h, k, n) from the dual-tracer data (d). Errors in 18F-FDOPA signal (differences between true 18F-FDOPA and extracted 18F-FDOPA signal) are also shown (g, j, m, p). A T2 acquisition is shown in (a), indicating the location of the tumour volume. Magenta and green contours in (b) represent areas of high and low 18F-FMISO activity, respectively. Blue and red contours in (c) represent areas of high and low 18F-FMISO activity, respectively. These regions were test examples of hypoxic and normoxic (b) and tumour and normal (c) tissue types. The high activity shown in (b) and (c), signified by the white contours, is activity

due to the olfactory system and salivary glands and was not used in the analysis. Note that the subject was carefully placed in the same position on subsequent days, but image registration was not performed, so no biological analysis was performed.

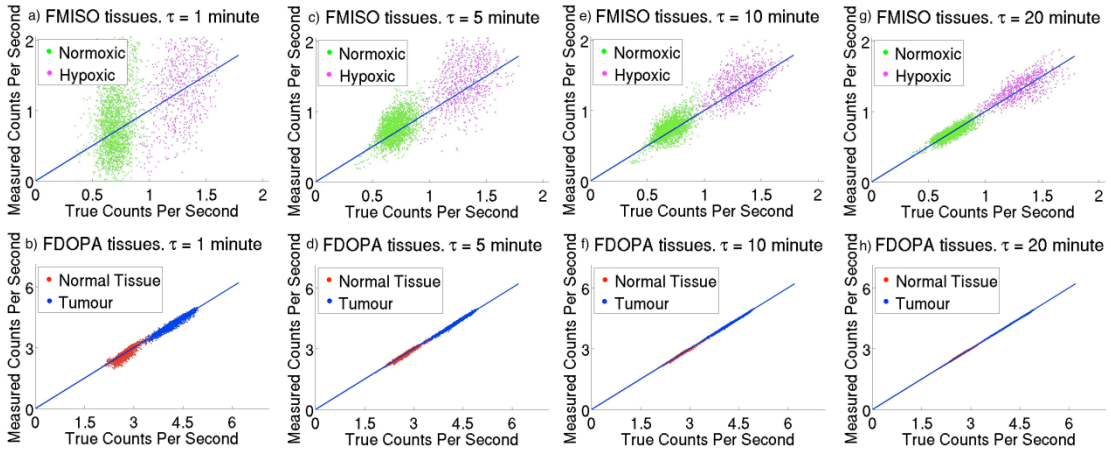

Figure 3-8 - Voxel-wise analysis of ROIs of sample data shown in Figure 3-7. Voxel values are plotted for true values (x-axis) as obtained from the single-tracer image versus extracted values (y-axis) as obtained from dual-tracer imaging. Each row represents the correlation between true and extracted values for reference protocols 2, 7, 8 and 5, respectively. Blue lines represent the line of perfect correspondence, where voxels on this line are identical between true and extracted data sets. As can be seen, extracted voxel values approach true values as τ increases. Lower count values for 18F-FMISO (a, c, e, g) due to a lower activity result in a more varied result than that of 18F-FDOPA (b, d, f, h). Note that no biological correspondence should be assumed for this data because the images were not registered.

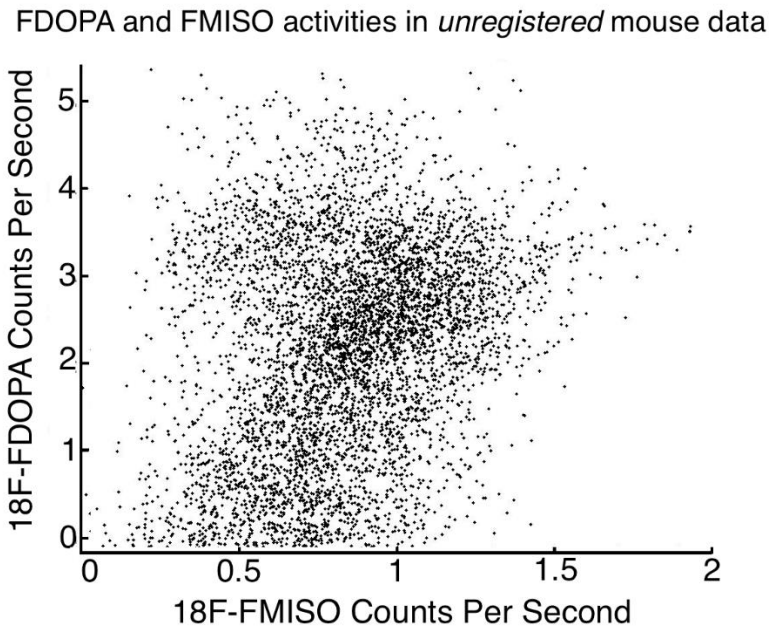

Figure 3-9 - Voxel values for ROIs used in analysis of real mouse data within the ROIs of sample data shown in Figure 3-7. ^{18}F-FMISO activities are plotted (x-axis) against ^{18}F-FDOPA activities for the same voxels. As can be seen, the range of voxels analysed included all four biological variations shown in Figure 3-3; ^{18}F-FMISO positive and ^{18}F-FDOPA negative representing hypoxic, non-enhancing tissue, ^{18}F-FMISO positive and ^{18}F-FDOPA positive representing hypoxic infiltrating

tissue, ^{18}F-FMISO negative and ^{18}F-FDOPA negative representing healthy tissue and ^{18}F-FMISO negative and ^{18}F-FDOPA positive representing normoxic infiltrating tissue. Note: no biological correspondence should be assumed for this data because the images were not registered. Hence these results solely show that all the scenarios in Figure 3-3 are covered for the purposes of validation.

Discussion

The imaging of both hypoxia and metabolism using PET has the potential to provide a better understanding of how biological factors in tumours affect treatment outcome. Such an understanding could assist in deciding what biology radiation therapy dose contours should conform to, and whether fractionation and dose should be adapted to dealing with acute hypoxia, chronic hypoxia or metabolism. In the clinical setting however, the potential utility of multiple metabolic modalities may be outweighed by the impracticality of performing multiple PET acquisitions on separate days. Performing dual-tracer imaging could overcome many practical issues, but this comes at a cost of signal accuracy. This chapter provides a framework for study designers to explicitly examine the potential additional error encountered when performing dual-tracer imaging and provides a method that allows imaging of multiple tracers where the dynamics of the first tracer can be assumed to be static at the injection of the second.

Unlike previous work which relies on (long) scans from the injection of the first tracer, this chapter focuses on a use-case more likely in clinical practice, where scanning commences from several minutes before injection of the second tracer and two static frames are reconstructed: one before and one after the second injection. Such a protocol could allow centers to maintain a similar patient throughput, despite using two tracers. It should be emphasised however, that the practicalities of *synthesising* two tracers on the same day also have additional logistical implications, which are outside the scope of this work.

In addition to the injected activity of ^{18}F-FMISO and ^{18}F-FDOPA, signal activity is controlled by three key factors:

- the pre-^{18}F-FDOPA scanning interval, τ,
- the ^{18}F-FMISO stabilizing time, T, and
- the local blood flow and tracer activity using the scaling factor, β.

A pre-^{18}F-FDOPA scanning interval that is too short does not allow reliable estimation of the hypoxic signal. For the noise model used, the signal-to-noise ratio decreases with the square root of the signal. Therefore, images with low intensity from short acquisitions

contain a higher fraction of noise compared to those of higher intensity, making them less statistically reliable. On the other hand, radioactive decay means that the signal intensity decreases after tracer injection, limiting the information gained by extending scan-time excessively. Hence both upper and lower limits on τ exist.

Shortening the ^{18}F-FMISO stabilizing time, *T*, has two negative effects. Firstly, the unbound ^{18}F-FMISO tracer has insufficient time to wash out of the normoxic tissue, which can result in false positives. Secondly, the ^{18}F-FMISO signal will not be at steady state when ^{18}F-FDOPA is injected, violating the assumption of relative stasis that allows ^{18}F-FMISO signal to be subtracted from the combined signal. Dynamic changes in ^{18}F-FMISO result in biased estimates of the ^{18}F-FDOPA signal. Lengthening *T* allows ^{18}F-FMISO activity to stabilize but has limited influence beyond a certain threshold because radioactive decay limits additional accumulation of ^{18}F-FMISO counts.

Several sets of experiments were performed to examine the range of scanning-injection protocols for which ^{18}F-FMISO and ^{18}F-FDOPA could be imaged within a single imaging session with sufficient accuracy. For this purpose, dynamic simulations for a range of ^{18}F-FMISO stabilisation intervals and ^{18}F-FMISO-only scanning intervals were performed, before subsequent integration to generate static signals of mean activity.

In the first set of theoretical experiments, the contrast between regions of high and low activity for ^{18}F-FMISO and ^{18}F-FDOPA was examined. The contrast in Figure 3-4a increases with scanning interval and there is a clear optimum for stabilisation interval for each scanning interval. This pattern arises from the trade-off between signal fidelity and scanning time, ensuring sufficient signal intensity from ^{18}F-FMISO and while excluding the large dynamics in the ^{18}F-FMISO signal immediately after its injection.

Considering the ^{18}F-FDOPA signal in Figure 3-4b, if ^{18}F-FDOPA uptake is high, relative contrast always exceeds 35.80 but never reaches the baseline contrast when no ^{18}F-FMISO signal is present. ^{18}F-FDOPA contrast is solely influenced by the stabilisation interval, because ^{18}F-FMISO activity decreases with increasing stabilisation interval. Scanning intervals above 90 minutes ensure ^{18}F-FDOPA contrasts (in high ^{18}F-FMISO regions) remain high.

The bias in the ^{18}F-FDOPA signal shown in Figure 3-5a remains low, so long as the stabilising interval exceeds the scanning interval by at least 30 minutes. This restriction

arises, because below this threshold dynamics in the ^{18}F-FMISO signal cause a positive bias in the ^{18}F-FMISO signal and a corresponding negative bias in the ^{18}F-FDOPA signal.

The variance from the underlying ^{18}F-FMISO signal is cumulative with the ^{18}F-FDOPA variance in the combined signal. Since the protocol only influences the ^{18}F-FMISO portion of the variance, only this is reported in Figure 3-5b. Variance decreases both as the scanning interval and the stabilisation interval increase. Increasing the scanning interval increases the accumulated ^{18}F-FMISO counts, hence the observed decrease in variance. Increasing stabilisation interval decreases the ^{18}F-FMISO signal and hence the decrease in variance added to the ^{18}F-FDOPA signal.

Scan intervals below 10 minutes have inadequate tissue contrast due to the low accumulation of ^{18}F-FMISO. Insufficient ^{18}F-FMISO counts also result in increased bias in the ^{18}F-FMISO and hence ^{18}F-FDOPA signals. The variance added to the estimated ^{18}F-FDOPA signal also increases. Stabilisation intervals of 120 minutes or more limit the variance induced in the ^{18}F-FDOPA signal. The protocol does not substantially influence the contrast between regions of high and low ^{18}F-FDOPA uptake. Thus, the limitations on protocol are imposed by the ability to distinguish hypoxic/normoxic regions, and limit ^{18}F-FDOPA bias and variance. Using contrasts from typical activity concentrations reported in the literature as a baseline does not impose onerous restrictions on the protocol. The baseline contrast levels can be satisfied by using a scanning interval of 10 minutes or more and a stabilisation interval that exceeds the scanning interval by at least 90 minutes, assuming scanner sensitivity similar to a Phillips Gemini scanner. Shorter scanning and stabilisation intervals would be possible on newer, more sensitive scanners.

Considering the influence of altering the ^{18}F-FMISO dosage, Figure 3-6a shows that the standard dosage can be reduced by a factor of two and still retain adequate contrast with changes in protocol that remain practical in certain clinical setting (e.g. T = 120min, τ = 25min). As shown in Figure 3-6b, the comparative influence of attenuation on the signal was relatively insignificant. Hence the spatial variation of attenuation within PET scans is of less concern when selecting protocol design.

To assess the validity of the theoretical results, tissue contrasts were measured using real images acquired from a NOD/SCID mouse bearing a U87 xenograph in the right striatum. Results from this experiment are reported in Table 3-3, with corresponding simulation results also shown for comparison. Tissue contrasts were measured for the reference

protocols 2, 5, 7 and 8 for two sets of paired regions: hypoxic versus normoxic tissue, and tumour versus normal tissue. Contrasts for dual-tracer mouse data were similar to values obtained from the simulations, with contrasts observed larger than those obtained in simulations in all cases. This suggests that the dual-tracer framework using simulations provides a conservative estimate of the range of protocols that will maintain adequate contrast and limit bias and variance in the FDOPA signal. The differences in contrast in the theoretical experiments and those measured in the image have several possible causes. The dose per kilogram administered to the mouse was not the same as that assumed in the experiments, and the metabolism of the mouse is more rapid than that typical for humans. Furthermore, the stage and genotype of the tumour could also play a role, as the U87 tumour line is a very aggressive model, designed to produce high-grade tumours in short periods of time. Finally, the noise parameter, *c*, used in the simulations was estimated for the Phillips Gemini scanner, not the Siemens Inveon scanner used for the mouse imaging. The former was used because blood activity concentrations adequate for kinetic analysis could only be obtained from the ^{18}F-FDOPA scan of humans, allowing c to be computed. Variations in dose and biology are typical in practice anyway, so some variation from simulation is to be expected. The key point when considering protocols is to ensure that the simulations are conservative enough that the selected protocol has some boundary for error, i.e. it is better to over-estimate c, and under-estimate activity concentration.

An example slice of the dual-tracer mouse model is shown in Figure 3-7, illustrating that as the scanning interval is increased, so does the fidelity of the ^{18}F-FMISO signal as well as the ability to extract the ^{18}F-FDOPA signal. The effect seen in Figure 3-5 where the increase in signal fidelity asymptotically approaches a maximum as the scanning interval is increased is also evident. The increase in signal fidelity between tau=10 to tau=20 is significantly lower than the increased between tau=1 to tau=5.

Voxel-wise analysis was also performed on regions defined by manually drawn ROIs. The voxel-wise analysis makes no assumptions about biological correspondence, as no registration was performed. Hence this experiment is synthetic in the sense that it measures signal loss only, but using real intensities and the full reconstruction pipeline that would be used in practice. Figure 3-8 shows that as τ increases, so does the reliability of the voxel values. The diagonal blue lines in the plots indicate the ideal case. The results in Figure 3-5, Figure 3-7 & Figure 3-8 show that for pre-^{18}F-FDOPA scanning intervals greater than 10 minutes, dual-tracer voxel values give similar values to the single-tracer case.

The analysis in the experiments is limited to four biological scenarios that were obtained from the literature. These scenarios were chosen to cover the typical range of possible biology under investigation and concisely define the trade-off between signal fidelity and clinical logistics. To show that real data analysis covered all four biological variations identified, ^{18}F-FMISO and ^{18}F-FDOPA voxel values for manually drawn ROIs were plotted in Figure 3-9. As shown, the ROIs from real mouse data covered a wide range of biological variations. It is conceivable that future work will reveal biological conditions outside the range of conditions tested here. In this event, the analysis could be repeated for the additional biological scenarios.

Residual dynamics will induce some bias, if a static FMISO signal is assumed. The bias depends on the FMISO gradient, which at one hour is relatively low hence the positive results reported here. These dynamics can be caused by the continued supply of remaining tracer from the blood. Figure 3-2 shows possible time activity curves generated using the adopted kinetic parameters and the blood activity concentrations shown in Figure 3-10a. However, some studies have shown continual binding of FMISO to hypoxic cells up to and past two hours post injection. Hence, for completeness, the experiments were performed again with the blood activity concentration shown in Figure 3-10c. Results from these experiments showed improved signal separation, suggesting that, although residual dynamics will affect the separability of these tracers, the results shown here are sufficiently conservative to represent possible residual ^{18}F-FMISO dynamics. Although the induced bias is low, accounting for FMISO gradient in the model has the potential to allow the injection interval to be reduced, and will be investigated in future work.

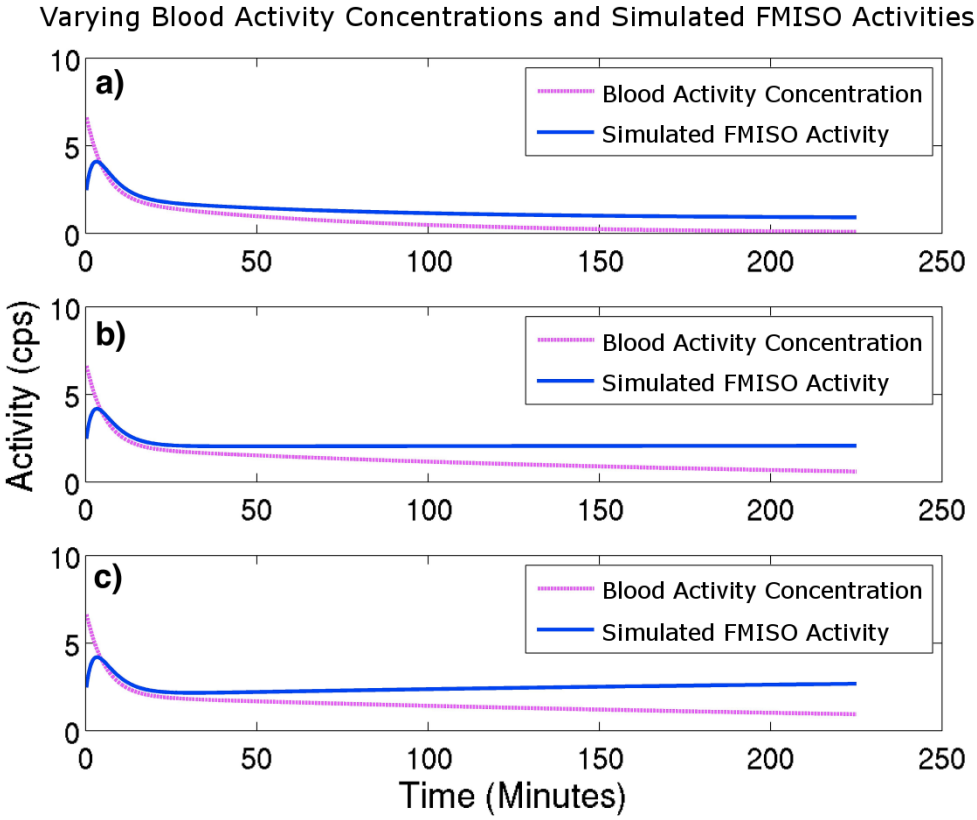

Figure 3-10 - Variations of the blood activity concentration (BAC) that allow simulation of different 18F-FMISO dynamics. The BAC shown in a) was adopted for this study and results in an 18F-FMISO time activity curve (TAC) where visual dynamics are due to wash out of the tracer from the diffused compartment. Simulation of 18F-FMISO using b) results in a perfectly static TAC. Simulation using c) results in a 18F-FMISO TAC where constant biding of 18F-FMISO within the cell (wash in to the trapped compartment) can be simulated. Experiments were also performed using this BAC, with results showing better tissue separation than a)

Recent work has suggested that kinetic parameters obtained from dynamic ^{18}F-FMISO scanning can provide more salient information about the hypoxic regions than static images taken 2-4 hours post-injection (94). While this approach may hold potential for providing additional information, the literature suggests that a short static scan suffices for identification of hypoxic regions (63, 78, 79). Also, the addition of a dynamic ^{18}F-FMISO scan to that of a dynamic ^{18}F-FDOPA scan would require a total dual-tracer acquisition in excess of 3 hours, which is not acceptable in many clinical settings.

It is important to note that the noise level within a signal is proportional to not only tracer activity, but also the scanner sensitivity. The experiments all assume performance equivalent to a Phillips Gemini scanner. More sensitive scanners would result in improved contrasts and hence a wider range of protocols.

Summary

For certain cancers such as glioma, the ability to examine multiple metabolic factors simultaneously could assist in understanding the reasons for local progression despite treatment. However, acquiring multiple PET scans is not practical in many clinical scenarios, hence the potential utility of dual-tracer PET imaging. Dual-tracer imaging has an impact on signal fidelity, so a trade-off between signal accuracy and clinical logistics exists. Even so, substantial scope exists to minimise operational impact while retaining sufficient signal fidelity. In the context of imaging hypoxia and tumour metabolism, this study has examined the trade-off between these factors. The influence of ^{18}F-FMISO stabilisation time, pre-^{18}F-FDOPA scan time and ^{18}F-FMISO dose were examined. Analysis showed that 90 minutes post injection the ^{18}F-FMISO signal is sufficiently stable for subtraction of the static ^{18}F-FMISO signal to give accurate estimates of the ^{18}F-FDOPA signal. The pre-^{18}F-FDOPA scan time should be at least 10 minutes in length, assuming scanner sensitivity similar to a Phillips Gemini scanner. As the ^{18}F-FMISO signal is typically low and relatively static by the time ^{18}F-FDOPA is injected, the increase in ^{18}F-FDOPA bias and variance, and the decrease in ^{18}F-FDOPA contrast relative to noise are not excessive. Results obtained from dual-tracer mouse data approximately concur with values generated from simulations. Some variation was expected due to differences in dosage, biology and scanner sensitivity. Residual dynamics will induce some bias, if a static FMISO signal is assumed. The bias depends on the FMISO gradient, which at one hour is relatively low hence the positive results reported here. Although the induced bias is low, accounting for FMISO gradient in the model has the potential to allow the injection interval to be reduced, and will be investigated in future work.

Substantial flexibility exists when selecting protocols for the purposes of combining ^{18}F-FMISO and ^{18}F-FDOPA. It is likely that dual-tracer imaging is practical in the clinic for other combinations of tracer and in different application areas, especially if techniques such as kinetic analysis and the pairing of distinctive isotopes are used.

While performing dual-tracer imaging using this approach is effective, it is restrictive in the sense that it cannot be applied when the dynamics of the first tracer are not static. Therefore, it would be useful to extend this methodology for dual-tracer imaging to the paradigms where dynamics of the first tracer are not static within the tissue during the entire imaging session. This leads to the next chapter of this thesis, where this approach is

developed further to include the case where the first tracer has some residual dynamics at the injection of the second.

Chapter 4 – Extension of static dual-tracer imaging to the case where first tracer dynamics are not at equilibrium.

Introduction

In the previous chapter, a framework for imaging two tracers simultaneously was developed, where it was assumed that the dynamics of the first tracer is at equilibrium at injection of the second. However, this assumption does not hold for all tracer combinations. This chapter develops the previous technique to allow pre-validation of static dual-tracer PET protocols where the first tracer continues to have linear dynamics during injection of the second with the specific case of a ^{64}Cu labelled monoclonal antibody specific to the EphA2 receptor tyrosine kinase (^{64}Cu-EphA2, nanomedicine) followed by ^{18}F-FDOPA (validation) considered. ^{64}Cu-EphA2 was chosen, as it has been shown to have slow uptake kinetics that persist for a number of hours(116). This concept is evaluated using a set of synthetic dual-tracer and true dual-tracer preclinical data sets. In addition to investigating this technique, there is also interest in whether the antibody based tracer, ^{64}Cu-EphA2 (EphA2 receptor tyrosine kinase), is taken up in regions of metabolically active infiltrating tumour as assessed by ^{18}F-FDOPA uptake. ^{64}Cu-EphA2 was chosen as overexpression of the Eph receptor tyrosine kinases (RTKs), specifically EphA2, has been shown to occur within glioblastoma (GBM) derived cell lines,(117-119) with EphA2 overexpression linked with poor patient prognosis.(120, 121) As such, EphA2 is an attractive therapeutic target for GBM.(122-125) In addition, the use of a monoclonal antibody allows, in principle, the application of the imaging methodology described here to any Immunoglobulin G (IgG) based nanomedicine as the pharmacokinetics of IgG structures are both slow and broadly similar.(126)

Materials & Methods

Radiotracer synthesis

Chemical reagents were sourced from Sigma Aldrich and were used as received. 1,4,7-triazacyclononane-1,4,7-triacetic acid was purchased from Macrocylics (Dallas, TX) and Amicon centrifugal filters were purchased from Sigma Aldrich. $^{64}CuCl_2$ was produced by

the Department of Medical Technology & Physics and RAPID PET Laboratories, Sir Charles Gairdner Hospital, Perth, Western Australia. ^{64}Cu-EphA2 was produced as previously described[29] ^{18}F-FDOPA was produced by Queensland PET, Royal Brisbane and Women's Hospital, Brisbane, Queensland.

Pre-clinical imaging protocols

In pre-clinical experiments, each mouse was injected with ^{64}Cu-EphA2 (5-7 MBq) and ^{18}F-FDOPA (5-7 MBq) via the lateral tail vein. 4 hours post injection, mice were anaesthetised and a cannula placed in the lateral tail vein. At 1 and 6 hours following injection, mice were positioned on the scanner bed in preparation for scanning.

For single-tracer imaging, thirty minute acquisitions were performed for both ^{64}Cu-EphA2 and ^{18}F-FDOPA, with imaging acquired on separate days to prevent cross-contamination. For true dual-tracer imaging, 60 minute ^{64}Cu-EphA2 acquisitions were performed, with ^{18}F-FDOPA injected via the cannula 40 minutes following the start of image acquisition. All PET images were reconstructed by a two-dimensional ordered subsets expectation maximum (OSEM2D) algorithm with no attenuation or scatter correction. In total five mice were imaged. Three mice were imaged twice respectively using ^{18}F-FDOPA and ^{64}Cu-EphA2 on separate days, with approximately a 24 hour gap between the scans to prevent cross contamination. Two mice were imaged when combining ^{64}Cu-EphA2 and ^{18}F-FDOPA. T_1-weighted MR imaging was also performed for each acquisition.

Synthetic dual-tracer imaging was performed on the acquired raw single-tracer PET list mode data, using the method outlined in the previous chapter. Two aspects were investigated by this synthetic dual-tracer method; the length of the PET acquisition before injection of the second tracer (pre-^{18}F-FDOPA imaging time, τ) and the voxel activity of each tracer. For synthetic dual-tracer imaging, the first frame window, τ, was varied at 1, 5, 10 and 20 minutes. True dual-tracer datasets were reconstructed unedited.

Separation of dual-tracer signals

The signals for ^{64}Cu-EphA2 and ^{18}F-FDOPA, respectively I_{EphA2} and I_{FDOPA}, are functions of time, *t*, and have decay factors λ_1 and λ_2. Again the terminology to differentiate between the activity of the tracer and the intensity of the signal in a PET frame are *C* and *I* respectively. In the frames after the injection of ^{18}F-FDOPA they are combined to form a dual-tracer signal:

$$I_{Multiplexed}(t) = I_{EphA2}(t) \cdot e^{-\lambda_1 t} + I_{FDOPA}(t) \cdot e^{-\lambda_2 t} \quad 4\text{-}1$$

To separate the dual-tracer signals post injection, two methods were used. The first was a linear model:

$$I_{EphA2}(t) = \beta\, t + \beta_o. \quad 4\text{-}2$$

The parameters β and β_0 can be estimated by performing linear regression on two or more frames prior to injection of ^{18}F-FDOPA. The second method assumes a static signal as described in the previous chapter where β was set to zero. Decay correction was applied during image reconstruction by assuming ^{64}Cu was the sole isotope and then correcting for ^{18}F decay post-reconstruction during the relevant image frames, after removal of the ^{64}Cu-EphA2 signal:

$$I_{FDOPA}(t) = \left(I_{Multiplexed}(t) - (\beta\, t + \beta_o) \cdot e^{-\lambda_1 t}\right) \cdot e^{\lambda_2 t} \quad 4\text{-}3$$

Thus, the radioactive decay of the tracers was removed from consideration. Here *t=0* is the time ^{18}F-FDOPA is injected and *t=-T* is the time ^{64}Cu-EphA2 is injected. Scanning commences prior to injection of ^{18}F-FDOPA at *t=-τ*. The imaging protocol and separating scheme are shown schematically in Figure 4-1.

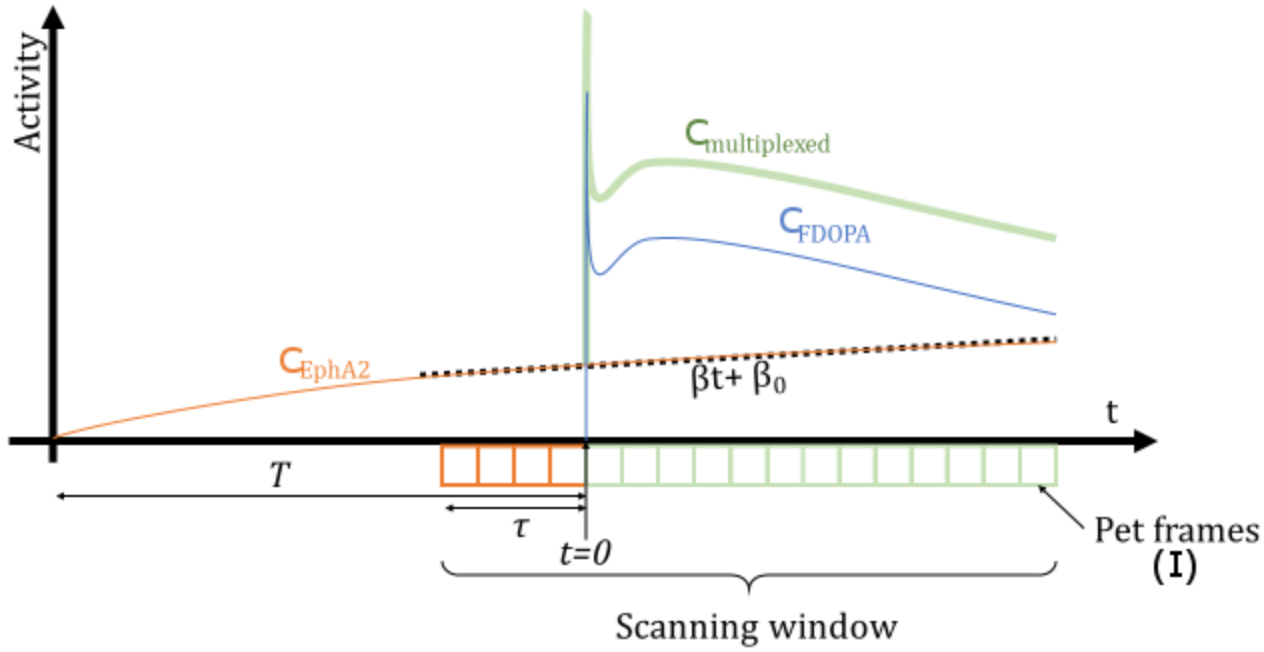

Figure 4-1 – Schematic diagram of the imaging protocol, showing injection of ^{64}Cu-EphA2 at t=-T. Scanning is initiated at t=- τ and at t=0 ^{18}F-FDOPA is injected. The activity of the tracers are represented by *C* and the intensity of the Pet signal for a given PET frame is represented by *I*. At least two PET frames are required between t=- τ and t=0, to calculate the

linear fit, $\beta\ t + \beta_o$, which is subtracted from $I_{Multiplexed}$ to obtain I_{FDOPA}. The effect of the two decay factors λ_1 and $\lambda_2$is no shown.

Image Analysis: Dual-Tracer signal error

For the three mice imaged on separate days, a map of ^{18}F-FDOPA error, ε, was calculated for each voxel in the image volume using the single-tracer ^{18}F-FDOPA data, $\bar{I}_{FDOPA}(t)$, as the signal of reference:

$$\varepsilon = \frac{|I_{FDOPA}(t) - \bar{I}_{FDOPA}(t)|}{I_{FDOPA}(t)} \qquad 4\text{-}4$$

where, as before, $I_{FDOPA}(t)$ denotes the ^{18}F-FDOPA signal obtained from dual-tracer imaging. Following this, cumulative error histograms were generated for the whole mouse volume for each separation method over the investigated range of τ and tracer activity.

Image Analysis: ^{64}Cu-EphA2-^{18}F-FDOPA spatial correlation

To investigate ^{64}Cu-EphA2 as a potential tracer, linear regressions across ^{18}F-FDOPA and ^{64}Cu-EphA2 voxel activities were performed individually for each of the five subjects, with the Pearson's correlation coefficients calculated to investigate the relationship between the two tracers. Regions of interest (ROIs) were drawn for active tumour using an acquired gadolinium contrast MR image. For the three mice imaged on separate days, the ^{64}Cu-EphA2 and ^{18}F-FDOPA images were reconstructed individually and rigidly registered using MILXView milxAliBaba.(127) To enable better inter-subject comparison, PET intensities were normalised to the cerebellum to generate tumour-to-normal ratio (T/N) maps.

Statistical analysis

Investigations were performed to determine if dual-tracer imaging produces statistically different results to that of independent imaging. Pairwise t-tests were performed to determine the similarity in relationship between the two tracers across all five mice. The pairwise testing was used to establish the influence of dual-tracer imaging, if any.

Results

Dual-Tracer signal separation: Static vs linear models

Synthetic dual-tracer datasets were combined by interleaving the list mode data of each tracer acquired on separate days. The combined datasets were simulated according to the protocol outlined in Figure 4-1 with variable lengths of τ. Figure 4-2 and Figure 4-3 show the fidelity of signal separation using both static and linear separation methods for investigated values of τ. Figure 4-2 shows images of a specific anatomical slice for a selected mouse imaged six-hours post injection of ^{64}Cu-EphA2. It can be qualitatively seen that by increasing τ, ^{64}Cu-EphA2 signal fidelity, signal separation and subsequent extraction of the ^{18}F-FDOPA activity are all improved.

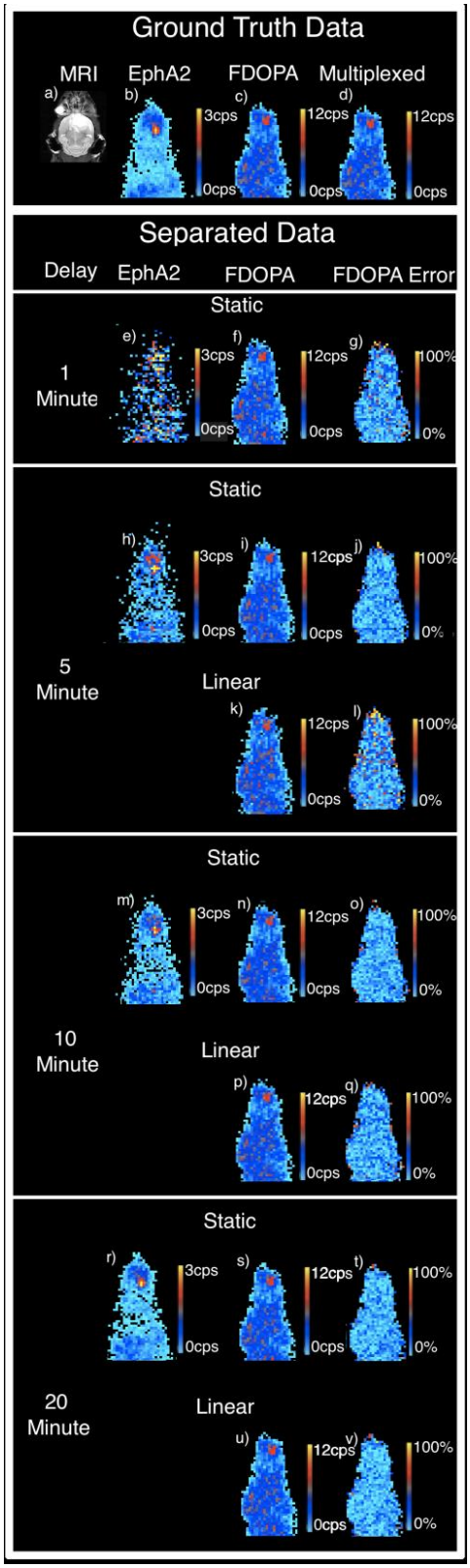

Figure 4-2 – Images of an anatomic slice for one of the synthetically combined mice, imaged six hours post injection of ^{64}Cu-EphA2. The tumour is shown in a T_2 weighted MRI (a) for reference. Independently obtained thirty minute ^{64}Cu-EphA2 (b) and ^{18}F-FDOPA (c) scans were synthetically combined (d) using the list mode data to simulate τ values of 1, 5, 10 and 20 minutes. Reconstruction and decay correction was performed using the original scanner software. Using the ^{64}Cu-EphA2 frame (e,h,m,r), ^{64}Cu-EphA2 activity was subtracted from the dual-tracer frame to recover the ^{18}F-FDOPA activity by means of the static method (f,i,n,s) and the linear method (k,p,u). Error in the estimated ^{18}F-FDOPA activity, expressed as a percentage of the true signal, is shown for both the static method (g,j,o,t) and linear method (l,q,v).

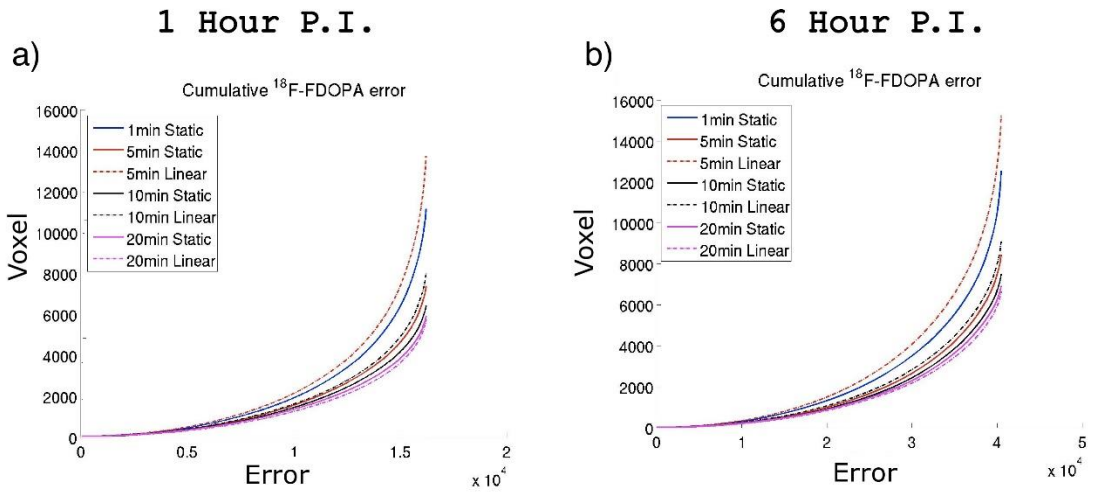

Figure 4-3 – Quantitative results from the three synthetically combined mice imaged at one hour (a) and six hours (b) post injection of ^{64}Cu-EphA2. Figures are cumulative sums of ^{18}F-FDOPA error across the mouse volume and averaged across the three mice. The larger the tail of the curve, the greater the error across the volume. For lower values of τ (1-10 minutes) the original static method outperforms the extended linear method. However for a τ value of 20 minutes, the linear method outperforms the static method.

These results are displayed quantitatively in Figure 4-3 for both one hour and six hours post injection of ^{64}Cu-EphA2, averaged across the three mice. Cumulative distributions of extracted ^{18}F-FDOPA signal error are plotted for increasing τ. Again, it can be seen that by increasing τ, the ability to separate the dual-tracer signals improves. In addition, it can be seen that signal separation improves when the linear method for signal separation is used for long values of τ.

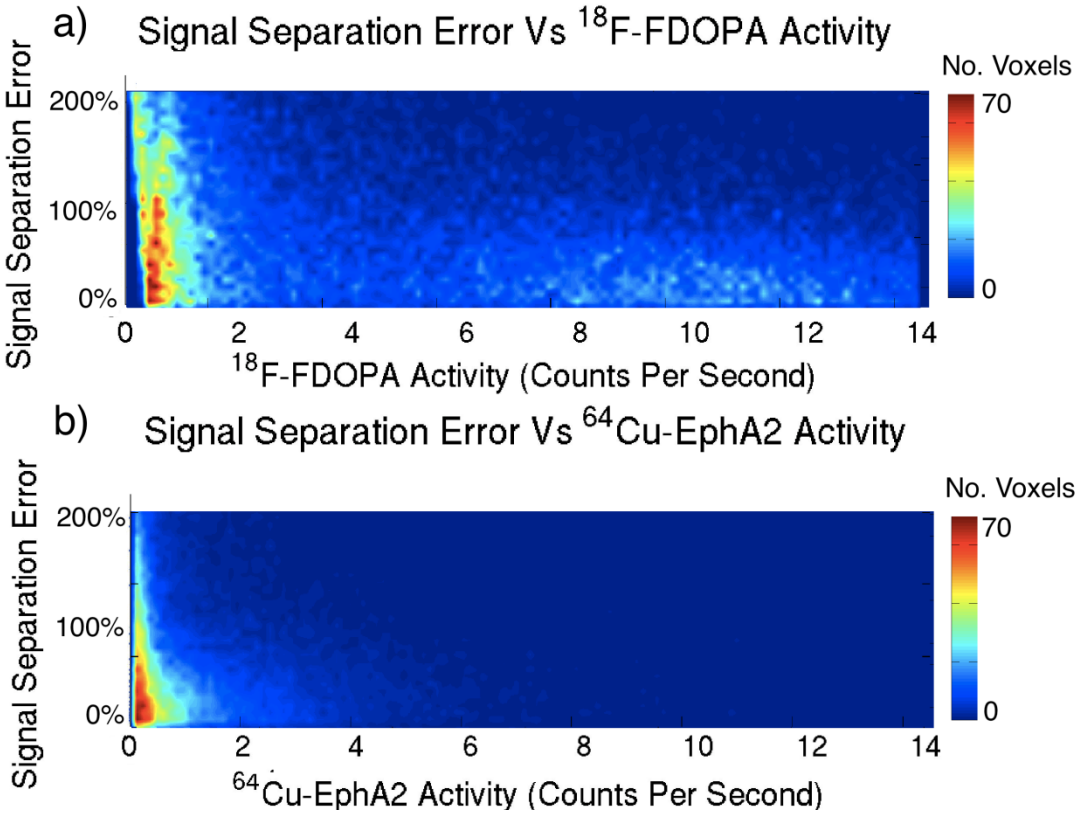

Figure 4-4 – Joint histograms (frequency plots) of (a) error versus ^{18}F-FDOPA and (b) ^{64}Cu-EphA2 activity for the mouse displayed in Figure 4-2, showing the relationship between the amount of activity and the resulting error for ^{18}F-FDOPA. For ^{64}Cu-EphA2 the relationship is less prominent.

Further experiments were performed to investigate which voxels cause the highest errors in signal separation. Figure 4-4a shows the error in ^{18}F-FDOPA versus the ^{18}F-FDOPA activity. It can be seen that areas of high error are likely to occur in voxels where ^{18}F-FDOPA activity is low. In addition, Figure 4-4b shows the error in extracted ^{18}F-FDOPA versus ^{64}Cu-EphA2 activity. While a relationship also appears to exist here, it is less pronounced, suggesting it has less of an effect on fidelity of the extracted signal.

Using Dual-Tracer PET to validate potential nanomedicines

To demonstrate that combining a potential nanomedicine and a validation tool is logistically possible, two real dual-tracer experiments were performed. An anatomical slice of a true dua-tracer mouse is shown in Figure 4-5. Here, the contrast enhanced MRI shows the location of the tumour, with ^{64}Cu-EphA2 and extracted ^{18}F-FDOPA images showing significant uptake in this region.

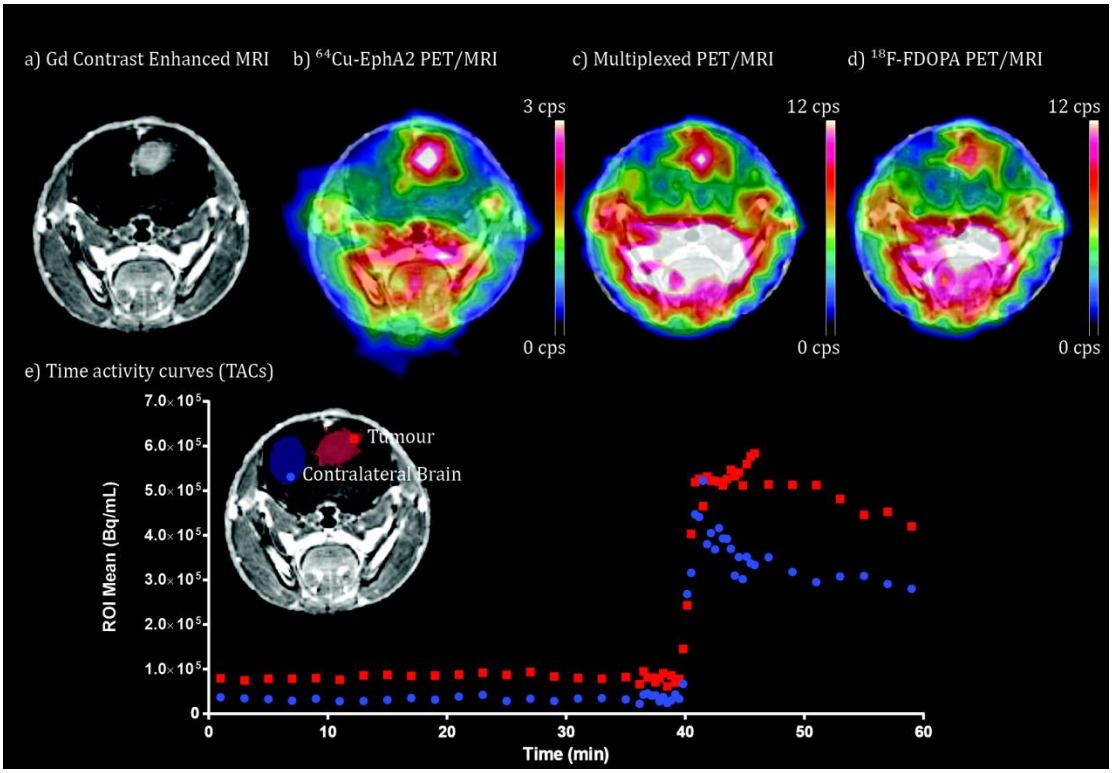

Figure 4-5 – Anatomical slice of the real dual-tracer mouse. The mouse was injected with ^{64}Cu-EphA2 at time zero. After 240 minutes post injection, scanning was initiated. After 280 minutes post injection, the mouse was injected with ^{18}F-FDOPA and scanning continued for an additional 20 minutes. The data was reconstructed using the original scanning software, correcting for ^{64}Cu-EphA2 decay. The activity of ^{64}Cu-EphA2 (b) was subtracted linearly from the dual-tracer frame (c) to extract the ^{18}F-FDOPA activity (d). The tumour is shown in the MRI (a) for reference. ROIs defined on the MRI are shown in (e) with the corresponding mean activities for each ROI. Activities in (e) are ^{64}Cu-EphA2 only for the first 40 minutes (240 – 280 minutes post injection of ^{64}Cu-EphA2) and ^{64}Cu-EphA2 + ^{18}F-FDOPA for the remaining 20 minutes (280 – 300 minutes post injection of ^{64}Cu-EphA2)

Figure 4-6 shows the voxel-wise correlation between ^{64}Cu-EphA2 and ^{18}F-FDOPA for each of the five mice (3 single-tracer and 2 dual-tracer). Tumour and normal tissue Pearson's correlation coefficients, r^2, are shown above each plot. It can be seen that there is a clear correlation between tracer activities in four of the five mice.

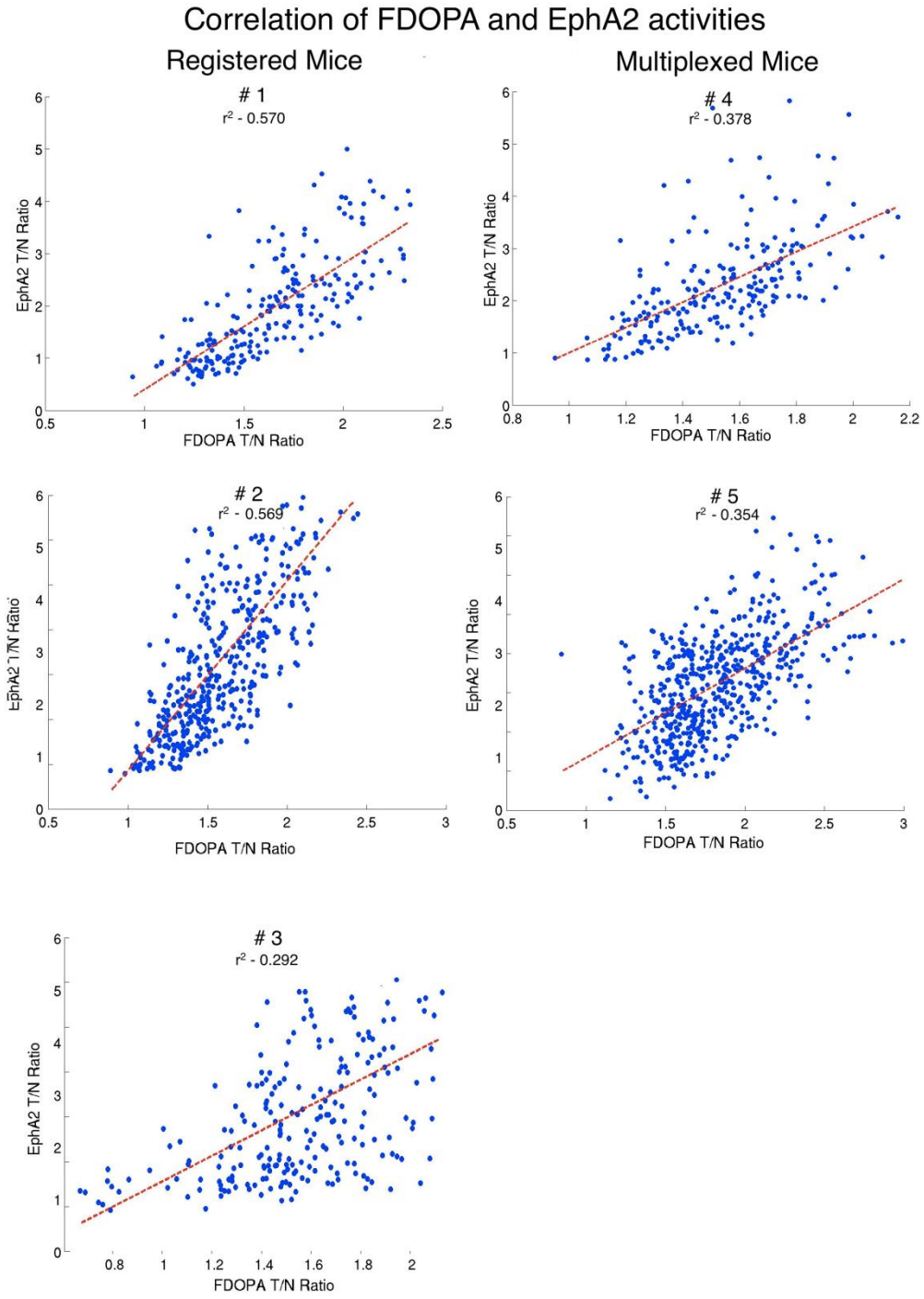

Figure 4-6 – Voxel-wise correlation between ^{18}F-FDOPA and ^{64}Cu-EphA2 uptake in the five mice imaged. The voxel-wise Pearson's correlation coefficient r^2 is shown above each plot.

Statistical validation of the Dual-Tracer method

Table 4-1 shows *p*-values for the pairwise t-test performed for each pair of mice. Mice #1-#3 were single-tracer mice where imaging was performed on separate days. Mice #4 and

#5 were the dual-tracer mice. Low t-statistics with associated high *p*-values indicate the slopes of regression, i.e., the correlation of the tracers are similar between the two mice tested. It can be seen from the table that only one mouse, mouse #3, has a significantly different slope from the others.

Table 4-1 – t-values, standard error and *p*-values for the pairwise t-test performed for each pair of mice. Mice #1-#3 were single-tracer mice where imaging was performed on separate days. Mice #4 and #5 were dual-tracer mice.

Mouse	#1 (Registered)	#2 (Registered)	#3 (Registered)	#4 (Dual-Tracer)	#5 (Dual-Tracer)
Slope	2.41	3.66	2.36	2.41	2.34
Standard Error	0.14	0.16	0.24	0.21	0.11
R2	0.57	0.57	0.29	0.38	0.35
N	220	420	237	217	563
#1 (Registered)		5.88 (p<10-6)	0.18 (p=0.85)	0 (p=1.00)	0.39 (p=0.69)
#2 (Registered)			4.51 (p<10-6)	4.73 (p<10-6)	6.80 (p<10-6)
#3 (Registered)				0.16 (p=0.87)	0.08 (p=0.94)
#4 (Dual-Tracer)					0.30 (p=0.76)
#5 (Dual-Tracer)					

Discussion

The error associated with dual-tracer image acquisition and subsequent image extraction was investigated by synthetically creating dual-tracer datasets from images acquired on two separate days. In this way, single-tracer data can be used to produce measures of signal fidelity and allows experiments to be performed that can be used to pre-validate dual-tracer imaging protocols. Here, the time prior to injection of ^{18}F-FDOPA, τ, and the concentration (activity) of each tracer in an imaging voxel were investigated for their effect on signal fidelity.

In the real-world experiments no ground truth is available. At best, it can be assumed that the signal is the best estimate of PET activity that can be obtained with the hardware, albeit with error bounds that can be established. Hence experiments attempted to estimate bias with respect to the non-multiplexed PET reconstructions (i.e. not the ground-truth) and that the variance in the signal estimates did not increase materially. Also given the manner in

which PET scanners are read, where clinicians identify hyper-intensities within a noisy background sometimes in comparison to contralateral regions, results were usually reported in terms of contrast in units of signal standard deviation (which implicitly accounts for noise).

It can be seen from Figure 4-2 and Figure 4-3 that the scanning time prior to injection of ^{18}F-FDOPA (τ) must be sufficiently long to adequately estimate the ^{64}Cu-EphA2 signal. If τ is too short, linear regression will be excessively erroneous, leading to a poor estimation of the ^{64}Cu-EphA2 signal and a subsequently poor extraction of the ^{18}F-FDOPA activity. In addition, qualitative and quantitative measures calculated from a ^{64}Cu-EphA2 acquisition that is too short will be inaccurate. However, overcompensating will increase the scanning time unnecessarily. It can be seen that as the scanning interval is lengthened from one minute to twenty minutes, the fidelity of both the ^{64}Cu-EphA2 and ^{18}F-FDOPA signals increases. Figure 4-3 provides quantitative results that corroborate this, showing that, as the pre-^{18}F-FDOPA scanning interval is lengthened, the quality of the extracted ^{18}F-FDOPA signal increases. Furthermore, as can be seen in all three figures that the improvement in the signal fidelity between 10 and 20 minutes is not significant, suggesting a scanning interval of 10 minutes may suffice for most cases, and lengthening scan time beyond this is unnecessary.

In addition, it can be seen that the time between injection of ^{64}Cu-EphA2 and commencement of scanning has a model-dependent effect on the fidelity of the extracted signal. For this study, post injection times of one and six hours were chosen for ^{64}Cu-EphA2. For a τ value of 20 minutes, the gain in signal fidelity when using linear regression over the static approach is greater for a post ^{64}Cu-EphA2 injection time of 1 hour compared to 6 hours. This is likely due to the changing uptake dynamics of the antibody into the tumour volume. It has previously been shown that uptake of ^{64}Cu-EphA2 into the tumour reaches a state of equilibrium approximately 6 hours post injection and so it follows that use of a linear model at six hours does not offer significant advantage over a simpler static model. Extending the FDOPA scan or including the period with faster uptake would likely increase the advantage of using a linear model (if τ is sufficient, and the linear assumption holds). The increase in performance of the linear model at shorter times post injection of ^{64}Cu-EphA2 becomes pertinent when considering application of this framework to other, non-antibody based, nanomedicines. Potential nanomedicines based upon peptide systems, small proteins or synthetic polymers may have different pharmacokinetics to a monoclonal antibody and may not exhibit regions of dynamics that can be modelled as

static. As such, the application and validation of a linear model to describe the dynamics of the first tracer and its use in separating dual-tracer PET signals significantly broadens the applicability of this methodology.

Finally, it can be seen (Figure 4-4) that the injected dose of each tracer has an effect on the fidelity of the extracted signal, due to the Poisson noise of PET. If the injected activity is too low, the detected activity will also be low. This will firstly result in a low signal-to-noise ratio, lowering the quality of the acquired images of the first tracer. In addition, it can be seen in Figure 4-4 that low activity also negatively affects the performance of signal separation. Figure 4-4 shows the extracted ^{18}F-FDOPA signal error plotted against both the ^{18}F-FDOPA activity (Figure 4-4a) and the ^{64}Cu-EphA2 activity (Figure 4-4b). If the ^{18}F-FDOPA activity is too low, the error from estimation of the ^{64}Cu-EphA2 signal will be significant in comparison, leading to an erroneous signal extraction (Figure 4-4a). In addition, a low ^{64}Cu-EphA2 signal-to-noise ratio will also negatively affect the signal separation, as it introduces more uncertainty into the regression's output variables (Figure 4-4b). While the ^{64}Cu-EphA2 appears to be less influential on signal separation, a trend is still obvious. Therefore, it appears that increasing the dose of both tracers improves the fidelity of the separated signals. However, the dose of ^{18}F-FDOPA should be larger than the dose of ^{64}Cu-EphA2 to minimize the effect of any error in ^{64}Cu-EphA2 signal estimation.

A potential issue of dual-tracer PET imaging is the logistics of synthesising both radiotracers on the same day. This issue is limited in this work, as the ^{64}Cu isotope, which as a half-life of 12.7 hours, was able to be synthesised offsite and transported the day before imaging. The radiolabelling and characterisation of ^{64}Cu-EphA2 was performed in parallel to the synthesis of ^{18}F-FDOPA so that both radiotracers were available at the time of imaging.

To fully validate the methodology, statistical comparisons were drawn between synthetic dual-tracer datasets and true dual-tracer datasets. A pairwise t-test was performed for each pair of mice, the results of which are shown in Table 4-1. This test identifies which regression slopes were significantly different, i.e., which mice suggested a different relationship between the two tracers. As can be seen, the only mouse that was significantly different from the others was #2, a single-tracer mouse. After reviewing the data, it appears that a possible explanation of this is the injection of ^{64}Cu-EphA2 into the mouse, in particular the cannula itself. There was significant activity surrounding the cannula, suggesting that it was displaced during injection, preventing the tracer from entering the tail vein effectively. This mouse was only included in the final results for completeness. This suggests that

performing dual-tracer PET imaging does not place a significant bias on the results, and that either method should give viable information when comparing the spatial distribution of two tracers.

Finally, this framework could readily be extended to other paradigms, where the residual dynamics cannot be represented by a static or linear model. The uptake dynamics of ^{64}Cu-EphA2 is relatively slow due to the large size of the ^{64}Cu-EphA2 molecule, decreasing the permeability. However, if a potential theranostic with a higher permeability is developed, the uptake dynamics may increase significantly. If this were the case, an exponential model may be more fitting for separating any dual-tracer signals. Here, modification of 4-2 can be performed to include the exponential term desired, extending this framework into an exponential paradigm.

Summary

In this chapter, an extension to the previous technique for pre-validating protocols for dual-tracer imaging was presented. Here, it is assumed that the rate of change of activity for the first tracer was constant at the injection of the second. This technique was evaluated on a set of spatially registered images of a potential nanomedicine and a diagnostic marker of disease progression. Furthermore, this methodology should be applicable to any IgG type structure or nanomedicine of similar pharmacokinetic behaviour. Finally, it was shown that by using more complex models to describe the dynamics of the first tracer, it may be possible to apply this methodology to nanomedicines with more complex pharmacokinetics that do not reach steady state for some time.

Coupled with the methodology presented in chapter 3, a framework is now available for performing dual-tracer imaging when the dynamics of the first tracer is static or linear. However, for a large number of tracers, this is not applicable as the residual dynamics are non-linear. Thus, to fully investigate and provide tools for effective dual-tracer imaging, the case of imaging two tracers with rapid dynamics must be investigated.

Chapter 5 - Performing dual tracer PET imaging in the general case by extending Basis Pursuit

Introduction

Previous work in this thesis is limited to cases where the dynamics of the first tracer are known *a priori* as either static or linear. For many cases, this is not possible. This chapter consists of the paper “Performing dual tracer PET imaging in the general case by extending Basis Pursuit” resubmitted with requested major revisions, and proposes a technique that uses the basis pursuit formulation (128) to consider the general case that represents all biology and PET radio-isotopes, allowing for pre-validation of scanning protocols irrelevant of the tracer combination used. Basis pursuit allows model complexity to be defined by the data and its formulation can be naturally extended to separating pairs of dynamic signals with an injection interval, T. The approach is applied by optimising the injection delay and relative injected activity for the general case where residual dynamics from a first tracer exist during injection of a second. Validation of the approach is performed by examining the statistics of the residual and parameters of the fitted curves within tissues.

Materials & Methods

The Basis Pursuit Technique

The temporal evolution of a tracer within the body can be modelled using time activity curves (TACs), which can be used to extract kinetic parameters. Kinetic analysis is often formulated as a numerical solution of a set of ordinary differential equations, yielding a set of kinetic parameters. Non-linear regression is typically used for this purpose, however this requires the prior selection of a compartment model. As described by Gunn *et al*. (128), an alternative representation is to describe the tissue as a linear combination of input response functions, shown in 5-1**.**

$$C(t) = V_b C_b + (1 - V_b) \sum_{i=1}^{n} \phi_i e^{-\theta_i t} \otimes C_p(t) \qquad 5\text{-}1$$

where C is the activity concentration within the tissue at time t. V_b and C_b are the blood volume fraction and blood activity concentration, respectively. ⊗ is the convolution operator, φ and Θ are the weight and rate of decay defining each of the n terms. The

number of terms, n, can be left unfixed, removing the requirement for a prior selection of the model. Extending 5-1 to the dual-tracer case:

$$C(t) = C_\alpha(t) + C_\beta(t+T) \qquad 5\text{-}2$$

$$= V_{b\alpha}C_{b\alpha} + (1-V_{b\alpha})\sum_{i=1}^{n_\alpha}\phi_i e^{-\theta_i t} \otimes C_{p\alpha}(t) \; + \; V_{b\beta}C_{b\beta} + \left(1-V_{b\beta}\right)\sum_{i=1}^{n_\beta}\phi_i e^{-\theta_i (t+T)} \otimes C_{p\beta}(t-T)$$

where the subscript α is used for the first tracer, and β for the second. The injection interval between the tracers is explicitly symbolised by T. A solution to 5-2 can be found for a sample tissue using a dictionary for each tracer. The dictionary, Ψ, is a matrix of kinetic basis functions, each of which is calculated as:

$$\psi_i(t) = \int_0^t e^{-\theta_i(t-\tau)} C_p(\tau) d\tau$$

$$\psi_0(t) = C_p(t) \qquad 5\text{-}3$$

where θ_i is varied over a physiologically plausible range. C_p is the plasma input function that represents the concentration time course of the tracer in the plasma, determined prior to the generation of the dictionary. The first basis function ψ_0 is set to C_p to allow estimation of the arterial activity in the sample tissue.

Basis functions are widely used for model fitting because they allow the linear and non-linear parameters in model to be solved independently, accelerating optimisation and improving robustness, e.g. the BAFPIC (Basis Functions from Plasma Input Compartments) approach proposed by Hong *et al.* (16), with extensions to ensure distinguishability of the two compartments by Kadrmas *et al.* (17) and formulations tailored to the GPU (18). However, basis pursuit adds the use of L1-regularisation (described in the next section) during optimisation to enforce sparsity which allows the choice in the structure of the compartment model to be dictated by the data on a per-voxel basis. This provides an important advantage for separating signals in dual tracer images containing multiple tissue types with uptake patterns that are likely heterogeneous and when it is not yet clear whether a particular tracer (with lower uptake) is even distinguishable.

The resulting dictionary for each tracer can be described using 5-4

$$\boldsymbol{\psi_\alpha} = \begin{bmatrix} \psi_{\alpha 01} & \cdots & \psi_{\alpha N_\alpha 1} \\ \vdots & \ddots & \vdots \\ \psi_{\alpha 0F} & \cdots & \psi_{\alpha N_\alpha F} \end{bmatrix}, \boldsymbol{\psi_\beta} = \begin{bmatrix} \psi_{\beta 01} & \cdots & \psi_{\beta N_\beta 1} \\ \vdots & \ddots & \vdots \\ \psi_{\beta 0F} & \cdots & \psi_{\beta N_\beta F} \end{bmatrix}, \qquad 5\text{-}4$$

where N is the number of dictionary elements and F is the number of image frames. For this study, a value of 30 was chosen for N, as at this resolution linear interpolation has been shown to provide a good approximation of parameters while being computationally efficient (128). The two dictionaries are concatenated with the second dictionary's values prior to its injection time set to zero

$$\boldsymbol{\psi} = \begin{bmatrix} \psi_{\alpha 01} & \cdots & \psi_{\alpha N_\alpha 1} & \psi_{\beta 01} & \cdots & \psi_{\beta N_\beta 1} \\ \vdots & \ddots & \vdots & \vdots & \ddots & \vdots \\ \psi_{\alpha 0F} & \cdots & \psi_{\alpha N_\alpha F} & \psi_{\beta 0F} & \cdots & \psi_{\beta N_\beta F} \end{bmatrix} \qquad 5\text{-}5$$

An example dictionary set is shown in Figure 5-1. A sparse linear combination of the dictionary elements can be computed to describe the data using the Basis pursuit as originally proposed in (128). Sparse in this case implies most of the coefficients associated with dictionary elements, $\mathbf{y} = [y_1 \ldots y_F]^T$, are zero.

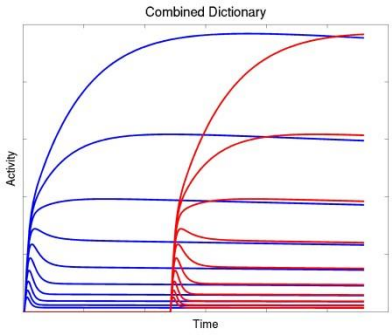

Figure 5-1 Example of a dictionary for two tracers with a given injection delay. The first tracer is shown in blue and the second in red. The final dictionary is a linear combination of the two.

Sparsity is achieved by utilisation of L_1 regularisation, modulated by the regularisation parameter, μ, within a quadratic programing framework to enforce positivity in the coefficients, **ϕ:**

$$\min_{\phi} \frac{1}{2} \left\| \mathbf{W}^{\frac{1}{2}} (\mathbf{y} - \boldsymbol{\Psi}\boldsymbol{\phi}) \right\|_2^2 + \mu \|\boldsymbol{\phi}\|_1 \qquad 5\text{-}6$$

The regularisation parameter μ is set globally for the image volume using leave one out cross-validation (LOOCV) as per (128). Typically μ is scalar, but to impose prior knowledge about the expected relative activities of the two tracers a vector can be used; for example, to account for a large relative difference in injected activities. In the following experiments, the standard scalar definition of μ is used. Once Basis Pursuit is performed, the identity of the dictionary elements with non-zero elements allows the individual tracers to be separated. From the calculated coefficients, key macroscopic parameters can be calculated. For this study, two parameters were investigated, based on the tracer reversibility of the tissue being investigated:

Volume of distribution (V_T), the ratio of the tracer concentration in tissue target to that in plasma at equilibrium, calculated as $\sum \frac{\phi_i}{\theta_i}$ (129). V_T is appropriate for reversible kinetics, where the tracer is both taken up and excreted by the tissue.

Irreversible uptake rate (K_I), the rate of tracer that is irreversibly bound in the tissue, calculated as ϕ_n (129). K_I is appropriate for irreversible kinetics, where the tracer is taken up but not excreted by the target tissue.

It's important to note that the choice of V_T and K_I is irrelevant with regards to the methodology, as the algorithm performs in the general case and can be implemented regardless of the reversibility of the tracers chosen. In the following experiments available ^{18}F-FDOPA and ^{18}F-FDG data were utilised.

Quantifying Error

In the single tracer case, the error in fit can be attributed to the random noise in the system, ε_{Noise}, controlled by the injected tracer activity and the geometry of the scanner such that:

$$C_{Noisy}(t) = C(t) + \varepsilon_{Noise} \qquad 5\text{-}7$$

The signal noise also acts to induce the standard deviation in any estimates in derived parameters, $\sigma_{noise}^{(p,i)}$, for either tracer, where *p* indicates the parameter of interest and *i* the tracer. When performing dual-tracer imaging, the additive noise will act to increase the

standard deviation by a certain amount, $\sigma_{multiplex}^{(p,i)}$, as may the linear dependence of the two tracer profiles if activity from one tracer is incorrectly attributed to the other. The latter can also act to induce a bias in the estimate, $\varepsilon_{multiplex}^{(p,i)}$.

In the ideal dual tracer case, $\sigma_{multiplex}^{(p,i)}$ and $\varepsilon_{multiplex}^{(p,i)}$ approach zero, but in practice there will be some finite fraction of $\sigma_{noise}^{(p,i)}$, which the designed protocol will aim to minimise.

Investigating the feasibility of imaging protocols

Given this formulation, it is therefore possible to estimate the amount of error expected when performing dual-tracer imaging under certain scanning protocols using a simulation based approach (Figure 5-2). This approach is performed in two steps: Generation of single-tracer data (Figure 5-2.1) and a feasibility study of dual-tracer protocols (Figure 5-2.2).

Using available single-tracer scans (Figure 5-2.1a) pharmacokinetic fits can be performed, extracting kinetic parameters for specific tissues of interest (Figure 5-2.1b). Single and Dual-Tracer pharmacokinetic time activity curves can then be synthetically generated (Figure 5-2.2a). 1000 instances of randomly generated noise are added to each simulation as per 3-6 and combined to generate synthetically combined dual-tracer curves (Figure 5-2.2b). Single- and dual-tracer simulations are then processed using the basis pursuit method to extract pharmacokinetic parameters (Figure 5-2.2c). The fitted parameters are compared to examine the increase in variance due to dual-tracer imaging (Figure 5-2.2d).

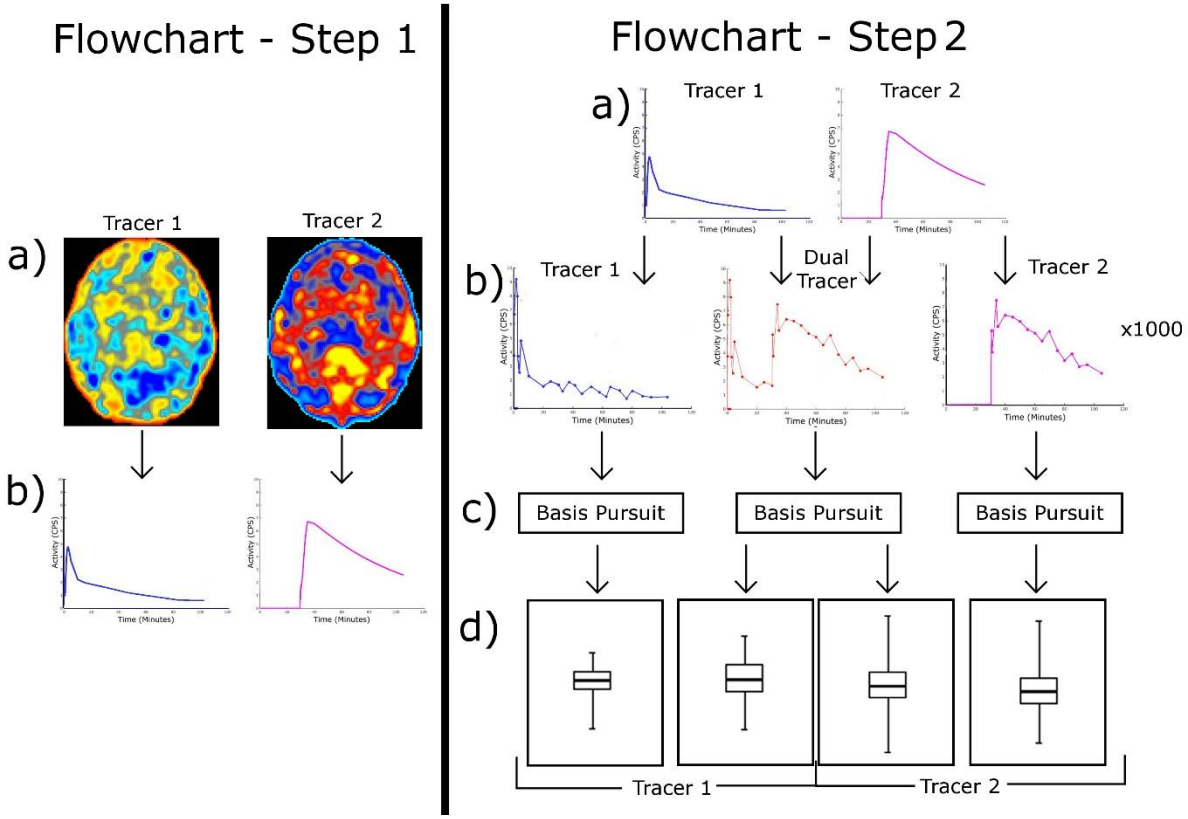

Figure 5-2 Flowchart for feasibility study of dual-tracer imaging protocols. It is convenient to consider the approach in two steps: Generation of single-tracer data (Step 1) and feasibility study of dual-tracer protocols (Step 2). First, a single-tracer imaging sessions must be performed if single-tracer data is not currently available for each tracer (a). From this, kinetic analysis is performed to determine the pharmacokinetic parameters associated with the tissues to be investigated (b). The second step allows a feasibility study of dual-tracer imaging protocols. First, single-tracer pharmacokinetic curves are generated using known kinetic parameters, generated from single tracer images acquired previously (a). These curves are then sampled 1000 times for noise as per 3-6 and combined to generate synthetically combined dual-tracer curves (b). Single- and dual-tracer simulations are then processed using the basis pursuit method to extract pharmacokinetic parameters (c). Single- and dual-tracer parameters can then be compared to assess if the scanning protocol is acceptable (d).

Physical phantom experiment

To demonstrate the principle of dual-tracer imaging, an experiment was performed to evaluate the separation process with real data while still retaining the original single-tracer signals. In the real-world experiments no ground truth is available. At best, it can be assumed that the signal is the best estimate of PET activity that can be obtained with the hardware, albeit with error bounds that can be established. Hence experiments attempted to estimate bias *with respect to the non-dual-trracer PET reconstructions* (i.e. not the ground-truth) and that the variance in the signal estimates did not increase materially. Also given the manner in which PET scanners are read, where clinicians identify hyper-intensities within a noisy background sometimes in comparison to contralateral regions,

results were usually reported in terms of contrast in units of signal standard deviation (which implicitly accounts for noise). To accomplish this, a physical phantom experiment using four Slide-A-Lyzer dialysis cassettes (https://www.thermofisher.com/) in conjunction with a sealed partitioned container was used. The dialysis cassettes were used to mimic uptake of the tracer from the blood into the cells (Figure 5-3a). Here, each partition represented a cell and each cassette represented the plasma. Two cassettes had a 3.5K molecular weight cut off (Tracer 1) and the other two had a 7K molecular weight cut off (Tracer 2). The lower the cut off, the lower the permeability and therefore the slower the dynamics. As per Figure 5-3a, a cassette was placed in each of partition one and two to represent single tracer injections. These compartments acted as the control for the experiment. In the third partition, one of each of the cassettes were inserted to represent dual-tracer imaging. Each cassette was prefilled with 1.5mL of distilled water. The scanning apparatus was placed into a Siemens Inveon pre-clinical PET/CT Scanner and scanning was initiated. The two "tracer 1" cassettes were immediately injected with ^{18}F-FDG, with the remaining two cassettes injected after 20 minutes to represent a 20 minute injection delay (Figure 5-3b). All cassettes were injected with 0.5mL of ^{18}F-FDG tracer. The specific injected activities for each cassette are shown in Table 5-1, with activities from each container normalised for differing injection doses.

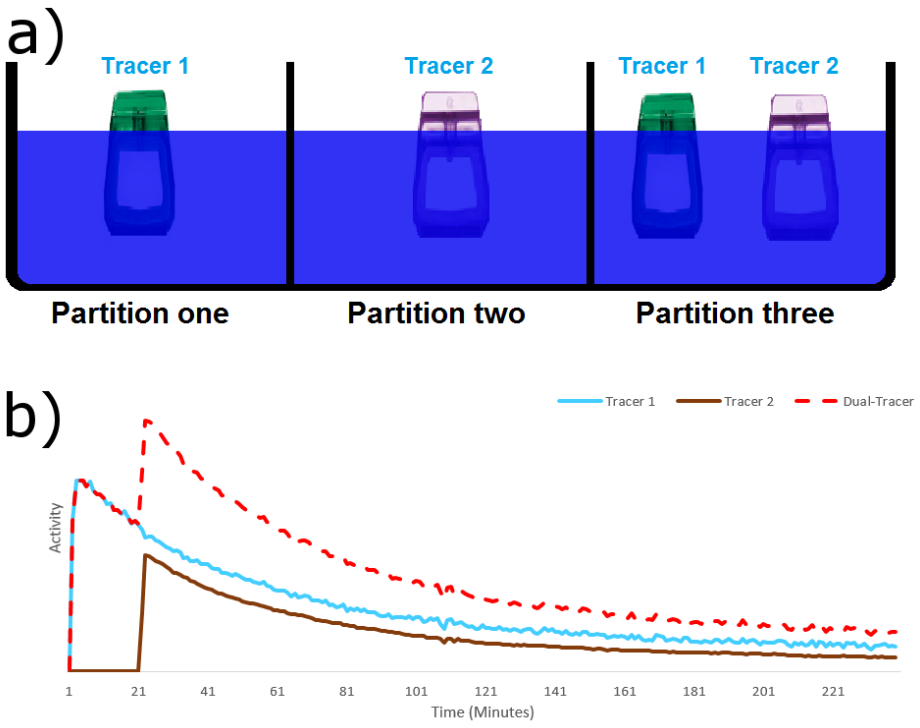

Figure 5-3 Experimental set up of the phantom study. A container was segmented into three separate and isolated partitions and filled with water (a). Cassettes were placed in each partition – one in each of partition one and two to

represent single-tracer activities and two in partition three to represent dual-tracer. Cassettes for tracer one were injected at zero minutes and cassettes for tracer two were injected at 20 minutes (b).

Table 5-1 Injected doses for each of the four cassettes used in the phantom experiment.

Cassette	**Injected Dose**
Single Tracer 1	2.16Mbq
Single Tracer 2	2.18Mbq
Dual Tracer 1	2.22Mbq
Dual Tracer 2	2.08Mbq

Segmentations of the bag (acting as the “plasma” compartment in a one compartment model) and the remainder of the partition (acting as an extra-vascular space) were obtained from the CT. The entire volume within each partition consisting of the bag and the remainder of the partition substitutes as a single voxel within an image.

The time course of concentration within the bags decays more slowly than is typical of blood activity concentrations in PET images, but increases the linear dependence of the blood activity concentration and the summed TAC. Hence in this aspect the experiment is conservative, as it increases the linear dependence of the two signals as well.

To validate the proposed dual-tracer approach, single-tracer compartments were fitted using the basis pursuit method (Figure 5-2.1). Simulations were then performed to simulate and test the feasibility of the dual-tracer protocol used (Figure 5-2.2). Dual-tracer activity was separated to obtain the single-tracer kinetic parameters and the normalised activities and parameters for each were compared to validate both the experiment and the separation method.

Experiment using synthetic combination of real data to simulate dual-tracer imaging

A further demonstration of the process outlined in Fig. 2 was made using a test-retest experiment with (real) images of a NOD/SCID mouse bearing a patient derived (WK1 cell line) glioma cranial xenograph in the right striatum(116). All animal experiments were approved by The University of Queensland Animal Ethics Committee and conformed to the

guidelines of the Australian Code of Practice for the Care and Use of Animals for Scientific Purposes.

A 30 minute ^{18}F-FDOPA dynamic image was acquired with an injected dose of 4.84 MBq (Figure 5-2.1a). From this data, basis pursuit was performed to extract the pharmacokinetic time activity curves and kinetic parameters for each tissue voxel (Figure 5-2.1b, Figure 5-2.2a). Simulations were performed to generate 1000 noisy single- and dual-tracer time activity curves for each voxel (Figure 5-2.2b). Finally, basis pursuit was once again used to obtain kinetic parameters from both single- and dual-tracer curves (Figure 5-2.2c) with kinetic parameters compared (Figure 5-2.2b) for various injection delays.

To remain as realistic as possible in the experiment, the original single-tracer image was interleaved with itself in list-mode form to create a synthetic dual-tracer experiment where the mouse was injected with the same tracer twice, with injection intervals set to the same as above. The purpose of interleaving the list-mode data was to eliminate the potential positive bias (if any) of combining the post-reconstruction data, and to remove the limitation from chapter three where biological information could not be obtained. Furthermore, in a perfect situation, kinetic information obtained for both injections should be identical, allowing visual inspection on the effect of tracer ordering on the results. This “list-mode” dual-tracer image was separated using the basis pursuit approach, with the variance in V_T calculated and compared to the above to ensure the process set out in Figure 5-2 is effective.

True dual-tracer imaging experiment

Finally, the basis pursuit method for separating dual-tracer signals was demonstrated using a single dual-tracer mouse injected with^{18}F-FDG and ^{18}F-FDOPA. This was a proof of concept experiment performed on a NOD/SCID mouse bearing a patient derived (WK1) glioma cranial xenograph in the right striatum. A sixty minute acquisition was performed where the mouse was injected with 2.75 MBq of ^{18}F-FDG at t=0. Using the feasibility from the previous experiment, a delay of 20 minutes was selected, after which 1.73 MBq of ^{18}F-FDOPA was injected and scanning continued for another 40 minutes. The reconstructed dataset was separated using the proposed basis pursuit method to extract the macroscopic parameters V_T for ^{18}F-FDOPA and K_I for ^{18}F-FDG, with recovered parameters compared to acquired single-tracer data (used in previous experiment) and the literature (130, 131) for manually delineated ROIs of brain tumour and cortical tissue. While only a single mouse

was imaged, the large number of intra-subject voxels allows voxel-wise investigations to be performed.

Results

Physical phantom experiment

In a typical image with vascular regions within the field of view that is distinct from the tissue being investigated, a blood activity concentration can be extracted. In this experiment the segmented bags were used for this purpose.

Initially the “blood activity concentration” of each bag type were compared to ensure approximately equal blood activity concentration for subsequent validation. From Figure 5-4, it is clear that the diffusion rates for each of the two tracers is very similar, suggesting that the experimental process was successful, with equal tracer concentrations delivered to the cell compartments for each tracer.

Next fits were performed to simulate fitting entire TACs (for which the sum of compartments is visible). Figure 5-5 shows the single-tracer (maroon & orange) and dual-tracer (red) activities for the delineated cell compartments. From this data, single-tracer (green & blue) and dual-tracer (cyan & brown) fits were performed. From the figure, it can be seen that the single-tracer and separated dual-tracer fits are in agreement, suggesting that the single-tracer activities can be recovered from dual-tracer imaging.

Figure 5-4 and Figure 5-5 show that a comparison between the single-tracer and dual-tracer compartments is possible, allowing a controlled analysis to be performed on the data. Figure 5-6 shows a comparison between the variance in K_I calculated via simulations of TACs generated from single-tracer compartments (box plots; Figure 5-2.2b) and the K_I calculated from the dual-tracer compartment (asterisks). Results show that K_I as calculated from dual-tracer compartments lies within the range of values of K_I calculated from simulations generated from single-tracer compartments (Figure 5-2.2d).

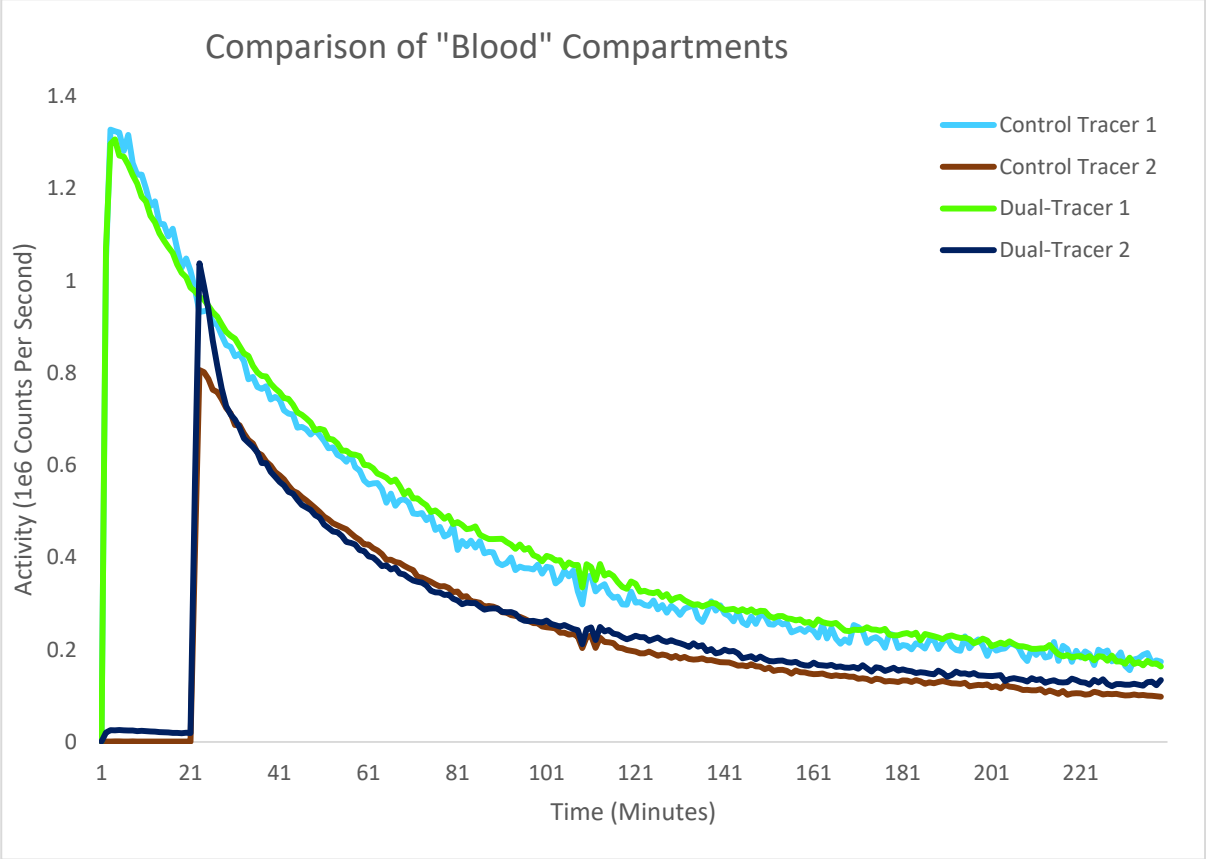

Figure 5-4 Diffusion of ^{18}F-FDG from the blood compartment into the cell compartment. Here it can be seen that the diffusion rates for each of the two tracers (control & dual) is very similar, suggesting that the experimental process was successful, with equal tracer concentrations delivered to the cell compartments for each tracer.

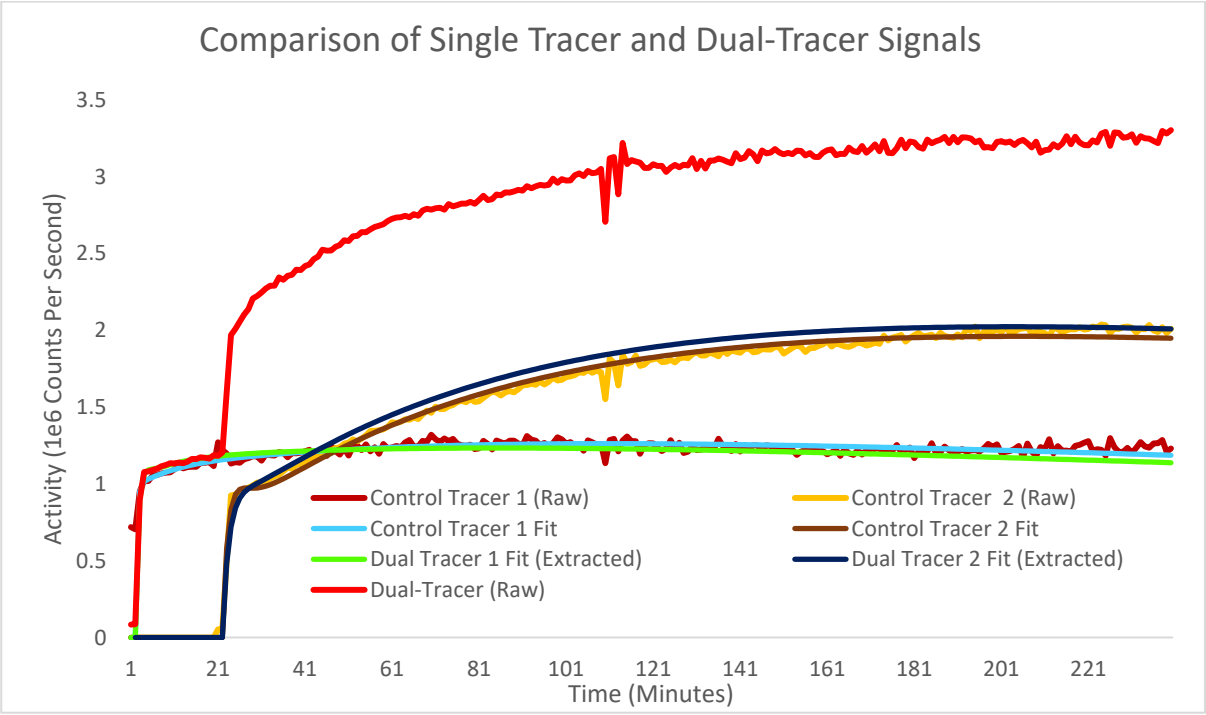

Figure 5-5 Activities and kinetic fits for each of the cell compartments. Single-tracer (maroon & orange) and dual-tracer (red) activities are shown as measured by the scanner. From this data, single-tracer (green & blue) and dual-tracer (cyan

& brown) fits were performed. Here, it can be seen that the single-tracer and separated dual-tracer fits are in agreement, suggesting that the single-tracer activities can be recovered from dual-tracer imaging.

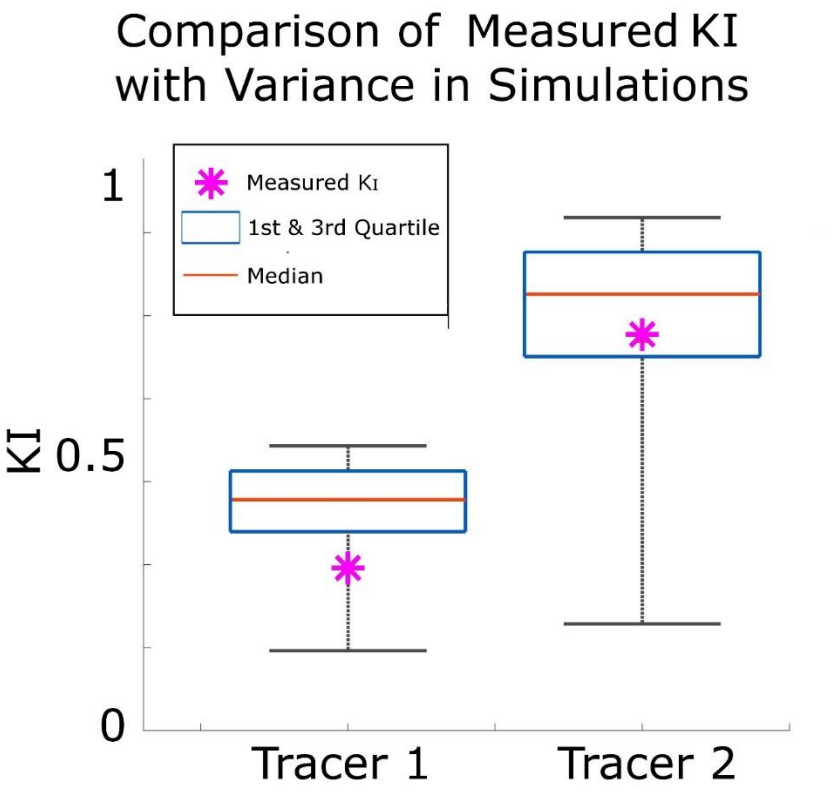

Figure 5-6 Comparison of K_I as measured from the dual-tracer compartment (star) with the variance of K_I as calculated from the single-tracer simulations.

Synthetically combination of real data to simulate dual-tracer imaging

Two investigations were performed using pre-clinical data and the macroscopic parameter V_T for two purposes. Firstly the experiment was used to evaluate the ability to predict the variance encountered when performing dual-tracer imaging on real data using the methodology set out in Figure 5-2. Secondly the experiment was used to evaluate the increase in bias and variance in V_T when performing dual-tracer imaging over single-tracer imaging and as a function of injection delay.

Figure 5-7 shows how the amount of bias introduced to V_T when performing dual tracer imaging over single tracer can be predicted for increasing delay. Plots are shown in groups of four for each injection delay investigated, with plots shown in red reflecting tumour tissue and plots in green depicting normal tissue. The left plot for each colour is from simulated data, used to predict the bias in the real data (shown as the right plot for each colour). The distribution of V_T calculated from real data closely resembles the simulations, indicating that simulations are able to predict the amount of bias introduced when performing dual-tracer imaging.

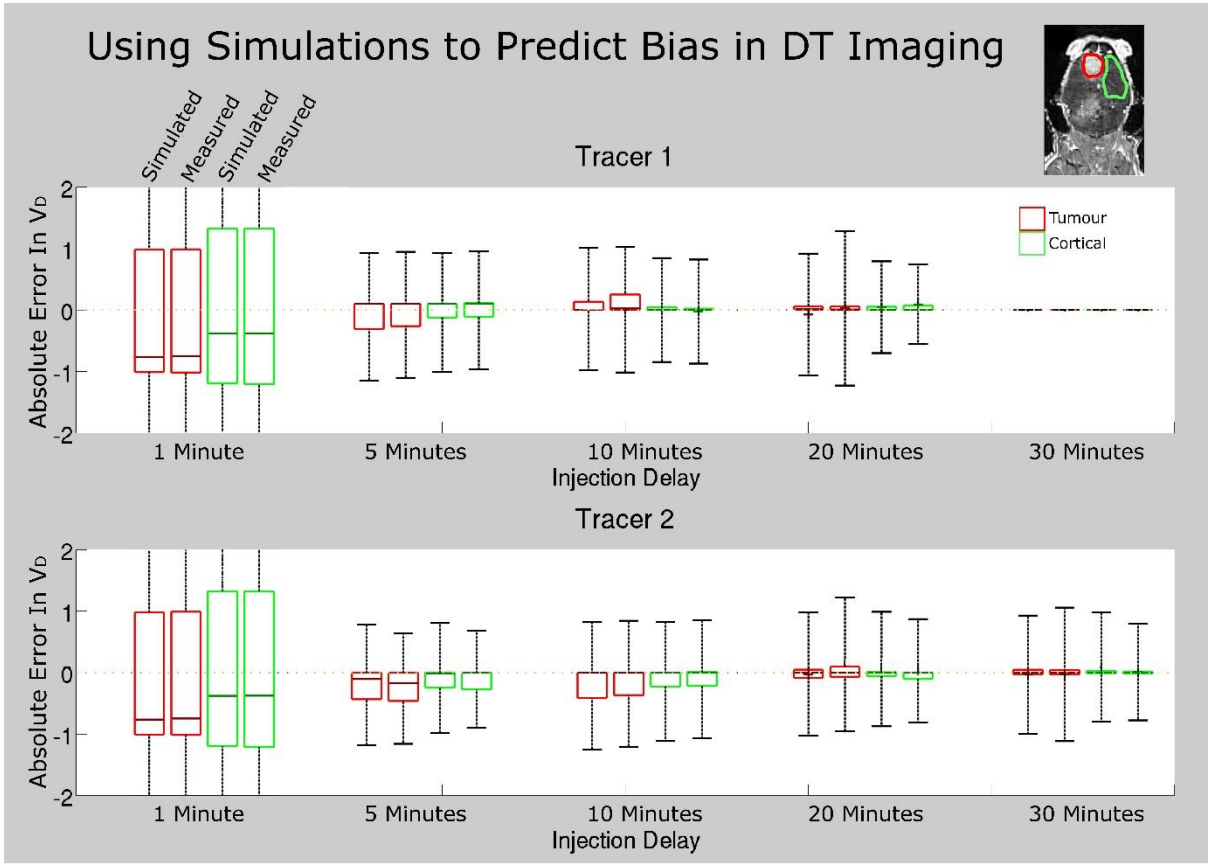

Figure 5-7 Estimating the bias encountered when performing dual-tracer imaging. Plots in red represent tumour tissue and plots in green represent normal tissue. Plots are shown in groups of four for each of the potential injection delays being investigated. The left plot for each colour represents bias calculated from simulations and the right plot reflects real data. It can be seen that bias determined from simulations closely resembles bias calculated from real pre-clinical data.

By selection of the appropriate injection delay the error can be minimised as far as necessary within the bounds imposed by logistics. In all experiments, the error is non-zero and both bias and the increase in parameter variance must be mitigated against the logistics of the scanning protocol. Figure 5-8 shows the distribution of estimated V_T values for both normal (green) and tumour (red) tissue and compares this to the estimates obtained from the single-tracer V_T (within blue box) over the ROI for the same volumes in the single-tracer case. Both Figure 5-7 and Figure 5-8 show that with an injection delay of 20 minutes the additional bias and variance induced by dual-tracer imaging become difficult to discern, especially for Tracer 1.

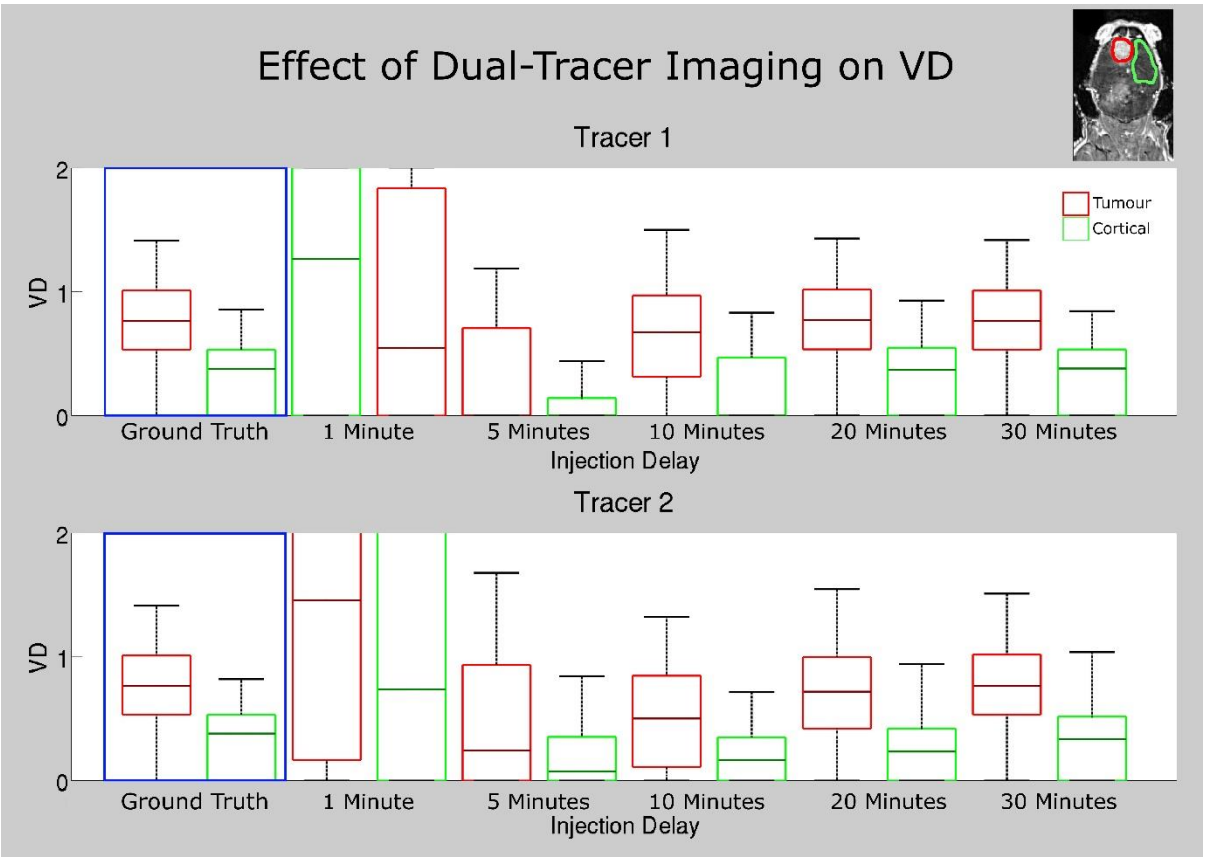

Figure 5-8 Explicitly showing the bias in V_T when performing dual-tracer imaging. Plots in red represent tumour tissue and plots in green represent normal tissue. Plots in the blue box represent single-tracer V_T distributions calculated from real single-tracer data. The remaining plots represent V_T calculated from dual-tracer simulations. It can be seen that for injection delays of 20 and 30 minutes, the distribution of V_T for both tumour and normal tissue very closely reflect the distributions for single-tracer imaging for both tracers, with errors slightly higher for the second tracer.

Real dual-tracer experiments

Figure 5-9 and Figure 5-10 show the results of the actual dual-tracer experiment, where a dynamic ^{18}F-FDOPA image followed immediately by a dynamic ^{18}F-FDG image was acquired in a NOD/SCID mouse bearing a patient derived (WK1) xenograft in the right striatum. Here, an injection delay of 20 minutes was selected, as this appeared to be a conservative choice based on results from simulations above. Figure 5-9 shows a coronal slice of the mouse illustrating the uptake of the tracers and the calculated macroscopic parameters V_T and K_I. A corresponding contrast enhanced MRI is shown in a) for anatomic reference. ^{18}F-FDOPA and ^{18}F-FDG uptake is shown in b) and e) respectively, with the dual-tracer volume shown in d). The tumour is clearly identifiable, as is the excess cortical uptake of FDG, common to this tracer. The calculated kinetic parameter for each tracer is shown in c) and f). It can be seen that the values are higher in tumour tissue for both tracers. It is also higher in the cortical ^{18}F-FDG tissue than ^{18}F-FDOPA, most likely due to the higher cortical uptake of ^{18}F-FDG, which can be seen in c).

For comparison, kinetic parameters for the tumour and cortical tissue were obtained from real single-tracer data (for 18F-FDOPA; previous experimental data) and the literature (130, 131) (for ^{18}F-FDG) were obtained and used for comparison against the real dual-tracer data. Figure 5-10 shows a comparison of the calculated volume of distributions for both brain tumour and normal cortical tissue. The distribution of values for both tissues are comparable and are within one standard deviation of the mean predicted by the simulations.

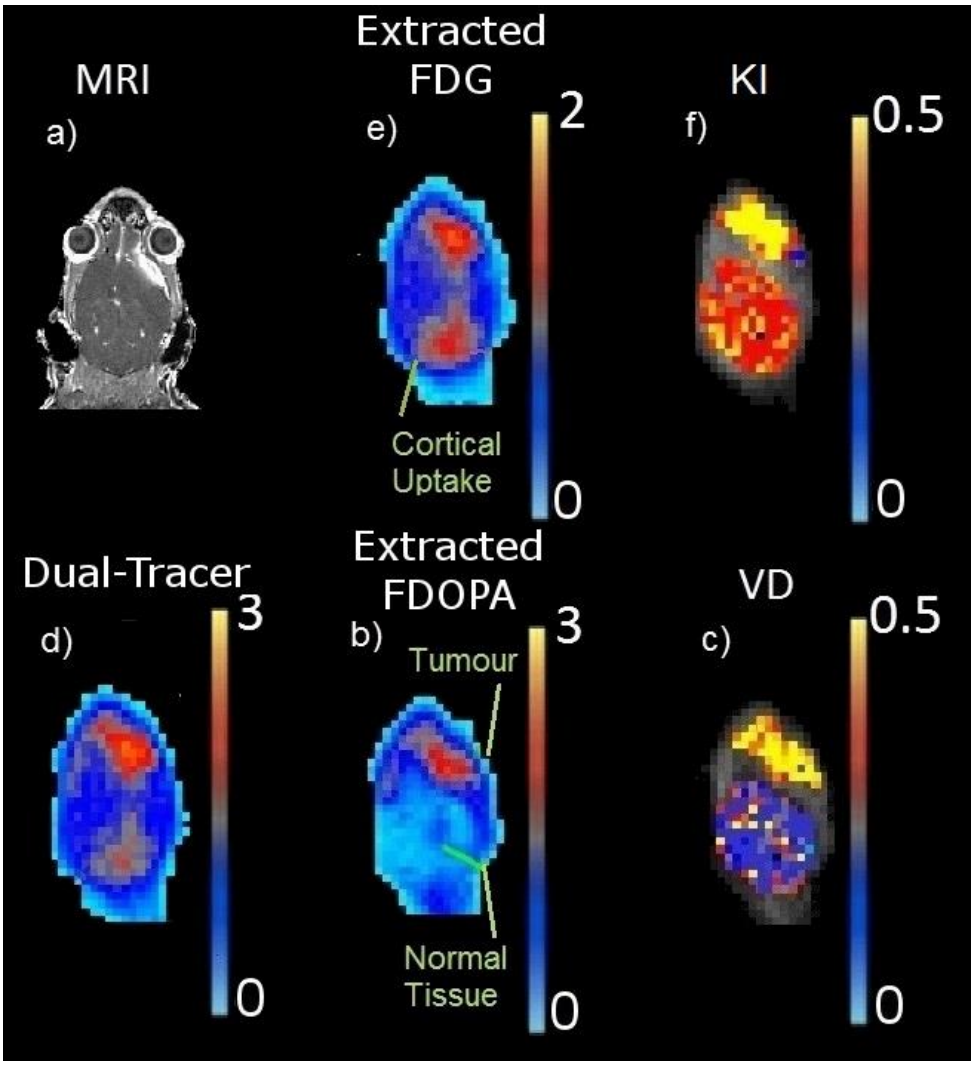

Figure 5-9 Uptake of ^{18}F-FDOPA and ^{18}F-FDG for tumour and normal tissue as measured using a truly combined NOD/SCID mouse data set. 2.75MBq of ^{18}F-FDOPA was injected and 1.73MBq of ^{18}F-FDG was injected. The MRI is shown in a) for anatomic reference. ^{18}F-FDOPA and ^{18}F-FDG uptake is shown in b) and e) respectively, with the dual-tracer volume shown in d). The tumour is clearly identifiable, as is the excess cortical uptake of ^{18}F-FDG, common to this tracer. The calculated kinetic parameters for each tracer is shown in c) and f). It can be seen that these values are higher in tumour for both tracers. It is also higher in the cortical ^{18}F-FDG tissue than ^{18}F-FDOPA, most likely due to the higher cortical uptake of ^{18}F-FDG, which can be seen in c).

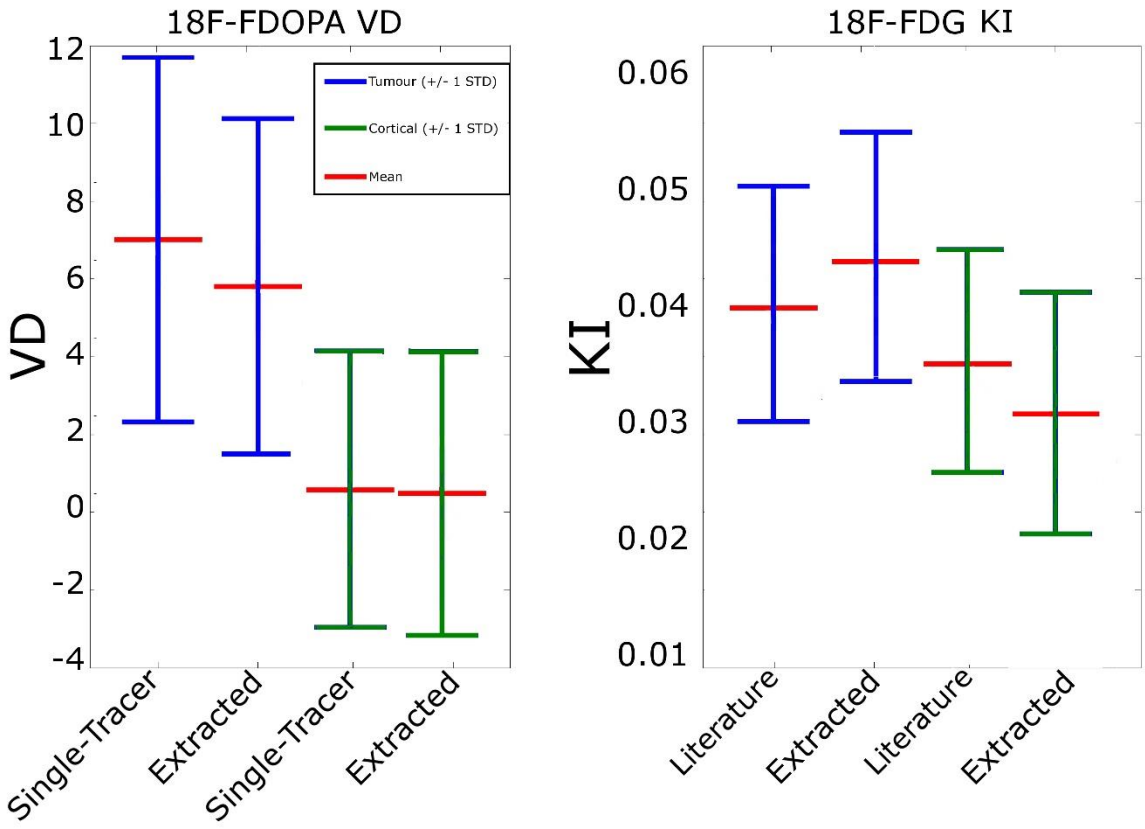

Figure 5-10 Extracted dual-tracer V_T and K_I values for ^{18}F-FDOPA and ^{18}F-FDG compared to single-tracer (^{18}F-FDOPA data from last experiment) and literature for ^{18}F-FDG (130, 131). This shows values obtained while performing dual-tracer imaging are comparable to those found in the single-tracer scans and the literature, suggesting that dual-tracer imaging allows for recovery of important pharmacokinetic parameters.

Discussion

Positron emission tomography (PET) is increasingly used both pre-clinically and clinically due to its ability to provide detailed information on a single aspect of biological metabolism. However, individual counts from different tracers cannot be distinguished by PET scanners, and modelling is required to separate the individual signals when multiple PET tracers are used simultaneously. The alternative of performing individual scans on separate days may be impractical due to limitations on scanner and patient time, changes in tissue morphology and biology between scans and the reliance on successful image registration in deformable tissues.

Several methods have been proposed to separate the signals from combined PET tracers, but all have drawbacks. Some approaches have required the fitting of pre-defined pharmacokinetic models to the combined data which limits their application to specific

biological cases. Other algorithms are used during image reconstruction, requiring data to be available in list-mode form and increasing the computational cost of the already expensive reconstruction methods. Algorithms eschewing kinetic models require the dynamics of the first tracer to have reached stability prior to injection of the second tracer, limiting the selection of tracers and injection intervals. This work proposed using the basis pursuit approach of (128), because it:

- removes the need for a kinetic model to be provided *a priori,* allowing the data to determine the complexity of the tissue being analysed;
- extends naturally to additional tracers that are simultaneously acquired;
- is computationally efficient;
- provides a global optimum;
- can be performed post-reconstruction, i.e. without modification of the reconstruction algorithm; and
- does not require a pre-defined model.

This paper demonstrates the use of basis pursuit to separate tracers without the need to specify a model which allows much flexibility in the choice of radiotracer and which tissue is investigated. This provides a potentially more straight-forward way to separate signals both to test the feasibility of possible scanning protocols and subsequently in the actual study, and it must be stressed that although the method allows multiple potential protocols to be investigated, the study designer must decide if the selected protocol is viable. This study further demonstrates how simulations can be used to predict parameter error for a given injection delay by considering the reduction in signal fidelity caused by dual-tracer imaging independent of the residual due to noise (Figure 5-2). Using the proposed approach, researchers can optimise their imaging protocol prior to performing experiments to characterise the bias and increased variance caused by dual-tracer imaging. The ability to do this is critical, as in many cases, no ground truth is available to validate the results. Following a demonstration of separating dual-tracer curves using a controlled experiment, this difficulty is surmounted by showing the expected dual-tracer error on simulated dual-tracer data, with extension to a real dual-tracer experiment, with extracted values concurring with single-tracer data.

An experiment was performed using a physical phantom to demonstrate the dual-tracer methodology using real data while still retaining the original single-tracer signals. From this experiment it can be seen that provided care is taken to follow specific protocols, dual-

tracer activity signals can be separated and the original single-tracer activities can be recovered with minimum loss. In addition, following the process outlined in Figure 5-2 showed that values for K_I as calculated from the dual-tracer compartment lie within expected values as calculated from simulations generated from curves measured in the single-tracer compartments. This suggests that the variance in kinetic parameters such as K_I can be predicted using simulations prior to experiments being performed.

Results from the simulations using the mouse data show the dual-tracer error reduces rapidly after the injection delay exceeds one minute, with greater errors occurring for the second tracer. This is most likely due to the residual activity from the first tracer contributing additional noise to the signal subsequent to injection of the second tracer. The separability of two tracers when performing dual-tracer imaging is affected by tissue biology, noise, relative injected activity and injection delay. For the specific cases used in this work, it appears that an injection delay of 10 to 20 minutes is sufficient to recover the kinetic parameters, which concurs with previous studies, with the work by Kadrmas *et al* (6) suggesting an injection delay of 10 minutes sufficient to separate signals for ATSM, PTSM and FDG. In addition, Ikoma *et al* (9) suggested an injection delay of 15 minutes sufficient to separate dual-tracer signals of Flumazenil followed by FDG. Finally, Koeppe *et al* (10) also showed correlating results, with their study suggesting an injection delay of 10-15 minutes is sufficient to recover tracer signals from dual-tracer experiments of three 11C tracers. Therefore, this work adds to the growing body that dual-tracer signals can be recovered without a significant increase in scanning time.

From the results of the actual dual-tracer experiment, shown in Figure 5-10, it can be seen that even with an injection delay of twenty minutes, V_T and K_I parameters recovered for each tracer within the tumour concurs closely with single-tracer imaging and the literature. The tumour uptake is enhanced relative to surrounding tissue in both tracers, apart from regions proximal to the cortical tissue where ^{18}F-FDG uptake is also high (as is typical in the literature). The agreement between the recovered values of V_T and K_I with single-tracer comparisons within the tumour and the brain of the mouse suggests that kinetic parameters can be recovered within the bounds described by experimental simulation.

The separability of two tracers when performing dual-tracer imaging is affected by tissue biology, noise, relative injected activity and injection delay. Tissue biology is not within the control of the experimenter, while ethical considerations limit the amount of activity that can be injected and limitations to scanner sensitivity, so some noise will always exist in the

data. However varying injection delays offers substantial latitude to devise a feasible experiment where information loss is negligible.

Injection delay does require a trade-off as excessively short injection delays can substantially increase dual-tracer error, while long injection delays can unnecessarily lengthen scanning time. However, the results suggest that injection delays of 20-30 minutes suffice in many pre-clinical cases. This will vary for different tracer pairs, but the evidence suggests that provided the injection of the second tracer occurs after the drop off of the initial spike, then the error appears to be manageable. Furthermore, injection delays can be shortened for tissues that rapidly metabolise the tracer or with more sensitive scanners. Tissues with slower dynamics may require a longer injection delay in order to be separated, because the long tails associated with slower dynamics can make tracers less distinguishable.

Relative injected activity also affects the separability of the tracers: if the dose of the first tracer is too high in comparison to the second tracer, then the noise and residual dynamics from the first tracer will conceal the signal from the second tracer. Conversely, a higher injected dose for the second tracer will reduce the influence of the first tracer on this fit. However, increasing the tracer dose also increases the radiation exposure for the patients and thus will need to be considered carefully from an ethical perspective. In addition, inaccurate fits of the first tracer in tissues with slow dynamics may cause inaccuracies in fitting the second tracer. The selection of relative activity can be adapted to tissue of interest if its dynamics are known.

A limitation of this work is that the injected doses were assumed to be the same in all experiments. Also, it is important to note that this work implicitly assumed the count-rate within the field of view is sufficiently controlled to avoid significant loss of sensitivity due to dead-time. Although doses are controlled within protocols to limit radiation exposure, significant dead-time losses cannot always be avoided, for instance when the initially unmixed bolus flows through the arteries in the field of view. Hence future work will explicitly include this effect as an additional reduction in signal to noise ratio as a function of dose and to allow appropriate down-weighting of relevant frames to minimise resultant bias. A further limitation is that the effect of varying the tissue model complexity was not investigated. However, the main contribution of this chapter was to demonstrate the ability for a study designer to pre-validate a dual-tracer protocol. The limiting factor in any experiment will be the ability to recover original single-tracer signals from dual-tracer

images. An increase in the complexity of the pharmacokinetic model *may* have an effect on the recovered signals – however this can be determined on a case-by-case basis by the study designer. This allows the framework to exist in the general case, as adaption of the framework to different pathologies, organs and tracers will have an effect on the parameters required to allow dual-tracer imaging to be performed.

This study has attempted to comprehensively demonstrate that it is possible to effectively predict dual-tracer error and use this to optimise the imaging protocols where dual-tracer imaging is used, by utilising the basis pursuit method proposed in (128). Although real data lacks a ground truth, it is possible to estimate the dual-tracer error from simulations and compare this to experiments. However, this method does assume that the study designer has some information on the expected dynamics of the tissues of interest. This study also assumes that a static noise parameter, c, is sufficient to estimate the bias when performing dual-tracer imaging. However, a spatially varying noise parameter may be more beneficial if scanning areas with varying susceptibility to noise. Even so, a static noise parameter may suffice in the majority of cases. Finally, this study assumes a correctly characterised blood activity concentration. Previous studies have investigated methods for determining the blood activity concentration (96, 132, 133) and this work assumes the study designer is capable of identifying the activity concentration effectively.

Summary

There are a large number of radioactive PET tracers that can be utilised to image a wide range of normal and pathological tissue. In this study the use of the basis pursuit method was utilised to separate two PET tracers that are scanned within the same imaging session. Basis pursuit extends naturally to dual-tracer imaging and avoids having to pre-define kinetic models for multiple combinations of tissue and tracer. Using this approach, the bias and variance can be established from simulations based on expected bounds of biology. Experiments show the predictions of the simulations correspond with results obtained in reality, allowing the injection delay to be selected appropriately to ensure additional error due to dual-tracer imaging is minimised. Based on this approach, the injection delay was selected for a true dual-tracer image. Dual-tracer imaging was performed, with uptake concurring with what would be expected of the cortical and tumour tissues. The V_T was well within the bounds suggested by population data. As demonstrated by the concurrence of the results of the actual dual-tracer experiment and single-tracer data, dual-tracer imaging is practical in the experimental arena and possibly also the clinical arena. This work helps

to support the wider use of dual-tracer imaging and opens the door to a better understanding of those diseases such as brain cancer that are still relatively intractable for reasons that are poorly understood.

Chapter 6 Discussion

PET imaging has the ability to provide information complementary to that obtained from MRI, improving both the diagnostic accuracy and treatment pathways for patients. Previous work has indicated that more than one biological factor may play a role in the development and progression of cancers such as glioma(134). For example, tracers such as ^{18}F-FDOPA and ^{18}F-FMISO identify two independent factors, namely tumour infiltration and tumour hypoxia, respectively. Obtaining information on two or more biological factors currently requires PET imaging to be performed on separate days, or at least far enough apart that residual activity from the first tracer does not contaminate the second. This approach is not practical in most clinical settings due to the significant increase in scanner and clinician time required.

An alternative methodology to performing multiple PET scans is dual-tracer imaging, where two or more tracers are injected within the same imaging session. Since its conception by Huang in 1982, few studies have investigated the idea, and proposed techniques each suffer from particular limitations such as scanning from injection of the first tracer, imposing restrictions on tracer selection and requiring pre-defined kinetic models.

Thesis Summary

The contribution of this PhD was to devise a set of methodological tools to allow study designers to effectively implement an optimal dual-tracer imaging protocol in either the clinical or preclinical setting by allowing the continuous numerical relationship between protocol and additional noise to be understood. It also demonstrated how the dual-tracer problem could be investigated for any combination of tracers and biology without the need for explicitly specified compartment models by utilising the Basis Pursuit technique. The noise in a dual-tracer data set comprises of two components: The irreducible noise due to the scanner itself, and the noise added to the system when performing dual-tracer imaging. In the ideal case, this additional noise is zero. However, in the real-world case, this additional noise can be minimised by controlling the injection protocol.

The first contribution of this PhD was to provide a technique to optimise static dual-tracer imaging protocols, specifically considering the case of glioma imaged with ^{18}F-FDOPA and ^{18}F-FMISO, two tracers that identify biological processes that are thought to be important for glioma treatment. The benefit of using this particular tracer combination is that the

pharmacokinetic properties of ^{18}F-FMISO allows for the assumption that the dynamics of this tracer are stable around two hours post injection, allowing for subtraction of the activity of this tracer using only a small number of frames imaged prior to the injection of ^{18}F-FDOPA. Using this framework, it was shown that two static images, one for each tracer, could be obtained with only a small increase in scanning time of about 5-10 minutes. Here, provided an ^{18}F-FMISO stabilising time of at least 90 minutes is used, the additional noise encountered in the system does not exceed 10%. These findings show that subtracting the activity of one tracer from another can be achieved with little impact on image quality for either tracer.

The second contribution of this PhD was to investigate a more complex version of the developed framework, where residual (but linear) dynamics remain for the first tracer. An example of this is the new tracer ^{64}Cu-Epha2 coupled with ^{18}F-FDOPA. As the uptake and excretion of ^{64}Cu-EphA2 is very slow, it could be assumed that its dynamics were relatively linear and thus, for the second project, it was shown that linear interpolation could be used to estimate and remove this tracer from the ^{18}F-FDOPA activity, provided that the ^{64}Cu-EphA2 imaging time was sufficient to characterise the linear interpolation parameters. For shorter ^{64}Cu-EphA2 imaging times, performing linear interpolation offers no advantages. However, for ^{64}Cu-EphA2 imaging times greater than 10 minutes, performing linear interpolation yields a 1-2% decrease in the resulting error. With this contribution, it was shown that the previous framework could be extended to handle tracers with more complex (linear) dynamics, and that dual-tracer imaging has application outside of cancer diagnostic imaging, specifically the validation of new tracers.

It became clear that dual-tracer imaging could be extended to other paradigms and that the field of dual-tracer imaging was incomplete without a general solution where residual dynamics from the first tracer exist. Therefore, the final contribution of the PhD was to devise a framework that provided a method for dual-tracer imaging to be performed regardless of the tissue imaged or the tracers used. Here, the well documented methodology of basis pursuit was extended into the dual-tracer paradigm and validated it using phantom and real mouse data. The framework can be used to pre-validate any imaging protocol considering any pair of tracers or biological scenarios for various injection times, provided dynamic information of both tracers is available. This work showed that, not only was dual-tracer imaging possible, but that the protocols can be pre-validated to assess validity prior to any experiments being performed. The benefit of basis pursuit is that there is no requirement for a kinetic model to be provided *a priori*, allowing the pre-

validation technique to be extended to the general case of all tracers and all tissue biology types. This is important for cases where the tissue model is not known or not available, for example with new tracers or cases where more than one model exists in the field of view. This method allows the study designer to determine the feasibility of a scanning protocol using simulations prior to implementation, as the amount of error encountered can be estimated given the amount of scanner time available, the scanner being used, the tracers being injected and the tissue to be imaged.

Study Limitations

Like any study, there are limitations that need to be taken into consideration:

Multi-tracer synthesis

In order to perform real dual-tracer experiments, the experimenter needs to ensure that both radiotracers are synthesised and ready to be injected within a short period of time. This may pose a logistical challenge at sites where only one tracer is able to be generated at a time. However, for tracers with longer half-lives and higher yields, this is less of an issue. In this study we have shown in two instances that multi-tracer synthesis is possible, with the experiments performed in ^{64}Cu-Epha2-^{18}F-FDOPA and ^{18}F-FDG -^{18}F-FDOPA mice.

Increased radiation dose

With an additional injected PET tracer, comes an additional source of radiation exposure for the patient which will need to be taken into consideration in any ethics proposals made. This issue can be mitigated, however, as reductions in tracer doses can also be considered. With better attenuation correction and the advent of MR-PET, the CT scan may be obviated.

Not all scenarios can be imaged with dual-tracer PET

While the basis pursuit methodology and pre-validation framework can be applied to any pair of radiotracers, there are some scenarios where the pharmacokinetics of the tracers will not allow effective separation of the two signals. One such scenario is when the

dynamics of the two tracers are very slow but not static or linear. In addition, if the first tracer dynamics are very slow, the injection delay may be too significant to warrant dual-tracer imaging. In this case, it may be beneficial to perform scans on separate days if possible.

Training Data

Pre-validating test radiotracers requires that a certain amount of information about the tracers is known *a priori*. For static scanning, tracer activity needs to be known. For dynamic imaging, pharmacokinetic parameters or a dynamic "training" image needs to be available. This may be difficult for novel radiotracers.

Investigation of Model Complexity

The experiments in this thesis rely on the model complexities of the test tracers used, such that time activity curves generated from pharmacokinetic parameters and curves investigated from real data are a direct reflection of the tracers investigated. Therefore, no experiments were performed investigating the effect of varying the tissue model complexity outside these compartmental models. More complex compartmental models *may* have an effect on the ability to separate tracer signals.

Study sizes

This thesis performs real-world experiments on multiple pre-clinical mouse subjects. However, the number of mouse subjects is small, allowing for inter-subject variability. However, the experiments performed in mouse subjects formed part of other projects, limiting the availability of more test subjects. In addition, the large number of intra-subject test voxels allows for comprehensive intra-subject voxel wise investigations to be performed.

Future Research Paths

Finally, this PhD opens up new research pathways and future topics of research that could expand on these presented techniques. One such pathway is expanding these dual-tracer techniques to the case of more than two injected tracers, and investigating the influence of noise and residual activities on the third injection. An investigation into the limit to the

number of tracers that can be injected in a scanning session would be of great interest in both the clinical and pre-clinical setting.

Furthermore, with the development of PET/MR imaging systems, coupling dual-tracer PET imaging with modalities such as contrast enhanced MRI provides a means to directly compare biological functions with indices derived from BBB breakdown. For example, simultaneous imaging of ^{18}F-FMISO, ^{18}F-FDOPA, Contrast Enhanced MRI and Diffusion weighted imaging would allow simultaneous investigation into a wide range of biological and physiological processes of a tumour.

Conclusions

In summary, a general framework was devised that allows the effective implementation of dual-tracer PET imaging, providing study designers a toolkit for the separation of multiple tracers injected within a single scanning session. The first contribution devised a method for separation of two tracers when the dynamics of the first was stable at the injection of the tracer, with the specific case of treating glioma was considered. However, it became clear that dual-tracer imaging could be applied to other scenarios. Hence the second contribution investigated a pair of tracers where the first tracer activity could be assumed to be linear and was estimated from a few frames imaged prior to the injection of the second tracer. Finally, the dual-tracer framework was extended to the general case of any tissue and tracer combination by using a modified version of the basis pursuit method.

The successful implementation of these methods brings the field of dual-tracer imaging closer towards pre-clinical and clinical translation. It substantially extends the versatility of dual-tracer imaging and gives rise to a new wave of information obtainable from PET imaging allowing researchers to gain greater insight into diseases that remain intractable such as advanced glioma. Finally, by utilising basis pursuit approaches, it is possible to consider any combination of tracers regardless of tracer and without devising specific model of uptake within tissue.

Bibliography

1. Heiss WD, Raab P, Lanfermann H. Multimodality assessment of brain tumors and tumor recurrence. J Nucl Med. 2011;52(10):1585-600.
2. Swanson KR, Alvord Jr EC, Murray JD. Virtual brain tumours (gliomas) enhance the reality of medical imaging and highlight inadequacies of current therapy. Br J Cancer. 2002;86(1):14-8.
3. Bell C, Dowson N, Puttick S, Gal Y, Thomas P, Fay M, et al. Increasing feasibility and utility of (18)F-FDOPA PET for the management of glioma. Nucl Med Biol. 2015;42(10):788-95.
4. Bell C, Dowson N, Fay M, Thomas P, Puttick S, Gal Y, et al. Hypoxia imaging in gliomas with 18F-fluoromisonidazole PET: toward clinical translation. Seminars in nuclear medicine. 2015;45(2):136-50.
5. Huang SC, Carson RE, Hoffman EJ, Kuhl DE, Phelps ME. An investigation of a double-tracer technique for positron computerized tomography. J Nucl Med. 1982;23(9):816-22.
6. Buckner JC. Factors influencing survival in high-grade gliomas. Semin Oncol. 2003;30(6 Suppl 19):10-4.
7. Curran Jr WJ, Scott CB, Horton J, Nelson JS, Weinstein AS, Fischbach AJ, et al. Recursive partitioning analysis of prognostic factors in three Radiation Therapy Oncology Group malignant glioma trials. J Natl Cancer Inst. 1993;85(9):704-10.
8. DeAngelis LM. Brain tumors. N Engl J Med. 2001;344(2):114-23.
9. Behin A, Hoang-Xuan K, Carpentier AF, Delattre JY. Primary brain tumours in adults. Lancet. 2003;361(9354):323-31.
10. Gorlia T, van den Bent MJ, Hegi ME, Mirimanoff RO, Weller M, Cairncross JG, et al. Nomograms for predicting survival of patients with newly diagnosed glioblastoma: prognostic factor analysis of EORTC and NCIC trial 26981-22981/CE.3. Lancet Oncol. 2008;9(1):29-38.
11. Laws ER, Parney IF, Huang W, Anderson F, Morris AM, Asher A, et al. Survival following surgery and prognostic factors for recently diagnosed malignant glioma: data from the Glioma Outcomes Project. J Neurosurg. 2003;99(3):467-73.
12. Louis DN, Ohgaki H, Wiestler OD, Cavenee WK, Burger PC, Jouvet A, et al. The 2007 WHO classification of tumours of the central nervous system. Acta Neuropathol. 2007;114(2):97-109.

13. Goodenberger ML, Jenkins RB. Genetics of adult glioma. Cancer genetics. 2012;205(12):613-21.
14. Mamelak AN, Jacoby DB. Targeted delivery of antitumoral therapy to glioma and other malignancies with synthetic chlorotoxin (TM-601). Expert opinion on drug delivery. 2007;4(2):175-86.
15. Weber G. Enzymology of cancer cells (second of two parts). N Engl J Med. 1977;296(10):541-51.
16. Brizel DM, Dodge RK, Clough RW, Dewhirst MW. Oxygenation of head and neck cancer: changes during radiotherapy and impact on treatment outcome. Radiother Oncol. 1999;53(2):113-7.
17. Gatenby RA, Kessler HB, Rosenblum JS, Coia LR, Moldofsky PJ, Hartz WH, et al. Oxygen distribution in squamous cell carcinoma metastases and its relationship to outcome of radiation therapy. Int J Radiat Oncol Biol Phys. 1988;14(5):831-8.
18. Kolstad P. Intercapillary distance, oxygen tension and local recurrence in cervix cancer. Scand J Clin Lab Invest Suppl. 1968;106:145-57.
19. Folkman J. What is the evidence that tumors are angiogenesis dependent? J Natl Cancer Inst. 1990;82(1):4-6.
20. Brown JM, Wilson WR. Exploiting tumour hypoxia in cancer treatment. Nat Rev Cancer. 2004;4(6):437-47.
21. Hockel M, Vorndran B, Schlenger K, Baussmann E, Knapstein PG. Tumor oxygenation: a new predictive parameter in locally advanced cancer of the uterine cervix. Gynecol Oncol. 1993;51(2):141-9.
22. Thomlinson RH, Gray LH. The histological structure of some human lung cancers and the possible implications for radiotherapy. Br J Cancer. 1955;9(4):539-49.
23. Rampling R, Cruickshank G, Lewis AD, Fitzsimmons SA, Workman P. Direct measurement of pO2 distribution and bioreductive enzymes in human malignant brain tumors. Int J Radiat Oncol Biol Phys. 1994;29(3):427-31.
24. Hall EJ. Radiobiology for the Radiologist. 4 ed. Philadelphia, PA: JB Lippincott Company; 1994.
25. Menegakis A, Eicheler W, Yaromina A, Thames HD, Krause M, Baumann M. Residual DNA double strand breaks in perfused but not in unperfused areas determine different radiosensitivity of tumours. Radiother Oncol. 2011;100(1):137-44.

26. Helleday T, Lo J, van Gent DC, Engelward BP. DNA double-strand break repair: from mechanistic understanding to cancer treatment. DNA Repair (Amst). 2007;6(7):923-35.
27. Rogakou EP, Pilch DR, Orr AH, Ivanova VS, Bonner WM. DNA double-stranded breaks induce histone H2AX phosphorylation on serine 139. J Biol Chem. 1998;273(10):5858-68.
28. Valk PE, Mathis CA, Prados MD, Gilbert JC, Budinger TF. Hypoxia in human gliomas: demonstration by PET with fluorine-18-fluoromisonidazole. J Nucl Med. 1992;33(12):2133-7.
29. Daumas-Duport C, Meder JF, Monsaingeon V, Missir O, Aubin ML, Szikla G. Cerebral gliomas: malignancy, limits and spatial configuration. Comparative data from serial stereotaxic biopsies and computed tomography (a preliminary study based on 50 cases). J Neuroradiol. 1983;10(1):51-80.
30. Scherer HJ. The forms of growth in gliomas and their practical significance. Brain. 1940;63:1-35.
31. Chan JL, Lee SW, Fraass BA, Normolle DP, Greenberg HS, Junck LR, et al. Survival and failure patterns of high-grade gliomas after three-dimensional conformal radiotherapy. J Clin Oncol. 2002;20(6):1635-42.
32. Chen W. Clinical applications of PET in brain tumors. J Nucl Med. 2007;48(9):1468-81.
33. Chen W, Silverman DH, Delaloye S, Czernin J, Kamdar N, Pope W, et al. 18F-FDOPA PET imaging of brain tumors: comparison study with 18F-FDG PET and evaluation of diagnostic accuracy. J Nucl Med. 2006;47(6):904-11.
34. Fueger BJ, Czernin J, Cloughesy T, Silverman DH, Geist CL, Walter MA, et al. Correlation of 6-18F-fluoro-L-dopa PET uptake with proliferation and tumor grade in newly diagnosed and recurrent gliomas. J Nucl Med. 2010;51(10):1532-8.
35. Jora C, Mattakarottu JJ, Aniruddha PG, Mudalsha R, Singh DK, Pathak HC, et al. Comparative evaluation of 18F-FDOPA, 13N-AMMONIA, 18F-FDG PET/CT and MRI in primary brain tumors - A pilot study. Indian J Nucl Med. 2011;26(2):78-81.
36. Ledezma CJ, Chen W, Sai V, Freitas B, Cloughesy T, Czernin J, et al. 18F-FDOPA PET/MRI fusion in patients with primary/recurrent gliomas: initial experience. Eur J Radiol. 2009;71(2):242-8.
37. Pafundi DH, Laack NN, Youland RS, Parney IF, Lowe VJ, Giannini C, et al. Biopsy validation of 18F-DOPA PET and biodistribution in gliomas for

neurosurgical planning and radiotherapy target delineation: results of a prospective pilot study. Neuro Oncol. 2013;15(8):1058-67.
38. Tripathi M, Sharma R, D'Souza M, Jaimini A, Panwar P, Varshney R, et al. Comparative evaluation of F-18 FDOPA, F-18 FDG, and F-18 FLT-PET/CT for metabolic imaging of low grade gliomas. Clin Nucl Med. 2009;34(12):878-83.
39. Walter F, Cloughesy T, Walter MA, Lai A, Nghiemphu P, Wagle N, et al. Impact of 3,4-dihydroxy-6-18F-fluoro-L-phenylalanine PET/CT on managing patients with brain tumors: the referring physician's perspective. J Nucl Med. 2012;53(3):393-8.
40. Wahl L, Nahmias C. Modeling of fluorine-18-6-fluoro-L-Dopa in humans. J Nucl Med. 1996;37(3):432-7.
41. Heiss WD, Wienhard K, Wagner R, Lanfermann H, Thiel A, Herholz K, et al. F-Dopa as an amino acid tracer to detect brain tumors. J Nucl Med. 1996;37(7):1180-2.
42. Dhermain FG, Hau P, Lanfermann H, Jacobs AH, van den Bent MJ. Advanced MRI and PET imaging for assessment of treatment response in patients with gliomas. Lancet Neurol. 2010;9(9):906-20.
43. Wen PY, Macdonald DR, Reardon DA, Cloughesy TF, Sorensen AG, Galanis E, et al. Updated response assessment criteria for high-grade gliomas: response assessment in neuro-oncology working group. J Clin Oncol. 2010;28(11):1963-72.
44. Dunn IF, Heese O, Black PM. Growth factors in glioma angiogenesis: FGFs, PDGF, EGF, and TGFs. J Neurooncol. 2000;50(1-2):121-37.
45. Fischer I, Gagner JP, Law M, Newcomb EW, Zagzag D. Angiogenesis in gliomas: biology and molecular pathophysiology. Brain Pathol. 2005;15(4):297-310.
46. Spence AM, Muzi M, Swanson KR, O'Sullivan F, Rockhill JK, Rajendran JG, et al. Regional hypoxia in glioblastoma multiforme quantified with [18F]fluoromisonidazole positron emission tomography before radiotherapy: correlation with time to progression and survival. Clin Cancer Res. 2008;14(9):2623-30.
47. Swanson KR, Chakraborty G, Wang CH, Rockne R, Harpold HL, Muzi M, et al. Complementary but distinct roles for MRI and 18F-fluoromisonidazole PET in the assessment of human glioblastomas. J Nucl Med. 2009;50(1):36-44.

48. Szeto MD, Chakraborty G, Hadley J, Rockne R, Muzi M, Alvord Jr EC, et al. Quantitative metrics of net proliferation and invasion link biological aggressiveness assessed by MRI with hypoxia assessed by FMISO-PET in newly diagnosed glioblastomas. Cancer Res. 2009;69(10):4502-9.
49. Kawai N, Maeda Y, Kudomi N, Miyake K, Okada M, Yamamoto Y, et al. Correlation of biological aggressiveness assessed by 11C-methionine PET and hypoxic burden assessed by 18F-fluoromisonidazole PET in newly diagnosed glioblastoma. Eur J Nucl Med Mol Imaging. 2011;38(3):441-50.
50. Karunanithi S, Sharma P, Kumar A, Khangembam BC, Bandopadhyaya GP, Kumar R, et al. Comparative diagnostic accuracy of contrast-enhanced MRI and (18)F-FDOPA PET-CT in recurrent glioma. Eur Radiol. 2013;23(9):2628-35.
51. Jeremic B, Milicic B, Grujicic D, Dagovic A, Aleksandrovic J. Multivariate analysis of clinical prognostic factors in patients with glioblastoma multiforme treated with a combined modality approach. J Cancer Res Clin Oncol. 2003;129(8):477-84.
52. Vos MJ, Hoekstra OS, Barkhof F, Berkhof J, Heimans JJ, van Groeningen CJ, et al. Thallium-201 single-photon emission computed tomography as an early predictor of outcome in recurrent glioma. J Clin Oncol. 2003;21(19):3559-65.
53. De Witte O, Levivier M, Violon P, Salmon I, Damhaut P, Wikler Jr D, et al. Prognostic value positron emission tomography with [18F]fluoro-2-deoxy-D-glucose in the low-grade glioma. Neurosurgery. 1996;39(3):470-7.
54. Santra A, Kumar R, Sharma P, Bal C, Julka PK, Malhotra A. F-18 FDG PET-CT for predicting survival in patients with recurrent glioma: a prospective study. Neuroradiology. 2011;53(12):1017-24.
55. Kioi M, Vogel H, Schultz G, Hoffman RM, Harsh GR, Brown JM. Inhibition of vasculogenesis, but not angiogenesis, prevents the recurrence of glioblastoma after irradiation in mice. J Clin Invest. 2010;120(3):694-705.
56. Greenfield JP, Cobb WS, Lyden D. Resisting arrest: a switch from angiogenesis to vasculogenesis in recurrent malignant gliomas. J Clin Invest. 2010;120(3):663-7.
57. Mongiardi MP. Angiogenesis and hypoxia in glioblastoma: a focus on cancer stem cells. CNS Neurol Disord Drug Targets. 2012;11(7):878-83.
58. Fyles A, Milosevic M, Hedley D, Pintilie M, Levin W, Manchul L, et al. Tumor hypoxia has independent predictor impact only in patients with node-negative cervix cancer. J Clin Oncol. 2002;20(3):680-7.

59. Hockel M, Knoop C, Schlenger K, Vorndran B, Baussmann E, Mitze M, et al. Intratumoral pO2 predicts survival in advanced cancer of the uterine cervix. Radiother Oncol. 1993;26(1):45-50.
60. Hockel M, Schlenger K, Aral B, Mitze M, Schaffer U, Vaupel P. Association between tumor hypoxia and malignant progression in advanced cancer of the uterine cervix. Cancer Res. 1996;56(19):4509-15.
61. Knocke TH, Weitmann HD, Feldmann HJ, Selzer E, Potter R. Intratumoral pO2-measurements as predictive assay in the treatment of carcinoma of the uterine cervix. Radiother Oncol. 1999;53(2):99-104.
62. Sundfor K, Lyng H, Trope CG, Rofstad EK. Treatment outcome in advanced squamous cell carcinoma of the uterine cervix: relationships to pretreatment tumor oxygenation and vascularization. Radiother Oncol. 2000;54(2):101-7.
63. Cher LM, Murone C, Lawrentschuk N, Ramdave S, Papenfuss A, Hannah A, et al. Correlation of hypoxic cell fraction and angiogenesis with glucose metabolic rate in gliomas using 18F-fluoromisonidazole, 18F-FDG PET, and immunohistochemical studies. J Nucl Med. 2006;47(3):410-8.
64. Kawai N, Lin W, Cao WD, Ogawa D, Miyake K, Haba R, et al. Correlation between F-fluoromisonidazole PET and expression of HIF-1alpha and VEGF in newly diagnosed and recurrent malignant gliomas. Eur J Nucl Med Mol Imaging. 2014.
65. Brizel DM, Sibley GS, Prosnitz LR, Scher RL, Dewhirst MW. Tumor hypoxia adversely affects the prognosis of carcinoma of the head and neck. Int J Radiat Oncol Biol Phys. 1997;38(2):285-9.
66. Haensgen G, Krause U, Becker A, Stadler P, Lautenschlaeger C, Wohlrab W, et al. Tumor hypoxia, p53, and prognosis in cervical cancers. Int J Radiat Oncol Biol Phys. 2001;50(4):865-72.
67. Nordsmark M, Overgaard J. A confirmatory prognostic study on oxygenation status and loco-regional control in advanced head and neck squamous cell carcinoma treated by radiation therapy. Radiother Oncol. 2000;57(1):39-43.
68. Rofstad EK, Sundfor K, Lyng H, Trope CG. Hypoxia-induced treatment failure in advanced squamous cell carcinoma of the uterine cervix is primarily due to hypoxia-induced radiation resistance rather than hypoxia-induced metastasis. Br J Cancer. 2000;83(3):354-9.
69. Rudat V, Vanselow B, Wollensack P, Bettscheider C, Osman-Ahmet S, Eble MJ, et al. Repeatability and prognostic impact of the pretreatment

pO(2) histography in patients with advanced head and neck cancer. Radiother Oncol. 2000;57(1):31-7.
70. Wendt TG, Bank P. Prognostic factors in squamous cell carcinoma of the head and neck. Onkologie. 2002;25(3):208-12.
71. Karunanithi S, Sharma P, Kumar A, Gupta DK, Khangembam BC, Ballal S, et al. Can F-FDOPA PET/CT predict survival in patients with suspected recurrent glioma? A prospective study. Eur J Radiol. 2013.
72. Evans SM, Judy KD, Dunphy I, Jenkins WT, Hwang WT, Nelson PT, et al. Hypoxia is important in the biology and aggression of human glial brain tumors. Clin Cancer Res. 2004;10(24):8177-84.
73. Flynn JR, Wang L, Gillespie DL, Stoddard GJ, Reid JK, Owens J, et al. Hypoxia-regulated protein expression, patient characteristics, and preoperative imaging as predictors of survival in adults with glioblastoma multiforme. Cancer. 2008;113(5):1032-42.
74. Lally BE, Rockwell S, Fischer DB, Collingridge DR, Piepmeier JM, Knisely JP. The interactions of polarographic measurements of oxygen tension and histological grade in human glioma. Cancer J. 2006;12(6):461-6.
75. Oliver L, Olivier C, Marhuenda FB, Campone M, Vallette FM. Hypoxia and the malignant glioma microenvironment: regulation and implications for therapy. Curr Mol Pharmacol. 2009;2(3):263-84.
76. Ceyssens S, Van Laere K, de Groot T, Goffin J, Bormans G, Mortelmans L. [11C]methionine PET, histopathology, and survival in primary brain tumors and recurrence. AJNR Am J Neuroradiol. 2006;27(7):1432-7.
77. Spetzler RF, Martin NA. A proposed grading system for arteriovenous malformations. J Neurosurg. 1986;65(4):476-83.
78. Hirata K, Terasaka S, Shiga T, Hattori N, Magota K, Kobayashi H, et al. (1)(8)F-Fluoromisonidazole positron emission tomography may differentiate glioblastoma multiforme from less malignant gliomas. Eur J Nucl Med Mol Imaging. 2012;39(5):760-70.
79. Yamamoto Y, Maeda Y, Kawai N, Kudomi N, Aga F, Ono Y, et al. Hypoxia assessed by 18F-fluoromisonidazole positron emission tomography in newly diagnosed gliomas. Nucl Med Commun. 2012;33(6):621-5.
80. Bruehlmeier M, Roelcke U, Schubiger PA, Ametamey SM. Assessment of hypoxia and perfusion in human brain tumors using PET with 18F-fluoromisonidazole and 15O-H2O. J Nucl Med. 2004;45(11):1851-9.

81. Nioche C, Soret M, Gontier E, Lahutte M, Dutertre G, Dulou R, et al. Evaluation of quantitative criteria for glioma grading with static and dynamic 18F-FDopa PET/CT. Clin Nucl Med. 2013;38(2):81-7.
82. Kratochwil C, Combs SE, Leotta K, Afshar-Oromieh A, Rieken S, Debus Jr, et al. Intra-individual comparison of 18F-FET and 18F-DOPA in PET imaging of recurrent brain tumors. Neuro-oncology. 2013(October):1-7.
83. Kim B, Soisson E, Duma C, Chen P, Hafer R, Cox C, et al. Treatment of recurrent high grade gliomas with hypofractionated stereotactic image-guided helical tomotherapy. Clin Neurol Neurosurg. 2011;113(6):509-12.
84. Kadrmas DJ, Rust TC. Feasibility of rapid multitracer PET tumor imaging. Nuclear Science, IEEE Transactions on. 2005;52(5):1341-7.
85. Figueiras FP, Jimnez X, Pareto D, G√≥mez V, Llop J, Herance R, et al. Simultaneous dual-tracer PET imaging of the rat brain and its application in the study of cerebral ischemia. Molecular imaging and biology : MIB : the official publication of the Academy of Molecular Imaging. 2011;13(3):500-10.
86. Verhaeghe J, Reader AJ. Simultaneous water activation and glucose metabolic rate imaging with PET. Physics in medicine and biology. 2013;58(3):393-411.
87. Ikoma Y, Toyama H, Uemura K, Uchiyama A, editors. Evaluation of the reliability in kinetic analysis for dual tracer injection of FDG and flumazenil PET study2001 2001.
88. Koeppe RA, Raffel DM, Snyder SE, Ficaro EP, Kilbourn MR, Kuhl DE. Dual-[11C]tracer single-acquisition positron emission tomography studies. J Cereb Blood Flow Metab. 2001;21(12):1480-92.
89. Kadrmas DJ, Rust TC, Hoffman JM. Single-scan dual-tracer FLT+FDG PET tumor characterization. Phys Med Biol. 2013;58(3):429-49.
90. Zhang JL, Michael Morey A, Kadrmas DJ. Application of separable parameter space techniques to multi-tracer PET compartment modeling. Phys Med Biol. 2016;61(3):1238-58.
91. Gao F, Liu H, Jian Y, Shi P. Dynamic dual-tracer PET reconstruction. Inf Process Med Imaging. 2009;21:38-49.
92. Cheng X, Navab N, Ziegler S, Shi K. Direct Parametric Image Reconstruction of Rapid Multi-tracer PET. In: Mori K, Sakuma I, Sato Y, Barillot C, Navab N, editors. 8151: Springer Berlin Heidelberg; 2013. p. 155-62.

93. Lage E, Parot V, Moore SC, Sitek A, Udias JM, Dave SR, et al. Recovery and normalization of triple coincidences in PET. Medical physics. 2015;42(3):1398-410.
94. Wang W, Lee NY, Georgi J-C, Narayanan M, Guillem J, SchѴðder H, et al. Pharmacokinetic analysis of hypoxia (18)F-fluoromisonidazole dynamic PET in head and neck cancer. Journal of nuclear medicine : official publication, Society of Nuclear Medicine. 2010;51(1):37-45.
95. Huang SC, M.E P. Principle of Tracer Kinetic Modeling in Positron Emission Tomography and Autoradiography. New York: Raven Press; 1986. p. 287-345.
96. Schiepers C, Chen W, Cloughesy T, Dahlbom M, Huang SC. 18F-FDOPA kinetics in brain tumors. J Nucl Med. 2007;48(10):1651-61.
97. Huang SC, Barrio JR, Yu DC, Chen B, Grafton S, Melega WP, et al. Modelling approach for separating blood time-activity curves in positron emission tomographic studies. Phys Med Biol. 1991;36(6):749-61.
98. Chondrogiannis S, Cristina Marzola M, Al-Nahhas A, Venkatanarayana TD, Mazza A, Opocher G, et al. Normal biodistribution pattern and physiologic variants of (18)F-DOPA PET imaging. Nuclear Medicine Communications. 2013;34(12):1141-9.
99. Carlin S, Zhang H, Reese M, Ramos NN, Chen Q, Ricketts S-A. A Comparison of the Imaging Characteristics and Microregional Distribution of 4 Hypoxia PET Tracers. Journal of nuclear medicine : official publication, Society of Nuclear Medicine. 2014;55(3):515-21.
100. Wang W, Georgi JC, Nehmeh SA, Narayanan M, Paulus T, Bal M, et al. Evaluation of a compartmental model for estimating tumor hypoxia via FMISO dynamic PET imaging. Phys Med Biol. 2009;54(10):3083-99.
101. Eschmann S-M, Paulsen F, Reimold M, Dittmann H, Welz S, Reischl G, et al. Prognostic impact of hypoxia imaging with 18F-misonidazole PET in non-small cell lung cancer and head and neck cancer before radiotherapy. Journal of nuclear medicine : official publication, Society of Nuclear Medicine. 2005;46(2):253-60.
102. Barrett HH, Wilson DW, Tsui BM. Noise properties of the EM algorithm: I. Theory. Physics in medicine and biology. 1994;39(5):833-46.
103. Wilson DW, Tsui BM, Barrett HH. Noise properties of the EM algorithm: II. Monte Carlo simulations. Physics in medicine and biology. 1994;39(5):847-71.

104. Chen K, Huang S-C, Yu D-C. The effects of measurement errors in the plasma radioactivity curve on parameter estimation in positron emission tomography. Physics in Medicine and Biology. 1991;36(9):1183-200.
105. Logan J, Fowler JS, Volkow ND, Ding YS, Wang GJ, Alexoff DL. A strategy for removing the bias in the graphical analysis method. Journal of cerebral blood flow and metabolism : official journal of the International Society of Cerebral Blood Flow and Metabolism. 2001;21(3):307-20.
106. Varga Jz, Szabo Z. Modified regression model for the Logan plot. Journal of cerebral blood flow and metabolism : official journal of the International Society of Cerebral Blood Flow and Metabolism. 2002;22(2):240-4.
107. Rajendran JG, Mankoff DA, O'Sullivan F, Peterson LM, Schwartz DL, Conrad EU, et al. Hypoxia and glucose metabolism in malignant tumors: evaluation by [18F]fluoromisonidazole and [18F]fluorodeoxyglucose positron emission tomography imaging. Clin Cancer Res. 2004;10(7):2245-52.
108. Thorwarth D, Eschmann SM, Paulsen F, Alber M. A kinetic model for dynamic [18F]-Fmiso PET data to analyse tumour hypoxia. Phys Med Biol. 2005;50(10):2209-24.
109. Corroyer-Dulmont A, Peres EA, Petit E, Durand L, Marteau L, Toutain J, et al. Noninvasive assessment of hypoxia with 3-[18F]-fluoro-1-(2-nitro-1-imidazolyl)-2-propanol ([18F]-FMISO): a PET study in two experimental models of human glioma. Biol Chem. 2013;394(4):529-39.
110. Dence CS, Ponde DE, Welch MJ, Lewis JS. Autoradiographic and small-animal PET comparisons between (18)F-FMISO, (18)F-FDG, (18)F-FLT and the hypoxic selective (64)Cu-ATSM in a rodent model of cancer. Nucl Med Biol. 2008;35(6):713-20.
111. Tochon-Danguy HJ, Sachinidis JI, Chan F, Chan JG, Hall C, Cher L, et al. Imaging and quantitation of the hypoxic cell fraction of viable tumor in an animal model of intracerebral high grade glioma using [18F]fluoromisonidazole (FMISO). Nucl Med Biol. 2002;29(2):191-7.
112. Valable S, Petit E, Roussel S, Marteau L, Toutain J, Divoux D, et al. Complementary information from magnetic resonance imaging and (18)F-fluoromisonidazole positron emission tomography in the assessment of the response to an antiangiogenic treatment in a rat brain tumor model. Nucl Med Biol. 2011;38(6):781-93.

113. Agostinelli S, Allison J, Amako K, Apostolakis J, Araujo H, Arce P, et al. Geant4, a simulation toolkit. Nuclear Instruments and Methods in Physics Research Section A: Accelerators, Spectrometers, Detectors and Associated Equipment. 2003;506(3):250-303.
114. Allison J, Amako K, Apostolakis J, Araujo H, Dubois PA, Asai M, et al. Geant4 developments and applications. Nuclear Science, IEEE Transactions on. 2006;53(1):270-8.
115. Siemens-AG. Technical Document "microPET List Mode format". 2006.
116. Puttick S, Stringer BW, Day BW, Bruce ZC, Ensbey KS, Mardon K, et al. EphA2 as a Diagnostic Imaging Target in Glioblastoma: A Positron Emission Tomography/Magnetic Resonance Imaging Study. Molecular imaging. 2015;14:385-99.
117. Hatano M, Eguchi J, Tatsumi T, Kuwashima N, Dusak JE, Kinch MS, et al. EphA2 as a glioma-associated antigen: a novel target for glioma vaccines. Neoplasia. 2005;7(8):717-22.
118. Wen PY, Kesari S. Malignant gliomas. Curr Neurol Neurosci Rep. 2004;4(3):218-27.
119. Wykosky J, Gibo DM, Stanton C, Debinski W. EphA2 as a novel molecular marker and target in glioblastoma multiforme. Mol Cancer Res. 2005;3(10):541-51.
120. Liu F, Park PJ, Lai W, Maher E, Chakravarti A, Durso L, et al. A genome-wide screen reveals functional gene clusters in the cancer genome and identifies EphA2 as a mitogen in glioblastoma. Cancer Res. 2006;66(22):10815-23.
121. Wang LF, Fokas E, Bieker M, Rose F, Rexin P, Zhu Y, et al. Increased expression of EphA2 correlates with adverse outcome in primary and recurrent glioblastoma multiforme patients. Oncol Rep. 2008;19(1):151-6.
122. Goldenberg DM. Targeted therapy of cancer with radiolabeled antibodies. J Nucl Med. 2002;43(5):693-713.
123. Goldenberg DM. Advancing role of radiolabeled antibodies in the therapy of cancer. Cancer Immunol Immunother. 2003;52(5):281-96.
124. Goldenberg DM, Sharkey RM. Advances in cancer therapy with radiolabeled monoclonal antibodies. Q J Nucl Med Mol Imaging. 2006;50(4):248-64.
125. Sliwkowski MX, Mellman I. Antibody therapeutics in cancer. Science. 2013;341(6151):1192-8.

126. Mould DR, Sweeney KR. The pharmacokinetics and pharmacodynamics of monoclonal antibodies--mechanistic modeling applied to drug development. Curr Opin Drug Discov Devel. 2007;10(1):84-96.
127. Rivest-Hénault D, Dowson N, Greer P, J. F, J. D. Robust inverse-consistent affine registration for the construction of CT-MR atlases of pelvis for the guidance of prostate radiation therapy. Medical Image Analysis. 2014;Under Review.
128. Gunn RN, Gunn SR, Turkheimer FE, Aston JA, Cunningham VJ. Positron emission tomography compartmental models: a basis pursuit strategy for kinetic modeling. J Cereb Blood Flow Metab. 2002;22(12):1425-39.
129. Gunn RN, Gunn SR, Cunningham VJ. Positron emission tomography compartmental models. J Cereb Blood Flow Metab. 2001;21(6):635-52.
130. Alf MF, Wyss MT, Buck A, Weber B, Schibli R, Kramer SD. Quantification of brain glucose metabolism by 18F-FDG PET with real-time arterial and image-derived input function in mice. J Nucl Med. 2013;54(1):132-8.
131. Bolcaen J, Lybaert K, Moerman L, Descamps B, Deblaere K, Boterberg T, et al. Kinetic Modeling and Graphical Analysis of 18F-Fluoromethylcholine (FCho), 18F-Fluoroethyltyrosine (FET) and 18F-Fluorodeoxyglucose (FDG) PET for the Fiscrimination between High-Grade Glioma and Radiation Necrosis in Rats. PLoS ONE. 2016;11(8).
132. Tantawy MN, Peterson TE. Simplified [(18)F]FDG Image-Derived Input Function Using the Left Ventricle, Liver, and One Venous Blood Sample. Molecular imaging. 2010;9(2):76-86.
133. Zhou S, Chen K, Reiman EM, Li D-m, Shan B. A method of generating image derived input function in quantitative (18)F-FDG PET study based on the monotonicity of the input and output function curve. Nuclear medicine communications. 2012;33(4):10.1097/MNM.0b013e32834f262e.
134. Hanahan D, Weinberg RA. The hallmarks of cancer. Cell. 2000;100(1):57-70.